



**Michigan  
Technological  
University**

Michigan Technological University  
**Digital Commons @ Michigan Tech**

---

Dissertations, Master's Theses and Master's Reports

---

2022

## MEASURING THE PHYSICOCHEMICAL PROPERTIES OF VIRAL VECTORS TO ENHANCE GENE THERAPY PRODUCTION

Oluwatoyin Areo

*Michigan Technological University, oareo@mtu.edu*

Copyright 2022 Oluwatoyin Areo

---

### Recommended Citation

Areo, Oluwatoyin, "MEASURING THE PHYSICOCHEMICAL PROPERTIES OF VIRAL VECTORS TO ENHANCE GENE THERAPY PRODUCTION", Open Access Dissertation, Michigan Technological University, 2022.  
<https://doi.org/10.37099/mtu.dc.etr/1493>

Follow this and additional works at: <https://digitalcommons.mtu.edu/etr>

 Part of the [Chemical Engineering Commons](#)

MEASURING THE PHYSICOCHEMICAL PROPERTIES OF VIRAL VECTORS TO  
ENHANCE GENE THERAPY PRODUCTION

By

Oluwatoyin Areo

A DISSERTATION

Submitted in partial fulfillment of the requirements for the degree of

DOCTOR OF PHILOSOPHY

In Chemical Engineering

MICHIGAN TECHNOLOGICAL UNIVERSITY

2022

© 2022 Oluwatoyin Areo

This dissertation has been approved in partial fulfillment of the requirements for the Degree of DOCTOR OF PHILOSOPHY in Chemical Engineering.

Department of Chemical Engineering

Dissertation Advisor: *Dr. Caryn L. Heldt*

Committee Member: *Dr. Tony N. Rogers*

Committee Member: *Dr. Lei Pan*

Committee Member: *Dr. Jeremy Goldman*

Department Chair: *Dr. Pradeep Agrawal*

# Table of Contents

List of figures .....	vi
List of tables.....	ix
Author contribution statement .....	x
Acknowledgements.....	xii
Abstract.....	xiii
1 Introduction and chapter summaries .....	1
1.1 Introduction .....	1
1.2 Chapter summaries .....	3
1.3 Summary .....	4
2 Literature review .....	5
2.1 Overview of gene therapy .....	5
2.2 Viral vectors for gene delivery .....	7
2.2.1 Selection criteria for viral vectors.....	8
2.2.2 AAV biology and as a vector for <i>in vivo</i> gene delivery.....	10
2.2.3 Manufacture of rAAV vectors .....	12
2.2.3.1 Purification of viral vectors using chromatography.....	16
2.2.3.2 Common additives used to enhance virus purification ...	21
2.3 Virus surface chemistry.....	23
2.3.1 Hydrophobicity .....	24
2.3.2 Charge .....	26
2.3.3 Typical methods for virus surface chemistry characterization .....	27
2.3.3.1 Hydrophobic interaction chromatography (HIC).....	28
2.3.3.2 Partitioning – aqueous two – phase systems (ATPS) ....	29
2.3.3.3 Isoelectric focusing .....	31
2.3.3.4 Chromatofocusing.....	32
2.3.3.5 Dye adsorption .....	34
2.3.3.5.1 Langmuir adsorption isotherm derivation	37
2.3.3.5.2 Freundlich adsorption isotherm derivation	39
2.3.4 Novel approach – single particle - chemical force microscopy (CFM) 40	
2.3.4.1 Working principles of AFM.....	41
2.3.4.2 AFM tip properties.....	42

	2.3.4.3	AFM measurement modes .....	43
	2.3.4.4	Force – Distance measurement .....	45
3		Virus surface hydrophobicity characterization using chemical force microscopy ...	49
	3.1	Introduction .....	49
	3.2	Materials and methods.....	52
	3.2.1	Materials .....	52
	3.2.2	Propagation and titration of cells and virus .....	53
	3.2.3	Virus and control surface preparation.....	53
	3.2.4	Buffers.....	54
	3.2.5	AFM probe functionalization.....	54
	3.2.6	AFM imaging, force measurement, and analysis.....	54
	3.2.7	Dye adsorption .....	55
	3.3	Results .....	56
	3.3.1	Virus hydrophobicity by CFM.....	57
	3.3.2	Virus hydrophobicity by dye adsorption isotherms .....	60
	3.4	Discussion .....	62
	3.5	Conclusions and future work.....	65
4		Understanding the Separation of Empty and Full AAV Capsids on Ion Exchange Chromatography by Chemical Force Microscopy .....	67
	4.1	Introduction .....	67
	4.2	Materials and Methods .....	70
	4.2.1	Materials .....	70
	4.2.2	Methods.....	70
	4.2.2.1	AAV production.....	70
	4.2.2.2	Virus samples and control surface preparation .....	70
	4.2.2.3	Preparation of buffers .....	71
	4.2.2.4	AFM probe functionalization.....	71
	4.2.2.5	Force measurements and analysis .....	72
	4.3	Results and Discussion .....	72
	4.3.1	Differential binding analysis based on buffer pH and conductivity of empty – full AAV capsids. ....	75
	4.3.2	Effect of Buffer Composition .....	79
	4.4	Conclusions and future work.....	83
5		Single-Particle Characterization of SARS-CoV-2 Isoelectric Point and Comparison to Variants of Interest.....	84
	5.1	Introduction .....	84
	5.2	Materials and Methods .....	86

5.2.1	Materials .....	86
5.2.2	Methods.....	87
5.2.2.1	Virus samples, AFM probe functionalization and control surface preparation.....	87
5.2.2.2	Preparation of buffers .....	87
5.2.2.3	Force measurements and analysis.....	88
5.3	Results and Discussion.....	88
5.4	Conclusion.....	91
6	Conclusions and future work .....	93
6.1	Conclusions .....	93
6.2	Future work .....	95
7	References.....	98
A	Appendix.....	119
A.1	Virus surface hydrophobicity characterization using chemical force microscopy.....	119
A.2	Effect of Charge and Hydrophobicity on the Separation of Empty and Full AAV Capsids on Ion Exchange Chromatography.....	127
A.3	Single-Particle Characterization of SARS-CoV-2 Isoelectric Point and Comparison to Variants of Interest .....	134
B	Copyright documentation.....	138
B.1	Reuse license for Figure 2.2 .....	138
B.2	Reuse license for Figure 2.4 and Figure 2.5.....	141
B.3	Reuse license for Figure 2.6.....	145
B.4	Reuse license for Figure 2.10.....	148

## List of figures

- Figure 2.1: Virus structures** (a) A non-enveloped virus (b) An enveloped virus (*created in biorender*) .....8
- Figure 2.2: AAV genome and mRNA transcripts.** The promoters that transcribe the *rep* gene are p5 and p19. *Rep* 78, 68, 52, and 40 are all proteins generated by the *rep* gene. The binding of *Rep* 78/68 to the RBE initiates AAV DNA replication at any of the ITRs. p40 generates VP1, VP2, VP3, and AAP mRNAs. AAP promotes native *Cap* protein trafficking into the nucleolus, where capsid formation occurs. Reprinted from [62] with permission.....11
- Figure 2.3:** Flow chart showing the activities involved in the upstream and downstream processing of viral vectors [69].....13
- Figure 2.4: Production of AAV by triple transfection using HEK293 cells.** The first plasmid contains the vector genome, which is the transgene expression cassette, flanked by the ITR. The AAV helper which is the second plasmid contains the *rep* and *cap* of the serotype to be produced. The third plasmid which is the A helper consists of the genes which supports AAV replication. For the double transfection, the second and third plasmid are cloned into a single plasmid. Reprinted from [70] with permission.....14
- Figure 2.5: Production of AAV in producer and packaging cell lines.** Producer cell line comprises of transgene expression cassette, and the *rep* and *cap* genes which is then infected with a helper virus to induce AAV replication. The packaging cell only consists of the *rep* and *cap* genes while the transgene expression cassette and helper function is provided by virus transduction using Adv. Reprinted from [70] with permission. ....15
- Figure 2.6: Hydrophobic interaction chromatography.** (A) The surface of viruses covered with water hydration layer, making the viruses unable to interact with the hydrophobic ligand. The hydration layer is formed by the rearrangement of water molecules. (B) Effect of salt on the hydrophobic surfaces – the addition of salts results to a dehydration of the virus surface causing an exposure of the virus hydrophobic surface. This allows an interaction with the hydrophobic ligand. Reprinted from [100] with permission.....18
- Figure 2.7:** Schematic Hofmeister series showing the effect of anions and cations on protein precipitation .....19
- Figure 2.8:** A mixed mode chromatography ligand with different interaction sites [114]. .....21
- Figure 2.9: Illustration of AFM function.** The AFM tip has a cantilever which comes in contact with the sample. The laser beam incident on the cantilever. The photodiode records cantilever deflections as the tip scans the sample surface. The cantilever deflection which is reflected on the photodiode through the mirror. The

cantilever deflection and tip-sample distance is processed by the computer and controllers [210].	42
<b>Figure 2.10: Force-distance curve schematic.</b> The AFM tip comes in contact with the sample surface and exerts a predetermined loading force, resulting to cantilever deflection. The tip is held on the sample surface by an adhesive force but it eventually breaks free as the tip is retracted. Those adhesion forces can be calculated from the pull-off force region. Reprinted from [233] with permission.	46
<b>Figure 3.1 CH<sub>3</sub> functionalized AFM probe in contact with viruses.</b> A gold coated glass slide is functionalized with a self-assembled monolayer of thiol compounds that are 50/50 COOH and CH <sub>3</sub> . The viruses are covalently bound to the COOH groups with NHS/EDC chemistry. The functionalized AFM probe measures the forces between the functionalized tip and viruses on the surface in different liquid environments. (Created with Biorender.com).	57
<b>Figure 3.2 Salt concentration effect on PPV and BVDV adhesion.</b>	59
<b>Figure 3.3 Cosolvents change hydrophobic interactions.</b> The addition of PEG 8000 and ethanol to PBS altered the CFM adhesion force. (A) PPV and (B) BVDV with the addition of polyethylene glycol (PEG) 8000 and ethanol. Each data point is the mean of at least 150 measurements with three different combinations of probes and virus surfaces.	60
<b>Figure 3.4 Adsorption isotherms for PPV and BVDV.</b> Fixed concentrations of PPV and BVDV were combined with various concentrations of Rose Bengal in different concentrations of salt. The isotherms were fitted using the Langmuir, and Freundlich models (A) PPV in 1X PBS (B) PPV in 1X PBS + 195mM NaCl (C) PPV in 1X PBS + 845mM NaCl (D) BVDV in 1X PBS (E) BVDV in 1X PBS + 195mM NaCl (F) BVDV in 1X PBS + 845mM NaCl. Each data point is in triplicate, and the error bars represent the standard deviation.	61
<b>Figure 4.1: Chromatogram for AAV initial pool loaded at high conductivity.</b> The empty capsids were collected in the wash step while the full capsids were collected in the peak for full capsids. Red and blue traces correspond to A <sub>260</sub> and A <sub>280</sub> respectively. Black trace corresponds to conductivity.	73
<b>Figure 4.2: Chromatograms showing peaks of AAV loaded on an AEX column using low conductivity buffer at pH 8.8</b> (A) Empty capsids (B) Full capsids. Red and blue traces correspond to A <sub>260</sub> and A <sub>280</sub> respectively. Black trace corresponds to conductivity.	73
<b>Figure 4.3: Measurement for viruses using CFM.</b> AFM probe functionalized with either a positive charge or hydrophobic chemistry in contact with virus particles covalently bound using the COOH-CH <sub>3</sub> self-assembly monolayer on a gold-coated glass slide in a liquid environment. Image was created with Biorender.com. Adopted from [204].	74

<b>Figure 4.4: AAV Force measurement as a function of buffer conductivity and pH</b> (A) Empty capsids (B) Full capsids. The points on this map indicate the solution conditions tested to show the effect of buffer pH and conductivity on the adhesion force. ....	76
<b>Figure 4.5: Adhesion forces for AAV at pH 8.8</b> (A) Adhesion force measurements with a positive $\text{NR}_3^+$ functionalized probe and (B) with hydrophobic $\text{CH}_3$ functionalized probe.....	79
<b>Figure 4.6: The effect of salt concentration and surfactant at pH 8.8 on empty and full AAV3B.</b> (A) The adhesion force changes in empty and full capsids when sodium acetate was added to 100 mM Tris buffer. (B) The adhesion force changes in empty and full capsids when 0.01 w/w% P188 was added to sodium acetate + Tris buffer. (C) The adhesion force changes in empty and full capsids when 5mM magnesium chloride was added to sodium acetate + Tris buffer. (D) Effect of 5 mM magnesium chloride, 0.01% P188, and sodium acetate on empty capsids. (E) Effect of 5 mM magnesium chloride, 0.01% P188, and sodium acetate on full capsids.....	82
<b>Figure 5.1: Isoelectric point determination using CFM.</b> (A) Inactivated SARS-CoV-2 particles were covalently immobilized on a Au-coated slide that contained a self-assembled monolayer that presented COOH and $\text{CH}_3$ functional groups. NHS/EDC chemistry covalently bound the virus to the COOH groups [158, 200]. Au tips were functionalized to provide either negatively charged carboxyl ( $\text{COO}^-$ ) or positively charged quaternary amine ( $\text{NR}_4^+$ ) groups. Changes in the mean adhesion forces were measured with respect to pH with (B) a $\text{NR}_4^+$ probe or (C) a $\text{COO}^-$ probe. The data points of the mean adhesion force vs. pH were fit to a sigmoidal curve and the IEP was determined to be the infection point. The histogram of each individual point can be found in <b>Figure A.3.2</b> . * $p < 0.05$ from student's t-test. (Image A was created in BioRender.com). ....	89
<b>Figure 5.2: Comparison of the mutations (Row 1 and 2) and surface electrostatic potentials (Row 3) on spike proteins of two VOIs with respect to the WT.</b> WT(PDB ID: 6VYB [341] (1 <sup>st</sup> column) and 6VSB [342] (2 <sup>nd</sup> column), B.1.1.7 (PDB ID: 7LWV [340]) and B.1.351 (PDB ID: 7LYQ [340]). (A-D) show the side view, 1 <sup>st</sup> row, and (E-H) show the top view, 2 <sup>nd</sup> row. For the VOIs, the AA mutations on the S proteins (see <b>Table 5.2</b> for details) are marked red with one residue before and after the actual mutational site for better visibility. (I-L) S-protein surface potentials of the WT and VOIs. The surface potentials were generated by preparing molecules with the pdb2pqr method and applying APBS electrostatics using PyMol v2.4.1. ....	90

## List of tables

<b>Table 2.1</b> Gene therapy characteristics of viral vectors [45, 53].....	9
<b>Table 2.2</b> Information on additives classes, types, concentration, and purpose [115]. ....	22
<b>Table 3.1</b> Summary of isotherm parameters for adsorption of Rose Bengal to PPV and BVDV .....	62
<b>Table 4.1.</b> Summary of physical titer, absorbance, and conductivity for each peak from chromatograms.....	74
<b>Table 5.1.</b> Summary of current IEP values for SARS-CoV-2 S protein.....	86
<b>Table 5.2.</b> Comparison of surface charge on S protein of the two VOI with the wild type. ....	91

## Author contribution statement

From September 2018 to September 2022, the work in this dissertation was accomplished at Michigan Technological University's Department of Chemical Engineering. Oluwatoyin Areo authored this dissertation. Oluwatoyin Areo carried out all of the experiments and measurements discussed in this dissertation with the assistance of collaborators and laboratory colleagues listed in the following paragraphs.

Chapter 3 examines virus hydrophobicity characterization on a single – particle level using chemical force microscopy (CFM). The CFM sample preparations, data collection and analysis, figures design, and writing of the paper were performed by me. For the dye adsorption, buffer and virus sample preparation, absorbance readings, data analysis and figure design was performed by me. To determine the effect of buffers salt concentration, and additives on the virus infectivity, a collaborative work was done by Elliana Sempek and myself. I prepared the buffer solution with the additives, and virus stock. Elliana performed the MTT assay to determine the virus infectivity. The paper in this chapter was written under the supervision of Dr. Heldt. Dr. Fei Long assisted with software troubleshooting and solving technical problems of the AFM instrument during data collection. This chapter is currently being prepared for submission to a peer-reviewed journal.

Chapter 4 explores the separation of empty and full AAV3B capsids using differences in surface charge distribution as determined by the CFM when buffer conditions change. It was a collaborative research project with Dr. Alex Berill and Dr. Yulia Ivanova from Pfizer. Dr. Heldt created the research concept and methodology. Dr. Berill also contributed to design the research methodology, secured funding, sent buffer materials, and virus stock for this project. I prepared the CFM samples, collected and analyzed the data, designed the figures, and wrote the paper under the supervision of Dr. Heldt. Dr. Ivanova assisted with providing some buffer conditions, and performing chromatography experiments as shown in **Figure 4.1** and **Figure 4.2** This chapter has been submitted to Pfizer for legal approval in order for it to be published. This chapter will be submitted to a peer-reviewed journal after receiving approval from Pfizer.

Chapter 5 is about the determination of SARS-CoV-2 isoelectric point on a single particle level using CFM. The CFM sample preparations, data collection and analysis, and design of **Figure 5.1b&c** was performed by me. Dr. Pratik Joshi performed the computational analysis for the variants of interests and designed **Figure 5.1a & Figure 5.2**. I wrote the introduction, while Dr. Pratik Joshi wrote the results, discussion and conclusion. The writing was done under the supervision of Dr. Heldt. The conceptualization was done by Dr. Heldt, Dr. Obrenovich and Dr. Tayahi. This chapter has been published in a peer-reviewed journal.

## Acknowledgements

First, I would like to thank my advisor, Dr. Caryn Heldt, for guidance and for ensuring that financial support was available throughout my graduate school studies. Her great genius, critical analysis, people, career and time management profoundly influenced and inspired me to overcome the challenges I encountered during my research. I'm grateful to Dr. Heldt for giving me the opportunity to work in her research group. For funding, I would like to thank Michigan Technological University's Department of Chemical Engineering, the National Science Foundation (CAREER-1451959), Pfizer, and the James and Lorna Mack Chair in Bioengineering.

In addition, I also thank my committee members, Dr. Tony Rogers, Dr. Lei Pan and, Dr. Jeremy Goldman for accepting to be on my committee. I want to thank Dr. Jeremy Goldman specifically on providing a reference letter for a job interview. Thank you to our collaborators from Pfizer, Dr. Alex Berill, and Dr. Yulia Ivanova, for their support with funding acquisition and critical discussions about results for a portion of this research project.

I would also like to appreciate all of my colleagues in the Dr. Heldt's bioseparation laboratory, especially Dr. Xue Mi, Dr. Pratik, Dr. Dylan Turpenin and Seth Kriz, for their advice, helpful discussions, and constructive criticism. Thanks to Elliana Sempek, the undergraduate who assisted with some of the experiments for this study. Dr. Fei Long, thank you for your unrelentless and timely assistance with troubleshooting the AFM equipment and software. Your support was critical to my success.

To Prince, the most caring and supportive fiancé I could ever ask for, words cannot express how grateful I am. To my parents and siblings, thanks for your unwavering love and support. To all my friends from Nigeria and those I met on this academic journey, thanks for helping me remember why I started the Ph.D, and all the funny moments. Without a doubt, I adore each and every one of you.

## Abstract

Gene therapy is a therapeutic intervention designed to correct single gene disorders. AAV has been identified as a suitable vector for delivering therapeutic genes. However, the use of AAV has been hampered by manufacturing challenges inclusive of low virus recovery, and the presence of AAV without the gene of interest (empty capsids). To solve these problems, we characterized the charge and hydrophobicity of AAV, and surrogate viruses using chemical force microscopy (CFM). CFM uses a modified atomic force microscope (AFM) probe to measure the adhesion force between a virus particle and a functional chemistry. The virus particles to be measured are covalently bound on a gold coated glass slide.

CFM revealed the hydrophobic interaction of was used to characterize the hydrophobicity of non-enveloped porcine parvovirus (PPV) enveloped bovine viral diarrhea virus (BVDV) increased with rising sodium chloride concentration but not non-enveloped porcine parvovirus (PPV) while the inclusion of polyethylene glycol (PEG) improved the hydrophobic interaction of PPV and BVDV. Ethanol enhanced PPV hydrophobic interaction but not for BVDV. Hydrophobic dye absorption to PPV and BVDV correlated to the CFM results when ethanol was added. This is the first evaluation of virus hydrophobicity using CFM.

The charge and hydrophobicity of AAV empty and full capsids assessed by the CFM has been utilized to interpret previously unknown interactions of the anion exchange (AEX) chromatogram. Although, AEX is designed to be solely dependent on electrostatic, hydrophobic interactions seemed to prevail for AAV at lower conductivity levels. CFM may be used in the future to optimize buffers, develop and choose AEX ligands.

The isoelectric point (IEP) of SARS-CoV-2 was first experimentally established using CFM. Understanding viral transmission and adherence requires deciphering the structural, surface, and functional features of each viral protein. Viral RNA sequence modeling and protein crystals has been insufficient in determining the IEP. Thus, we experimentally measured the IEP of SARS-CoV-2 and compared it to variations of interest (VOIs).

With the novel CFM approach presented in this study, viral surfaces can be appropriately characterized, and a predictive model can be designed for selecting the solution conditions for virus purification.

# 1 Introduction and chapter summaries

## 1.1 Introduction

Gene therapy is a therapeutic intervention designed to correct single gene genetic disorders. Gene therapy corrects genetic disorders by replacement techniques that allows the insertion of engineered nucleic acids into target cells using viral or non-viral particles [1-3]. These gene replacement technique can be ex-vivo or in-vivo. Ex-vivo gene replacement involves removing target cells, treating them in-vitro with therapeutic DNA, then reintroducing treated cells into the patient [4]. In-vivo gene therapy, viral or non-viral particles with therapeutic DNA are injected into the patient [5]. According to the Online Mendelian Inheritance in Man (OMIM), there are about 5000 diseases caused by single gene mutations [6]. Gene therapy is a timely intervention that will affect these lives.

The effectiveness of gene therapy is measured by the amount of therapeutic protein expressed for the desired effects. The amount of expressed protein is dependent on successfully targeting cells of interest and expressing nucleic acid in the cells using a suitable carrier [7-9]. These carriers, known as vectors, are either viral or non-viral particles. In recent times, gene therapy facilitated by viral vectors has shown enormous success in clinical trials, and advantages over conventional medications in terms of dosage, specificity, and toxicity as a treatment option for genetic disorders [1, 10, 11]. Chemotherapy is one of the conventional treatments for genetic disorders. It uses a combination of anti-cancer medications and needs numerous treatment cycles. These treatments destroy normal cells and leak toxins into the bloodstream which can cause organ failure [12]. A comparison of chemotherapy and Kymriah, a gene therapy, was done on the therapeutic effectiveness for refractory acute lymphocytic leukemia. Kymriah is a lentivirus gene therapy that requires only one dosage to be effective. Using Kymriah, 81% of patients with refractory acute lymphocytic leukemia had complete remission after 3 months [11], whereas chemotherapy only achieved complete remission in 20-40% of patients in 6 months [12, 13]. Also, clinical trials for the treatment of hemophilia B using a high dose of adeno-associated virus serotype 8 (AAV8) have

shown to induce long-term expression of blood clotting protein, resulting in a 90% bleeding reduction in patients. These successes led to the discontinuation of the human factor IX prophylaxis replacement therapy which was administered twice weekly for these patients [13].

Adenovirus, adeno-associated virus (AAV), and retrovirus are the commonly used viral vectors for gene therapy. They have shown great efficacy in clinical trials [11, 14]. The selection of viral vectors requires the characterization of their physicochemical properties. These physicochemical properties govern the safety and biologic aspects of viral vectors when provided as therapy, as well as their compatibility with production systems. Currently, gene therapy using viral vectors is plagued with low production volumes, limited efficacy when administered due to inconsistencies in the characterization of the surface properties of the viral vectors, and presence of viral vectors without the therapeutic genes (empty capsids). Most virus purification, and virus-cell interactions are based on virus surface properties but there is limited information on how virus physicochemical properties can be characterized. Therefore, an efficient method to characterize the surface properties of viruses is required.

The work contained in this dissertation seeks to optimize gene therapy by exploring how to improve the characterization of viral vectors surface properties. The surface properties of focus are hydrophobicity and charge. These surface properties were selected amongst other viral vectors' surface properties because they determine the fate, transport, and interaction of viral vectors in a liquid environment [15-17]. The conventional methods for characterizing viruses are based on bulk particle measurements, require large sample size and highly purified virus concentrations [18], have rigorous complex steps [19], and have an assumption of homogeneity in the surface properties of viral particles. Hence, we have introduced a single -particle method called chemical force microscopy (CFM) to characterize viral vector surface properties. We have used the CFM to better understand the expected interactions of the viral vectors with virus purification systems and target cells based on hydrophobicity and charge differences. This would help improve the volume of gene therapy products with the therapeutic gene of interest (full capsids) and enhance cellular uptake of the viral vectors for increased therapeutic effects.

Also, differences in the hydrophobicity and charge of viral vectors with and without the therapeutic genes were screened. Based on the differences in these measured surface properties, viral vector purification can be optimized to remove the empty capsids vectors without therapeutic gene. Hence, improving the therapeutic benefits of the administered dose in gene therapy.

## 1.2 Chapter summaries

Chapter 1 of this dissertation contains an introduction and the overview for each chapter of this research.

Chapter 2 details the background of gene therapy and different approaches to gene therapy administration. We also discussed types of gene therapy vectors, advantages, and disadvantages of each type. Steps involved in the production and purification of viral vectors, and the role of virus physiochemical properties in the selection of purification systems are also discussed. This chapter also contains literature of current methods, limitations and description of the novel technique, and CFM used in characterizing the surface properties of viral vectors.

Chapter 3 discusses how we developed a single- particle method using CFM to characterize the hydrophobicity of viruses which determines the viral transport and adsorption in a liquid environment. The CFM method utilizes a functionalized atomic force microscope (AFM) probe and virus particles covalently bonded to a gold coated surface. Using CFM, we were able to characterize the virus surface hydrophobicity in a known solution and were able to quantify changes in the hydrophobicity due to changing solution conditions. All these was done using small virus samples. CFM with a hydrophobic methyl group was used to characterize the hydrophobicity of porcine parvovirus (PPV), a non-enveloped virus, and bovine viral diarrhea virus (BVDV), an enveloped virus. With the seeming reliability of this method, we employed CFM for characterizing the hydrophobicity of adeno-associated virus (AAV).

In Chapter 4, we demonstrate the use of CFM in optimizing the purification of adeno-associated virus (AAV) through differences in the charge and hydrophobicity of

empty and full AAV capsids. Traditional chromatography methods make use of limited knowledge about chromatographic purification of proteins for virus purification. However, virus capsids are extremely heterogeneous, and the CFM single particle method provided information on the charge and hydrophobicity differences observed across the particle population in a virus pool. CFM can detect the surface charge and hydrophobicity of viral capsids at a single-particle level and enable the comparison of surface charge between the empty and full virus capsids. The method described in Chapter 3 was used for characterizing hydrophobicity while for charge characterization, CFM probe terminated with positively charged quaternary amines was used.

In Chapter 5, we used CFM to determine the isoelectric point (pI) of severe acute respiratory syndrome coronavirus 2 (SARS-CoV-2, USA-WA1/2020, referred to as WT), an enveloped virus. Traditional determination of virus pI has focused on the bulk characterization of a viral solution. However, due to the heterogeneity of the virus capsids surface, and results obtained in previous studies in the Heldt laboratory on characterizing PPV and BVDV pI [20] using CFM, a similar method was applied in characterizing the pI of WT SARS-CoV-2. CFM determined the pI of WT to be 5.2-5.3. Using computational methods, the pI of WT obtained from the CFM was compared to two variants of interest, SARS-CoV-2, B.1.1.7, and B.1.351.

Chapter 6 concludes the dissertation with major findings from each project and discusses future work for development

### **1.3 Summary**

This chapter has been able to highlight the importance of gene therapy as well as the successes that has been reported in clinical studies employing viral based gene therapy. The significance and role of virus physicochemical properties gene therapy manufacture, and treatment efficacy has also been discussed. Furthermore, the drawbacks of conventional methods for characterizing hydrophobicity and charge, which are the surface properties of interest in this work, have been summarized. In addition, the advantages of the novel technique, CFM over conventional methods are emphasized.

## 2 Literature review

### 2.1 Overview of gene therapy

Gene therapy seeks to treat monogenic disorders through replacement of defective genes with healthy genes [21]. Beginning from the early 1990s, efforts have been made to apply the principles of gene therapy to treat genetic disorders. Successes have been recorded in the introduction of two in – vivo adeno- associated virus (AAV) gene therapy, Luxturna for treatment of human retina and central nervous system, and zolgensma for treating Leber’s congenital amaurosis and spinal muscular atrophy [1, 21]. These successes have led to the development of AAV-based gene therapy targeted for delivery in the skeletal muscle to treat Duchenne muscular dystrophy [22], and delivery in the liver to treat hemophilia [23]. While these early gene therapy successes are being theorized for the development of other therapies in treating human diseases, efforts are being truncated due to unsatisfactory findings from clinical trials [1]. Clinical trials revealed that some experimental drugs do not provide therapeutic benefits and instead produced harmful consequences, resulting in patient fatalities in some cases [24]. Despite the remarkable effectiveness of several AAV-based gene treatments, up to 50% of patients are still barred from treatment because of existing immunity against viral capsids, which is a gene delivery mechanism, and the transgene materials [25]. This is a major obstacle in the development of gene therapy. Numerous research focused on how to control the immune system of humans to ensure safe and efficient gene delivery are in progress. Recent breakthroughs and clinical trials have resulted in technical advances to bypass immunological barrier, such as the production of modified AAV capsids that escape pre-existing neutralizing antibodies [26, 27] and ways for temporarily removing antibodies from circulation [28]. Immunosuppression regimens may potentially offer a mechanism of preventing adaptive immunity to the viral vector while simultaneously bypassing pre-existing immunity, allowing the possibility repeated treatment, if required [29, 30].

There are various approaches for introducing or inserting genes into target cells. The *ex vivo* technique was employed in the initial attempts at gene therapy. For *ex vivo*,

the desired genes are delivered into the patient's cells that have been removed. For the *in-situ* technique, the desired gene is injected directly into the area of the body containing the target cells [31]. The *in vivo* strategy entails directly providing the desired gene to the patients, either with or without a carrier, for the required protein to be produced. The target and administration sites are different with this strategy[32] .

The efficient delivery of plasmid DNA to target cells, transcription and translation into protein is critical to gene therapy's objective. As a result, a carrier molecule, also known as a vector, is required for effective gene delivery. The vector must be highly specific to the target site, protective to the transgene from systemic endonuclease degradation [33], capable of delivering the requisite gene size for therapeutic effect, and manufacturable in large batches and at high concentrations [7-9]. The vector should not elicit immune responses or carcinogenic consequences once inserted in the patient [31]. Ultimately, a vector should be capable of expressing the gene over an extended period. Vectors used in gene therapy are categorized into viral and nonviral particles. The vector choice in gene delivery is determined by the type of genetic material to be delivered, the gene therapy approach followed, the amount of genetic material to be delivered, and the route of administration [34].

Viral vectors consist of a virus capsid with the genetic material replaced with a therapeutic gene [35]. Viral vectors have high gene delivery efficiency because they bind easily to target cells [2, 36], are not limited to gene delivery in only actively dividing cells [37, 38], protect the therapeutic gene from degradation; nonetheless, only small gene can be packed and delivered [39], they have high cost of production and quality control [40], pose problems of potential inflammatory and immune response [41], and can be toxic. Non-viral vectors are either chemical (synthetic) or naked (nucleic acid) NA. In comparison to viral vectors, they are less harmful, capable of transferring large gene sizes, less difficult to manufacture, cheaper, safer [42], and can be easily retrieved, or their effects reversed in case of adverse immune response [43]. However, with all these benefits they have certain limitations, including greater sensitivity to extracellular and intracellular interface, poor transfection ability, and substantially lower transgenic expression [33, 44].

The viral vectors are preferred because they are more efficient in the delivery of genetic materials through specific receptor binding on the cell surface, can preserve transgenes from degradation, and they overcome the disadvantage of chemical transfection which occurs in nonviral vectors [40].

With successes recorded in human gene therapy trials between the years 2012 and 2019, the US Food & Drug Administration (FDA) has approved three gene therapy treatments [38]. These approvals and successes in human trials have resulted in an increased interest in viral gene therapy. The increased interest has led to a high demand for reliable and clinical grade viral vectors in large quantities [45] [46]. Currently, over 70% of vectors used in gene therapy clinical trials are based on viral vector [38].

## **2.2 Viral vectors for gene delivery**

Viruses can adapt to changes in their biological environment allowing them to survive and proliferate in host cells [47]. Gene therapy using viral vectors has leveraged this characteristic by employing viruses as vectors for the delivery of genetic materials to target cells. Viral vectors are recombinant viruses that have been genetically modified by replacing their genetic materials with a therapeutic gene that will be transferred to the cell of interest [36]. Viruses are very small structures made up of DNA or RNA enclosed within a protein capsid, as shown in **Figure 2.1a**, and sometimes a lipid membrane surrounds the capsid (envelope) derived from the host cell, as shown in **Figure 2.1b**. Viruses range in size from 20 to 500 nm [37]. Each virus infects different cell types; hence, gene therapy viral vectors are chosen based on the tissue to which the gene is to be delivered.

The viral vectors have the unique ability to easily bind to the cell and insert the genetic code to produce a therapeutic protein. Despite this strength, various limitations imposed by a lack the diversity in physical and chemical properties of viral vectors have influenced cellular uptake and biologic safety. Polydispersity, shape, size, composition, side chain density, functional external surface, and hydrophobicity are some physical and chemical properties [48]. With viral vectors it is difficult to manipulate these attributes.

The limitation in viral vector sizes affects the size of transgene that can be delivered [35]. Also, because of the charge and functional external surface, viral vectors are susceptible to random insertion of the therapeutic gene, which might provoke immunological responses [49]. The vector solubility improves gene expression by making the therapeutic transgene stable throughout manufacturing and simplifies the dissociation of DNA [50]. Viral vectors possessing less amount of water-soluble hydroxyl groups and amino acids with carboxyl groups makes gene delivery difficult. Therefore, these attributes are carefully considered in the selection and manufacture of viral vectors.

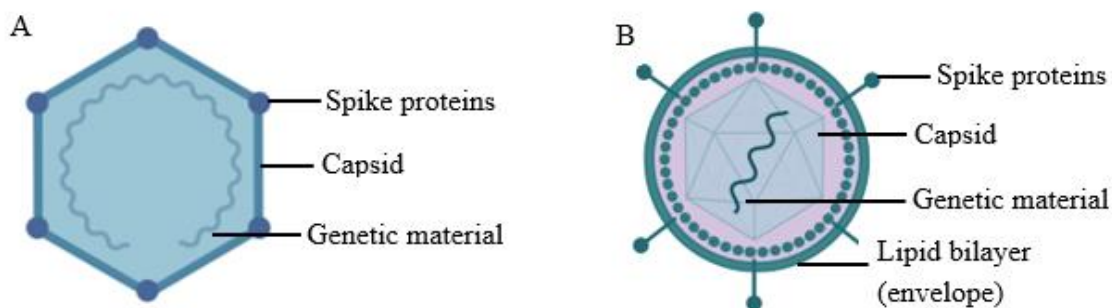


**Figure 2.1: Virus structures** (a) A non-enveloped virus (b) An enveloped virus (*created in biorender*)

### 2.2.1 Selection criteria for viral vectors

The selection of viral vectors necessitates the evaluation of physicochemical properties - attributes that pertain to physical and chemical characteristics, as well as cellular mechanism [48]. The physicochemical properties pertain to the size, hydrodynamic diameter, solubility, side chain length, and charge. These attributes govern the safety and biologic characteristics considered in the production system selection and biologic compatibility of viral vectors when administered as treatment. The molecular weight and side chain length have been studied and recognized to significantly influence cellular uptake, DNA unpacking, endosomal escape, and nuclear internalization [51]. Also, the particle size and surface charge of viral vectors affect cellular uptake and transfection efficiency [48].

One of the criteria considered in selecting a viral vector is the transgene size. Viral vectors like herpes simplex virus, vaccinia virus and baculovirus with a capacity to carry large transgenes as indicated by the DNA insert size in **Table 2.1**, are preferred because some diseases are controlled by large proteins which require larger genomes for therapeutic efficacy. In addition, delivery efficiency, stability of the transgene, and efficiency of transgene expression are considered. In **Table 2.1**, the viral vectors with transient transgene expression have a limitation of triggering unwanted immune response and generating infectious virus while those with long lasting(stable) transgene expression are preferred because they have high expression of the desired DNA in the target cell [45]. Also, all viral vectors in **Table 2.1** can transfect both dividing and non-dividing cells apart from retrovirus and vaccinia virus. Retrovirus has the ability to integrate into the cell (host genome interaction) which can lead to genetic instability, and modification in the function of nearby untargeted cells [52].

**Table 2.1** Gene therapy characteristics of viral vectors [45, 53]

Viral vector	Family	Genome	Virion diameter(nm)	DNA insert size (kb)	Infection/Tropism	Transgene expression
Adenovirus	Adenoviridae	dsDNA	80-100	36-39	Dividing and non-dividing cells	Transient
Adeno-associated virus	Parvoviridae	ssDNA	18-26	5	Dividing and non-dividing cells	Potential long lasting
Alpha virus	Togaviridae	ssRNA	60-70	12	Dividing and non-dividing cells	Transient
Herpes simplex virus	Herpesviridae	dsDNA	150-200	120-200	Dividing and non-dividing cells	Potential long lasting
Retrovirus/lentivirus	Retroviridae	ssRNA	80-130	3-9	Dividing cells	Long lasting
Vaccinia virus	Poxviridae	dsDNA	170-200	130-280	Dividing cells	Transient
Baculovirus	Baculoviridae	dsDNA	30-100	80-180	Dividing and non-dividing cells	Transient

Adeno-associated virus (AAV) vectors have become the platform of choice for *in vivo* gene therapy due to their outstanding safety profile, and high transduction efficiency of a wide variety of target tissues [54]. In 2012, the European Medicines Agency authorized alipogene tiparvovec (Glybera), the first AAV gene therapy product to treat lipoprotein lipase deficiency [55], and, in 2017 oretigene neparvovec-rzyl (Luxturna), was licensed as the first AAV in the United States [56]. The approval of these AAV therapies proved that AAV is well tolerated and deliver long term transgene expression in humans [57, 58]. Also, these approvals led to a significant increase in the number of clinical studies using adeno-associated virus (AAV) vectors for *in vivo* gene transfers. AAV technology has also been successfully used in the clinic for a range of ailments, including coagulation abnormalities, hereditary blindness, and neurodegenerative diseases [56]. Recent developments in generating therapeutically desirable AAV capsids, improving genome designs, and exploiting new biotechnologies have all contributed significantly to the expansion of gene therapy using AAV. Continued research into AAV biology, and a thorough understanding of the physicochemical properties, will provide the groundwork for future clinical trial success.

### **2.2.2 AAV biology and as a vector for *in vivo* gene delivery**

AAV is of the Parvoviridae family. It is made up of an icosahedral protein capsid with a diameter of 25 nm and a 4.7 kb linear single-stranded DNA [59]. The capsid is made up four protein of subunits, VP1, VP2, VP3, in a 1:1:10 ratio and AAP which is responsible for virion assembly activation, as shown in **Figure 2.2** [60]. The genome is flanked at the ends by two T-shaped inverted terminal repeats (ITRs), which primarily function as viral replication sources and packaging signal. The rep gene are necessary for genome viral replication and integration, while the cap gene encodes the three capsid components [56]. A third gene encodes the assembly activating protein (AAP) and is transcribed in a separate reading frame inside the cap coding region. Unless a helper virus offers replication functions, AAV stays latent in host cell DNA [59]. AAVs life cycle is

reliant on the presence of a helper virus, such as herpes simplex virus (HSV) or adenovirus (Adv) [60]. AAV has been identified in a variety of vertebrate animals, including humans and nonhuman primates (NHPs) [40]. According to current research, AAV does not cause any human illnesses [61].

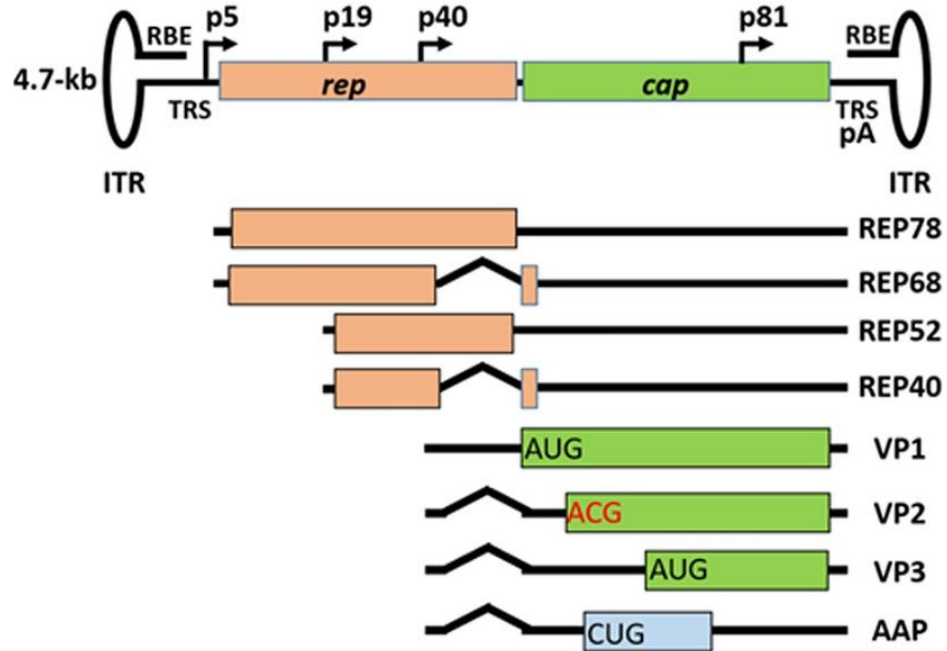


**Figure 2.2: AAV genome and mRNA transcripts.** The promoters that transcribe the *rep* gene are p5 and p19. *Rep* 78, 68, 52, and 40 are all proteins generated by the *rep* gene. The binding of *Rep* 78/68 to the RBE initiates AAV DNA replication at any of the ITRs. p40 generates VP1, VP2, VP3, and AAP mRNAs. AAP promotes native *Cap* protein trafficking into the nucleolus, where capsid formation occurs. Reprinted from [62] with permission.

Recombinant AAV (rAAV) used as vector in gene therapy comprise of same capsid sequence and structure as wild-type AAV (wtAAV) [56]. However, the encapsidated genomes of rAAV are devoid of all AAV protein-coding regions and include therapeutic gene expression cassettes. For rAAV, the only viral-originated sequences from wtAAV are the ITRs, which are required for genome replication and packing during vector production, while the remaining viral sequences are swapped with the therapeutic gene of choice [54]. The DNA of interest flanked by AAV ITRs is known as the transgene expression cassette [63, 64]. The total elimination of viral coding

sequences increases rAAV packing capacity and leads to their low immunogenicity and cytotoxicity when administered as treatment [56].

### **2.2.3 Manufacture of rAAV vectors**

The approval of some rAAV based gene therapy, and the increasing number of clinical trials using rAAV has led to a high demand of good manufacturing grade (GMP) and high concentration rAAV vectors. To meet the quality requirement for rAAV, high yield production and efficient purification systems are required. The production and purification of rAAV vectors is faced with the challenge of how to reduce production costs, and process optimization and scalability to ensure vectors for gene therapy that are safe, have high concentrations, and are economic to produce on a commercial scale. This research will focus on how to overcome some of the challenges associated with the process optimization for the purification of viral vectors.

The manufacture of viral vectors can be divided into the upstream and downstream process, as shown in **Figure 2.3**. The upstream process focuses on designing the vector, selecting a vector production method, providing the medium required for optimum cell growth, and rAAV production while the downstream focuses on the elimination of contaminants (process and product related) such as, host cell proteins, empty capsids, and free proteins through a combination of chromatographic and non-chromatographic techniques [65]. In rAAV production, the cells are lysed or broken down after infection to release the virus, this contributes host cell proteins to the virus pool [66]. Also, during production, some assembled virion contains little or no part of the transgene of interest, this is referred to as partially full or empty capsids [67]. The goal of downstream processing is to ensure the products are pure, potent and meet regulatory requirements[68].

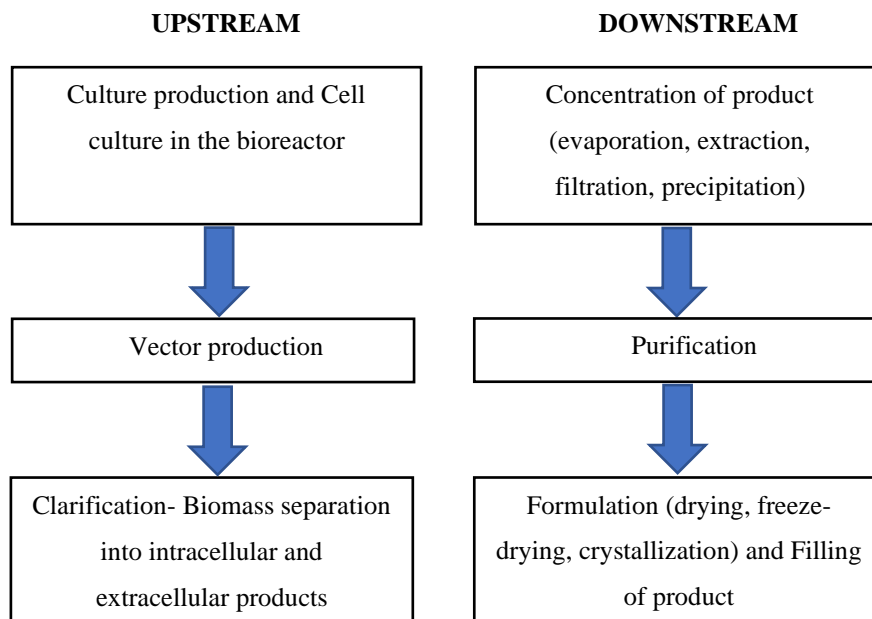


**Figure 2.3:** Flow chart showing the activities involved in the upstream and downstream processing of viral vectors [69].

The production of AAV vectors in large quantities can be done either by transient transfection, or infection of producer and stable mammalian cells or insect cells [70, 71]. The transient transfection, as shown in **Figure 2.4** is one of the most common protocols adopted in the production of rAAVs. In transient transfection method, mammalian cells are transfected with the plasmids containing the components required for the rAAV vector assembly. The transfection may be double or triple. For double transfection, the rep and cap genes are cloned in the same plasmid containing the helper function allowing for double transfection of this plasmid with the AAV ITR plasmid [72, 73] while for triple transfection, the expression cassette is cloned into a *cis* plasmid carrying the AAV ITRs, with rep and cap proteins given in *trans* plasmid, and a helper functions provided by infecting transduced cells with a helper virus or co-transfecting with a third plasmid containing other Adv genes like VA RNA, E2A, and E4 genes [72]. For the double transfection with helper virus, Hela cells are used while HEK293 cells with Adv E1A and E1B genes are used for triple transfection with helper plasmid [71]. Double or triple transfection methods not only minimizes helper virus contamination in rAAV stocks, but

they also result in higher virus titers resulting from improved cell viability [70]. Transient transfection also offers advantages of generating high quality rAAV vectors, and flexibility with adopting the protocol to the production of various rAAV types [72] but is laborious and has limitations of scale up due to difficulties in adopting the protocol to bioreactor settings [74]. Transient method is also associated with high production cost due to the large quantity of plasmid required for transfection. Due to the difficulty of scaling-up transfection methods, research efforts were focused on the creation of rAAV producer cell lines.

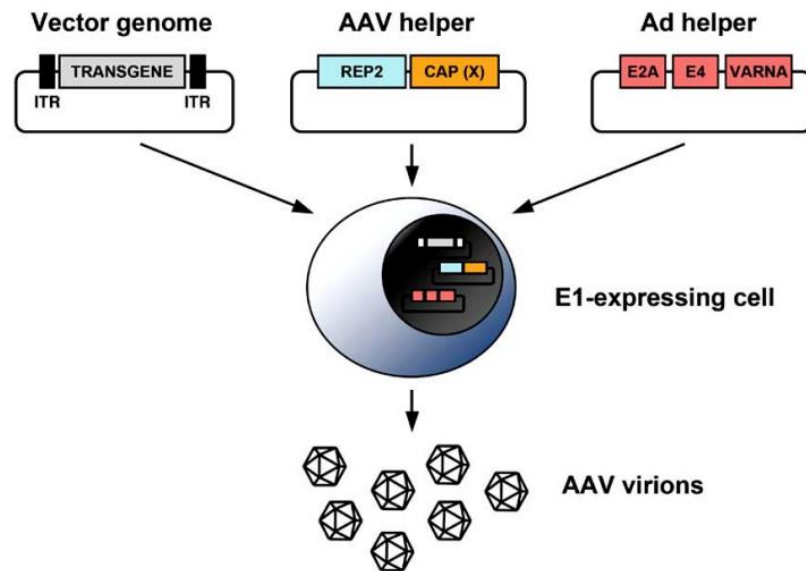


**Figure 2.4: Production of AAV by triple transfection using HEK293 cells.** The first plasmid contains the vector genome, which is the transgene expression cassette, flanked by the ITR. The AAV helper which is the second plasmid contains the *rep* and *cap* of the serotype to be produced. The third plasmid which is the A helper consists of the genes which supports AAV replication. For the double transfection, the second and third plasmid are cloned into a single plasmid. Reprinted from [70] with permission.

For the producer and packaging cell line method, all components necessary for rAAV production, namely the *rep* and *cap* genes, as well as the genome of the vector carrying the expression cassette of interest, are incorporated in the genome of a producer cell line [75]. To facilitate the production of rAAV, a helper virus, generally wtAdv, must be infected [70]. A packaging cell line varies from a producer cell line in that it only carries the *rep* and *cap* genes from the desired serotype [70]. As a result, in addition to the

helper virus, a second virus containing the vector genome is needed, see **Figure 2.5**. In comparison to the transfection method, the packaging and producer cell line method, offer a high potential of scale up by eliminating the transfection stage. However, they are less flexible in terms of switching rAAV type being produced. Also, for the vector produced to be GMP-compliant, the removal of the helper virus from the final product must be properly confirmed.

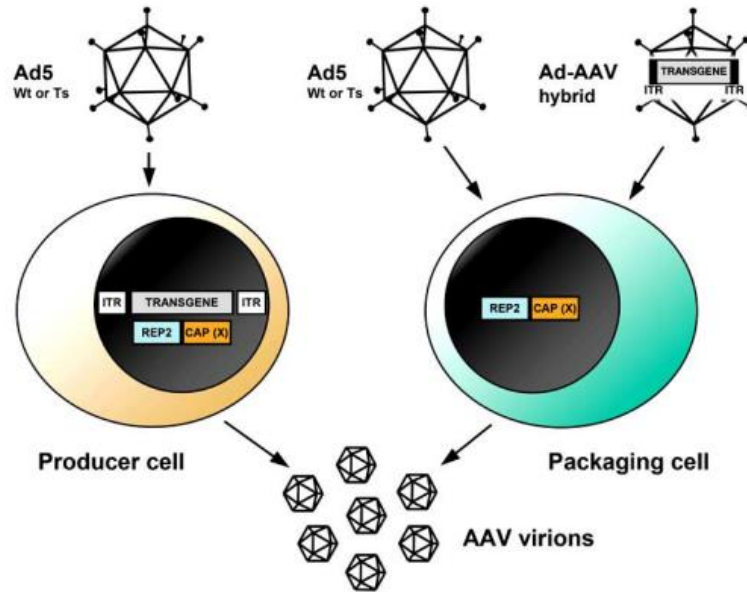


**Figure 2.5: Production of AAV in producer and packaging cell lines.** Producer cell line comprises of transgene expression cassette, and the *rep* and *cap* genes which is then infected with a helper virus to induce AAV replication. The packaging cell only consists of the *rep* and *cap* genes while the transgene expression cassette and helper function is provided by virus transduction using Adv. Reprinted from [70] with permission.

For rAAV production, regardless of the method used there is a problem of low percentage of viral vectors containing the transgene of interest (DNA) (only about 40%) [76] thus, resulting in low titers. The host cell proteins, high volume of empty viral vector capsids, and contaminants from helper virus, usually leads to rigorous purification requirements. Empty viral vector capsids increase dosage required for the gene therapy effectiveness, because the dosage is determined by the quantity of full capsids.

Administering large quantity of capsids into the patient can induce an immune response, which is detrimental to the effectiveness of therapeutic response [15]. It also can inhibit the gene delivery of the full vectors by competing for binding site in the targeted cell [77]. Therefore, the empty particles need to be removed from the full virus pool.

To facilitate pre-clinical and clinical AAV gene therapy studies, high-quality vector preparations are needed. Beyond production, good purification methods are required to obtain high quality rAAV. Different purification techniques which are scalable and GMP-compliant for rAAV vectors have been established in recent years. These methods are either non-chromatographic – density gradient-based [78], and precipitation [79, 80] or chromatographic – based on physicochemical properties like charge, hydrophobicity and affinity for different matrices [65]. Since there is minimal knowledge on how viral surface characteristics like charge and hydrophobicity may be consistently measured and translated to enhance virus purification, most virus purification techniques are based on protein purification processes. Although, viruses contain proteins, they are not only proteins which makes their surface characteristics completely different from that of proteins. Viral vectors are completely different from proteins in terms of size, charge, and hydrophobicity [16]. The adoption of protein purification techniques for viral vectors have led to low production yields. Therefore extensive modification of protein purification techniques is required for use in viral vectors purification. The work presented in this research, focuses on measuring charge and hydrophobicity of viral vectors to improve their purification using chromatographic techniques.

#### *2.2.3.1 Purification of viral vectors using chromatography*

Chromatographic techniques purify the virus based on the interactions resulting from physicochemical properties differences between the virus, contaminants, and chromatography ligands [81]. Since these interactions in chromatography are dominated by physicochemical properties like charge or hydrophobicity [82], a thorough understanding of how these viral vectors surface properties can be measured and applied to chromatography is essential for designing efficient chromatographic purification systems [83]. Chromatography is the widely used method for purifying viral vectors because it can be used on a large scale as compared to non-chromatographic methods [84]. Chromatographic purification stages are selected and optimized to enhance AAV

recovery while reducing the percentage of contaminants in form of HCP, cell culture media proteins, and empty virus vectors. The first chromatography stage which is the capturing step, utilizes charge or affinity-based ligands [85] while the next stage, which is the polishing step may be charge, hydrophobicity or size exclusion chromatography [86, 87].

Chromatography in which adsorption of the viral vectors to the stationary phase is controlled by ionic interaction is referred to as ion-exchange chromatography (IEX). In ion-exchange chromatography, a stationary phase containing either anions (AEX) or cations (CEX) is used to selectively absorb viral vectors while in a mixture of other charged contaminating particles [10]. The virus surface is large with multiple amino acids which have a net charge at a particular pH. The charge of the virus surface changes based on the pH of the mobile phase [88]. Careful manipulation of the pH and salt concentration in the mobile phase buffer allows for virus binding to the stationary phase. In general, viruses are bound at low salt concentrations to prevent charge shielding and eluted at high salt concentrations [86, 89]. With high salt concentration, the ions from the salt will compete for the surface of the stationary phase with the viral vectors, resulting in the detachment and elution of the viral vector. For virus elution from AEX using NaCl, the Cl<sup>-</sup> ions will compete for the surface of a positively charged ligand, displacing the bound negatively charged viral vectors while the Na<sup>+</sup> will bind to the negatively charged ions of the viral vector making them neutral and will lead to their elution. AEX or CEX has been used to purify AAV1 [90], AAV2 [86], AAV4 [91], AAV5,6,9 [92], and AAV8 [93].

AEX has been shown to be a feasible method in separating empty and full capsids for the majority of adeno-associated virus (AAV) serotypes [94, 95]. The isoelectric point (otherwise known as pI, is the pH at which the net charge of the virus is zero making it electrically neutral) of many AAV serotypes has been quantified with the full AAV capsids have a slightly lower pI than empty AAV capsids owing to the presence of negatively charged DNA inside the full capsid [96]. It has been shown that by manipulating the elution conditions based on the small difference in surface charge, the empty capsids can be separated from the full capsids using IEX [90, 93].

Using differences in the surface hydrophobicity of the viruses, contaminants, and ligand, chromatographic purification is achieved using hydrophobic interaction chromatography (HIC) [97]. At the interface between a hydrophobic surface and water molecules, there is a re-arrangement water molecules which manifests as a hydration layer, see **Figure 2.6a** [98]. In HIC, viruses are absorbed to the hydrophobic ligand on the chromatography column using high concentrations of kosmotropic salts in the loading buffer, and are desorbed by lowering the salt concentration in a linear or stepwise manner in the elution buffer [99]. The kosmotropic salts as described by the Hofmeister series are those salts which promotes hydrophobic interaction by inducing the salting-out effects. The salting-out effects refers to the ability of the salt ions to be solvated by water molecules which limits the amount of water molecules available to interact with the charged virus residue. In the condition of limited virus interaction with water, the virus hydrophobic residue can interact with the hydrophobic ligand, as shown in **Figure 2.6b**.

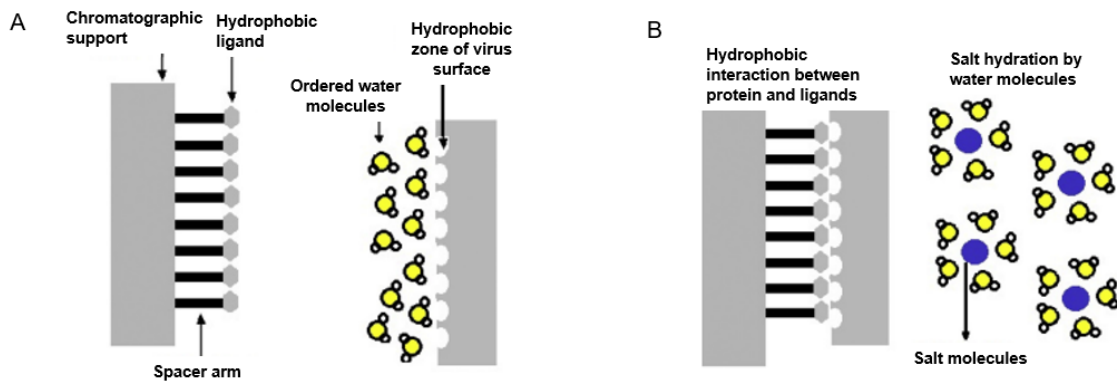


**Figure 2.6: Hydrophobic interaction chromatography.** (A) The surface of viruses covered with water hydration layer, making the viruses unable to interact with the hydrophobic ligand. The hydration layer is formed by the rearrangement of water molecules. (B) Effect of salt on the hydrophobic surfaces – the addition of salts results to a dehydration of the virus surface causing an exposure of the virus hydrophobic surface. This allows an interaction with the hydrophobic ligand. Reprinted from [100] with permission.

The first systematic observation of the effect of the ionic strength on biomolecules was carried out by Franz Hofmeister. This resulted in what is known as the Hofmeister effects, which is also an ionic strength effect. In his experiment, he categorized ions in a

sequence (Hofmeister series) from strongly hydrated ions kosmotropic ions to weakly hydrated ions, based on the density of their surface charge and affinity for water molecules [101], as shown in **Figure 2.7**. Kosmotropic ions are strongly hydrated, stabilize protein and are responsible for salting out of proteins while chaotropic ions are weakly hydrated, destabilize protein and cause salting in.

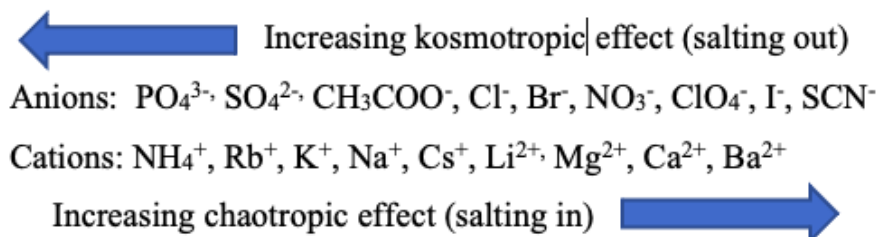


**Figure 2.7:** Schematic Hofmeister series showing the effect of anions and cations on protein precipitation

The chromatography that separates viral particles from protein and other contaminants using a reversible interaction based on biospecific (e.g., antibody-antigen, enzyme-inhibitor) or non-biospecific (e.g., protein- metal ion) interaction a specific ligand attached to a chromatographic stationary phase is the affinity chromatography [102]. The ligands can be made from heparin [103, 104], A20 monoclonal antibody [73], AVB Sepharose (ilama antibody conjugated to Sepharose) [105, 106], and mucin [107]. The viruses binds to the affinity ligand, forming a complex while the impurities flow through [108]. The bound viruses are eluted through the manipulation of the mobile phase pH and ionic strength. Purification by affinity chromatography is highly selective, resulting in a considerable recovery of biologically active material. Affinity chromatography interaction is reversible [95]. Using AVB Sepharose, rAAV vectors of the serotypes 1, 2, 3, 4, 5, 6, 7, 8, and rh.10 and 12 have been purified . The rAAV was loaded on the AVB sepharose column using a load buffer of 1X phosphate-buffered saline (PBS), 1 mM Magnesium chlordie ( $\text{MgCl}_2$ ) and 2.5 mM potassium chloride (KCl) (1X PBS -MK). 1X PBS-MK was used as the wash buffer, and 0.1 M sodium acetate and 0.5 M NaCl pH 2.5 was used as the elution buffer. AAV vectors were neutralized immediately with 1 M Tris-HCl pH 10 [109].

Since some AAV serotypes do not bind to heparin, mucin and antibodies, another form of affinity chromatography was developed based on the presence of proteins with metal affinity tag on AAV surface [110, 111]. This type of affinity chromatography is referred to as the immobilized metal ion affinity chromatography (IMAC). Metal immobilization on the chromatography column is by chelation [112]. IMAC exploits the bond formed between the virus capsid proteins like histidine and metal ions when mobile phase buffer is between pH 6-8 [112]. The proteins on the virus capsids that have affinity for the metal ions aids retention on the stationary phase column. Adv has been purified using affinity chromatography based on the binding of their particles to the zinc ions that were covalently bond to the stationary phase with a chelating ligand like iminodiacetic acid. Elution was achieved by adjusting the pH or using additives like imidazole, which compete for binding sites on the stationary phase [102]. Also, using an IMAC with positively charged metal affinity ligand, empty and full AAV2 and AAV8 capsids was separated. Overall, the data indicated that the ligand's positive charge increased AAV retention, while metal affinity modulated separation of empty and full capsids [113].

Multiple binding interactions are used in another form of chromatography. This is known as mixed mode or multimodal chromatography (MMC) [103]. It is based on the use of chromatographic ligands capable of providing a variety of interactions between the ligands and the viral pool. The retention of viral capsids to the ligand is made possible by the multiple sites on the ligand that can contribute different sorts of interactions as illustrated in **Figure 2.8**. Typically, the contact consists of electrostatic, hydrophobic, hydrogen bonding, and affinity interactions [104]. These interactions may be used alone or in combination to boost selectivity and specificity [105]. The surface chemistry of the viral vectors and the overall conditions, such as mobile phase ionic strength and pH used in MMC, defines the strength of the individual interactions.

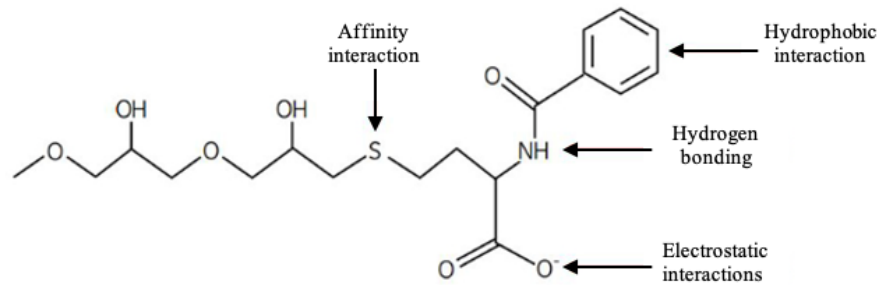


**Figure 2.8:** A mixed mode chromatography ligand with different interaction sites [114].

### 2.2.3.2 Common additives used to enhance virus purification

Several additives are used to improve selectivity and ensure the stability in the purification of viral vectors. These additives influence selectivity by improving solubility, inducing changes in the conformation, and promoting bound virus elution. Although they have positive effects, at high concentrations they can inactive or denature the viral particle. In **Table 2.2**, the typical concentration and effects of these additives in virus purification are as outlined. These additives alter ionic and hydrophobic interactions in the purification of viral vectors. In this research, ethanol and PEG was used as additives to induce changes in virus hydrophobic interaction as detailed in **Chapter 3**.

**Table 2.2** Information on additives classes, types, concentration, and purpose [115].

Additive	Types	Concentration	Purpose
Salts	CaCl <sub>2</sub> , MgCl <sub>2</sub> , NaCl, KCl, (NH <sub>4</sub> ) <sub>2</sub> SO <sub>4</sub> , NaCNS, up to 8M urea	50 – 150mM	Maintain ionic strength. May also affect conformation. Decrease hydrophobic effect in solution and leads to dissociation. Ca <sup>2+</sup> increases stability and Mg <sup>2+</sup> decreases stability.
Alcohols	Ethanol, n-butanol, 2-propanol,	10-90%	They are known as chaotropic agents because they alter the virus's structure and may cause the lipid layer of enveloped viruses to disintegrate. They disrupt non-covalent bonds like hydrogen bonds and the hydrophobic interactions between the virus, contaminants, and the binding surface, hence interfering with the hydrophobicity of the viral surface. Increased concentration may result in viral inactivation. An ionic bond is formed between the virus phosphate group and the positive ions (Na <sup>+</sup> , NH <sub>4</sub> <sup>+</sup> ), this results in virus precipitation.
Detergents	Tween 20, Triton X-100, Deoxycholate	0.01-1%	Solubilization of poorly soluble proteins
Glycerol		5-10%	Stabilizes the membrane. Surface tension decrease of water
Sucrose or glucose		25mM	Stabilizes the membrane
Reducing agents	DTT, DTE, 2-Mercaptoethanol	1 -10mM 0.05%	Reduce oxidation damage
Ligands, metal ions	Mg <sup>2+</sup> , ATP, GTP	1-10mM	Stabilizes the membrane
Poly-ethylene glycol (PEG)		5-20%	They are nontoxic and non- ionic water-soluble polymers. The type with higher molecular weight is preferred but less favorable due to high viscosity. It is used for virus precipitation. With increasing PEG concentration, virus concentration is increased till solubility exceeds the maximum and precipitates. It precipitates viruses based on the principle of volume exclusion.

Although viral vector purification using chromatography is scalable, it requires optimization because of low virus recovery volumes obtained using this technique. The recovery volumes are low because much of the chromatography ligands surface area is concealed and inaccessible to the large virus particles [102]. Most chromatography ligands were designed for proteins which have smaller sizes when compared to viruses making it possible for proteins to be trapped in the ligand cavities. However, since

viruses are large, they cannot fit into the narrow cavity sizes created for proteins. Since chromatographic purification is based on molecular interactions, it is possible to optimize chromatography to increase virus recovery volumes after purification. In this research, the chromatography methods that will be investigated for optimization are those in which viral vector charge and hydrophobicity govern the interaction with the chromatography ligand. These chromatography methods are based on ionic, and hydrophobic interactions only.

### **2.3 Virus surface chemistry**

Virus interactions are governed by the chemistry of the outer most proteins or lipids present on the viral surface [116]. The surface chemistry has some effects viral vectors manufacturability, safety, and biological compatibility with cells [117]. The viral charge and hydrophobicity are the two most important surface features because they are responsible for the transport and binding behavior of the viruses in a liquid environment [16, 118]. Charge and hydrophobicity respectively influence the electrostatic interaction and solubility of viruses. The charge and hydrophobicity of the virus are highly influenced by the solution conditions, including ionic strength and pH [119]. An understanding of the charge and hydrophobicity would help in the optimization of systems where these surface characteristics play a role.

The charge and hydrophobicity of viral vectors play essential roles in the design, selectivity, and scaling up of purification systems [18]. Therefore, a thorough understanding of viral charge and hydrophobicity is required for the design and selection of pH, ionic strength, and chromatography resin/ligand type for virus purification. This understanding of virus charge and hydrophobicity and its application to virus purification will help to improve the virus recovery volumes and eliminate contaminants for gene therapy products. The goal of this research is to help in the optimization of virus purification which would increase recovery. Increased viral recovery would result in less expensive gene therapies, thus increasing the accessibility to treatments for genetic illnesses, potentially saving lives.

### 2.3.1 Hydrophobicity

Hydrophobicity is a surface property that is responsible for low solubility of virus, their adherence to hydrophobic surfaces, and propensity to aggregate in an aqueous environment. Interactions enhanced by virus hydrophobicity are prevalent at short ranges of separation and become dominant at high ionic strength [120]. The nonpolar aliphatic or aromatic amino acids of proteins in capsids of the non-enveloped virus or glycoproteins in the lipid bilayer of enveloped virus are principally responsible for the virus surface hydrophobicity [121]. There are different theories which have been used to analyze the behavior of hydrophobic molecules in an aqueous environment.

Hydrophobicity has been defined using the water ordering and the cavity formation theory. The classical view, as developed by Frank and Evans, describes hydrophobicity as the characteristic of a hydrophobic molecule that causes the strengthening of hydrogen bonds in water, resulting in the formation of a cage-like cluster surrounding hydrophobic molecules [122]. Using nuclear magnetic resonance (NMR), based on the classical view, it was observed that the presence of a hydrophobic molecule in an aqueous environment inhibits the motion of water molecules [123], and effects a large and positive change in free energy,  $\Delta G$ , due to a large and negative change in entropy,  $\Delta S$ , at room temperature [124]. This large and positive change in free energy signifies a weak interaction between the hydrophobic molecule and water. The dynamic view on water ordering investigated the orientation of water around hydrophobic molecules utilizing neutron diffraction [125], infrared spectroscopy [126], and molecular dynamic simulations [127]. These investigations showed that a hydrophobic molecule reduces the rotation of water molecules surrounding it, with no influence on hydrogen bonding. From this information, we might be able to have an understanding of the interaction that goes on between a virus and an hydrophobic chromatography ligand in the presence of buffers.

According to the cavity formation theory, a molecule, whether hydrophilic or hydrophobic, produces a cavity in the presence of water. For hydrophobic molecules, the

cavity formed in the water structure is the outcome of hydrogen bond manipulation by the molecule [128]. Cavity formation theory characterizes hydrophobicity as the impossibility of a hydrophobic molecule to be accommodated by a cavity generated in the water structure [129]. Since hydrophobic molecules cannot be accommodated in the water structure cavity, the interfacial area between hydrophobic molecules and water molecules decreases. As a result, hydrophobic molecules have a poor solubility and generate a large and positive enthalpy change for cavity formation. [124].

The hydrophobicity of virus is typically enhanced by high ionic strength. Virus have a complex surface which possess both hydrophilic and hydrophobic patches. The hydrophilic portion interacts with water hence, preventing the exposure of hydrophobic patches. In a high ionic strength environment, the salt ions are able to manipulate the hydrogen bonds of the water structure in the virus hydration layer. This results to the exposure of hydrophobic portion on the virus which can participate in hydrophobic interactions [130]. To understand the impact ionic strength has on the of hydrophobicity on virus, MS2, QA and Q $\beta$  bacteriophages, which are common viruses that infect bacteria [131], was adsorbed to hydrophobic surfaces in the presence of 100 mM sodium nitrate (NaNO<sub>3</sub>) at pH 7. The adhesion results categorized the increase in hydrophobicity of the bacteriophages in the following order GA > Q $\beta$  > MS2. The influence of electrostatics at 100 mM NaNO<sub>3</sub> ionic strength is least significant. Hence, the adhesion of the bacteriophages was said to be as a result of hydrophobic interaction [132]. Furthermore, Hepatitis B core virus-like particle (HBc - VLP) was adsorbed to hydrophobic ligands over an ionic strength range of 0 to 0.7 M ammonium sulfate ((NH<sub>4</sub>)<sub>2</sub>SO<sub>4</sub>). The HBc - VLP adsorption increased as the concentration of (NH<sub>4</sub>)<sub>2</sub>SO<sub>4</sub> increased [133]. This shows the importance of ionic strength on hydrophobicity. To further support the contribution of high ionic strength to the adhesion of viruses using 1 – 1.25 M ammonium sulfate, AAV1, AAV5, AAV – MutC and AAV8 was successfully captured and recovered from cell culture media using a phenyl HIC membrane [134]. Understanding the significance of hydrophobicity in virus adsorption would provide a better understanding of the likely interactions taking place during virus purification. This understanding will aid in the

development of improved purification techniques and buffer compositions, which will increase viral recovery for gene therapy.

### **2.3.2 Charge**

Charge is another crucial surface property that influences the fate and transfer of viruses in a liquid environment [120]. The charge of a virus is based on the ionizable amino acids in the capsid protein for nonenveloped virus and the glycoproteins for enveloped virus [135, 136]. The net charge of the virus is based on the contributions from protonated and unprotonated amino acids in the virus capsids protein or envelope glycoprotein which results to a pH dependent electrical charged surface [137]. The net charge of virus is often described using IEP. The IEP is the pH at which the net charge of the virus is zero making it electrically neutral. At pH below the IEP, the viruses are positively charged while above the IEP, the viruses are negatively charged [88]. In a liquid environment, positively charged amino acids like lysine, arginine, and histidine becomes protonated while the negatively charged amino acids like, aspartic and glutamic acid becomes deprotonated [138].

The charge of a virus is considered to affect electrostatic interactions between the virus and other charged surfaces [132, 139]. The charge differences between the virus and other surfaces can enhance or inhibit adsorption in virus purification systems. The Derjaguin, Landau, Verwey, and Overbeek (Electrostatic) theory can be used in describing the adsorption of viruses based on electrostatic interaction [140, 141]. The DLVO theory assumes that the electrostatic double layer forces and van der Waal forces are independent. Thus, the forces can be superimposed or incorporated at the interacting distance between particles [140]. Electrostatic interactions between viruses and other surfaces are modulated by the pH and ionic strength [142]. The ionic strength controls the electrostatic interactions through its effect on the Debye length of the electrostatic potential of the liquid environment [143]. The Debye length measures thickness of the double layer [144]. The double layer is the characteristic distance over which electrons can be separated [144]. With an increase in ionic strength the Debye length is reduced and

double layer thinned while the reverse is the case for low ionic strength [145]. The solution pH affects the magnitude of electrostatic interaction by effecting changes in the charge distribution of the virus and adsorption surface [120].

Electrostatic interaction is important for virus adsorption. To highlight the importance of electrostatic interaction in virus adsorption, pseudo-typed adeno-associated virus serotype 2/8 (AAV -2/8) was purified using using cation and anion exchange chromatography exchange chromatography [146]. Pseudo-typed AAV-2/8 vector is a vector in which the AAV-2 genome is packaged in an AAV-8 capsid. Crude clarified cellular lysate was loaded using 20 mM Bis Tris Propane buffer. The AAV-2/8 particles only bound to the cation resin at pH 6 while the AAV-2/8 bound to the anion resin at pH 9. This means that the IEP of AAV-2/8 is greater than pH 6. The bound virus particles were eluted with increasing concentration of sodium chloride, NaCl (100–1000 mM). These suggests that AAV-2/8 particles are positively charged at pH 6 and negatively charged at pH 9. Hence, their adsorption and desorption from the charged membranes are based on changes in their surface charge distribution which is modulated by changing salt concentration and pH [146]. These highlights the effect of electrostatic interactions in virus adsorption to charged surfaces.

Although viruses adsorb through hydrophobic and electrostatic interactions, these interactions are generally inadequately characterized. The lack of a defined methodological descriptor to offer information on these interactions at a fundamental level contributes to the inadequate comprehension of these interactions. The goal of this study is to develop a reliable method for characterizing the charge and hydrophobicity of viruses in physiologic conditions employed in virus purification, allowing for improved modification and interpretation of virus interactions.

### **2.3.3 Typical methods for virus surface chemistry characterization**

The characterization of viral surface characteristics has been plagued by inconsistencies in the many methodologies used. The nanometric size and complexity of the viral surface makes most existing approaches for virus characterization incapable of

accounting for the changes effected by the liquid environment on the virus. The ionic strength and pH of the virus liquid environment being a major determinant for changes in the virus surface chemistry. A surface characterization technique that can adequately measure changes resulting from ionic strength change and pH shift would be very instrumental in virus surface characterization. In this section, the existing methods for evaluating viral hydrophobicity and charge will be explained, as well as their limitations. A proposed technique, chemical force microscopy (CFM) which allows the single particle probing of viral charge and hydrophobicity will be described as well.

#### *2.3.3.1 Hydrophobic interaction chromatography (HIC)*

HIC is a critical technique that enables the characterization of virus hydrophobicity based on their retention and elution from a stationary hydrophobic ligand. HIC is a well-established method for characterizing protein hydrophobicity [147-149] and has also been applied to virus [16].

In quantifying virus hydrophobicity using HIC, the relative hydrophobicity of minute virus of mice (MVM), and MVM- virus like particles (VLP) was characterized using a Tosoh TSK Phenyl column. MVM and MVM- VLP were assigned hydrophobicity based on the normalization of eluting salt concentration of the virus to the eluting salt concentration of a protein standard, with the lowest hydrophobicity given a rating of zero. The lowest value corresponded to the hydrophobicity of ribonuclease A (RNase A). The relative hydrophobicity values of MVM and MVM-VLP were 0.28 and 0.35 respectively, indicating MVM-VLP is more hydrophobic than MVM [150]. Using the relative hydrophobicity value, the hydrophobicity of bacteriophages, PP7 and  $\phi$ 174 was also calculated as 0.61 and 0.18 respectively [130, 150]. From these hydrophobicity characterization examples, we see that the hydrophobicity is based on bulk solution calculations and the hydrophobicity of individual particles are not accounted for. Also, the presence of sample impurities can affect the final overall hydrophobicity values obtained. This is because if the impurities are hydrophobic, they can compete for binding on the hydrophobic column resulting to less virus particles bound. If less virus particles

are bound, the concentration of salt required to elute the virus would be different. Also, there is a possibility that the salt concentration used in eluting the virus would also elute impurities. Making this method unreliable.

Although, HIC has been used to characterize the relative hydrophobicity of some viruses, this method is flawed. The HIC method relies on a relative hydrophobicity scale made with protein references as a baseline for comparison, any errors in the experimental determination of the reference protein standard might affect the other results. In addition, there are different hydrophobic ligands with varying degrees of hydrophobicity, these differences would result in different retention and selectivity of the virus surface. Hence, this might affect the relative hydrophobicity value assigned to a virus. Furthermore, the retention and elution of the viruses are modulated by the buffer compositions, and conditions. Changes to the buffer conditions and composition would effect changes in the binding behavior of the viruses making this method unreliable. The high salt concentrations are capable of inactivating the virus rendering making it uninfecious. The high salt concentrations utilized for HIC is also capable of affecting the virus integrity [151]. Changes to the capsid integrity can falsify the obtained hydrophobicity result obtained. For these reasons, a hydrophobicity characterization method that wouldn't affect virus capsid integrity during measurement and that can accommodate changes in the virus surface hydrophobicity due to changing solution conditions is required.

#### *2.3.3.2 Partitioning – aqueous two – phase systems (ATPS)*

Aqueous-two phase system is a fluid separation process that relies on partitioning based on the incompatibility of two aqueous solutions [152]. The aqueous solutions are formed from a combination of two polymers or a polymer and high concentration salt [152]. The common combinations for the ATPS systems are either polyethylene glycol (PEG) - dextran or PEG – salt systems [153]. Citrate, phosphate, or sulphate salts are used to allow the salt ions to capture water molecules [154] and increases the hydrophobic response of the ATPS [152]. The salts are able to effect salting-out effect

which causes the virus to precipitate and migrate from the salt phase to the PEG phase. ATPS has been used to purify and separate biomolecules from impurities [152, 155]. The partitioning of biomolecules in ATPS is driven by various interactions include hydrophobic and electrostatics interactions [155, 156]. As a result, ATPS partitioning has been used to characterize the hydrophobicity and charge of the virus surface. In ATPS surface characterization for biomolecules, the partitioning coefficient plays a large role. This is because partition coefficient in ATPS provides an equilibrium correlation between the top and bottom phase [152]. The partitioning coefficient is influenced by the polymer molecular weight, concentration, type of salt and concentration, solution pH and temperature [157]. Hence, changes to the factors that affect partitioning can impact the phase where the biomolecule partitions, and how the surface chemistry is characterized.

The cross partitioning of ATPS with PEG-salt in pH ranging from 4.5 – 6.5 was used to determine the isoelectric point for PPV and BVDV. The volume and virus concentration in the top and bottom phase was used in calculating the partitioning coefficient of PPV and BVDV at the different pH tested. The partition coefficient is a ratio of the virus concentration in the top phase to virus concentration of the bottom phase. A plot of partitioning coefficient and pH was obtained and IEP of 5.4 and 4.2 was determined based on the inflection point of the curve for PPV and BVDV respectively [158]. The results showed that at a pH greater than the IEP, the virus would have increased affinity to the PEG rich phase due to positive dipole moments [159]. When the virus is at a pH below IEP, the virus particles are positively charged and stay in the salt phase that contain negatively charged ions. However, at pH above the IEP, the virus is negatively charged making it repel the negatively charged salt ions and partitioning to the PEG rich phase. However, this method is not completely reliable because virus partitioning in ATPS is not purely dependent on the charge differences between the salt and PEG phase. There are hydrophobic interaction contributions from the PEG rich phase that contributes to virus partitioning. Although, ATPS has advantages of being environmentally friendly, and low cost [160], it is deficient in the characterization of the surface properties of viruses. Since surface characterization using ATPS is dependent on partitioning behavior which is influenced by polymer and salt attributes which cannot be

strictly controlled in the system, surface characterization using ATPS would be inconsistent. In addition, partitioning is modulated by a combination of physicochemical properties ranging from hydrophobic, electrostatic, bio affinity, virus size, and side chain conformational changes induced by the salt ions [161]. Surface characterization based on just one possible interaction can be misleading. Also, for enveloped viruses high salt concentrations are capable to inducing envelope deformation [162, 163]. These makes the ATPS method of surface characterization unsuitable for all viruses. Hence, a surface characterization technique which can differentiate the properties responsible for the virus surface interaction and is suitable for all virus types is required.

#### *2.3.3.3 Isoelectric focusing*

Virus charge characterization in the presence of an electric field like capillary electrophoresis utilizes electrophoretic attributes of the virus and have complex steps. Hence, the need for a method of characterizing virus charge that reduces the complexities associated with methods that focus on virus electrophoretic properties. Isoelectric focusing (IEF) is a electrophoretic technique which separates amphoteric molecules like viruses and proteins according to their isoelectric point (pI) [164]. Viruses or proteins are categorized as amphoteric because they consist of the amino group which is positively charged and the carboxyl group which is negatively charged. In IEF, the charge characterization of molecules is based on their migration in a charged field under the influence of a pH gradient [164]. For IEF, the pH gradient is created across a capillary with a negative electrode immersed in an acidic solution while the positive electrode is immersed in a basic solution. The viral particles will be negatively charged when the pH is above the pI or positively charged when the pH is below the IEP. In the presence of a pH gradient, the mobility of the molecules follows electrophoresis principles until the isoelectric point is attained. When the IEP is reached, there will be no further migration of the virus particles and the narrow bands at which the migrations stop on the capillary is then excised. The common IEF formats are gel and capillary and can be coupled with

mass spectrometry [165]. The proteins in the bands can be detected using staining with silver [166], ethidium bromide or Coomassie brilliant blue [167].

The IEP of six strains of poliovirus was estimated using capillary isoelectric focusing (CIEF). The anion exchange capillary column was made of silica coated with fluorocarbon. The observed IEP for the strains were 0.5-1 pH unit lower than those obtained from the use of other IEP derivation methods [168]. The differences in IEP obtained between IEF and other methods can be associated with differences in the virus strains, presence of impurities, electrostatic interactions between the virus and other charged interface and the host cell type used for virus propagation [88]. Also, the isoelectric point of full and empty Brome Mosaic Virus (BMV), Cowpea Chlorotic Mottle Virus (CCMV) virus like particles (VLP) and their constituent protein subunits were estimated using agarose-based gel IEF. It was observed that there was a wide variance between the pI and charge distribution of the empty and full virus capsids [118]. In addition, the pI of purified empty and full rodent protoparvovirus (H-1PV) was determined using agarose-based gel IEF. The pI's reported was 6.3 for empty capsids and 5.8 – 6.2 for full capsids [169].

Although, IEF requires only a minimal amount of virus samples, there are still some drawbacks associated with this method. IEF approach is laborious, time consuming and requires specialized equipment [170]. Also, there is a possibility of electrode reactions which can lead to contaminations [171]. Highly hydrophobic viruses are also difficult to characterize using IEF because their low solubility inhibits migration through the carrier solution [170]. To overcome the challenges associated with the use of an electric field in characterizing the surface charge of biomolecules, an easier method independent on electric field was introduced.

#### *2.3.3.4 Chromatofocusing*

This is a simple and rapid technique that can be used in combination with other methods for determining the pI of viruses and protein. Chromatofocusing utilizes the retention of viruses on an ion exchange column through a pre-determined pH gradient to

define the virus behavior in IEF [172]. In chromatofocusing no electric field is applied or required to establish the pH gradient unlike the electrophoretic techniques [173].

The IEP of several viruses have been characterized using chromatofocusing. The IEP of bacteriophage  $\phi$ X174 was quantified using chromatofocus that utilized an anion-exchange column [170]. Also, using a weak anion-exchange (AEX) column, empty and full H-1PV capsids were chromatofocused [169]. The results obtained was an IEP of 6.3 for empty H-1PV capsids, and 5.8 – 6.1 for the full capsids. These results was confirmed by isoelectric focusing as 6.3 and 5.8-6.1 for the empty and ull H-1PV capsids respectively [169]. In addition, the pI of WT minute virus of mice (MVM) , and a mutant MVM was obtained using anion exchange column chromatofocusing as 4.5 and 6.2 respectively [174]. For chromatofocusing, using a weak AEX column, the ions will dissociate faster than in strong AEX column [175]. This helps to create a stronger buffering effect on the column. With this, viruses which are susceptible to pH changes can be easily characterized.

Chromatofocusing offers the advantage of simplicity in terms of eluting the virus off the column and possibility of retrieving intact virus. There is also the advantage of easy scalability, and it can also be used to predict the pI of viruses in the presence of impurities. However, a disadvantage of this method is that the pH at which the virus elutes from the column may vary slightly from the true pI. It is difficult to estimate the range of deviations, hence, the unreliability of this method [170].

The traditional methods for characterizing the charge and hydrophobicity quantify these virus properties for the bulk solution and are thus affected by the level of virus sample impurities [18] and buffer composition [119] . Also, because these traditional methods can be affected by the level of virus sample impurities, they require high virus concentration which may not be achieved in the virus purifications process [19]. Also, there is a possibility of characterizing impurities rather than the target virus particles [88]. For these reasons, a simple, dependable, and straightforward technique which is independent on high virus concentrations and that can quantify virus surface properties based on the contributions from individual virus particles is required.

#### 2.3.3.5 Dye adsorption

The dye adsorption technique involves characterizing hydrophobicity using the adsorption of molecules to a standard probe molecules which is either, hydrophobic or hydrophilic [176]. Dye compounds that absorb visible light are often utilized as probe molecules. These dyes may also have fluorescing characteristics, which may indicate whether they are bound to hydrophobic or hydrophilic molecules [177]. Rose Bengal is a rose or red colored anionic dye which belongs to the organic compound. It is hydrophobic in nature and adsorb to hydrophobic surfaces using its xanthene ring [178]. Another organic dye is the congo red. It is anionic and is used for hydrophobicity characterization due to its aromatic rings [179]. Nile blue is a cationic dye that has a hydrophilic amino acid which gives it an affinity for hydrophilic surfaces [178]. 8-anilino-1-naphthalene sulfonate (ANS) is a common fluorescing dye used in hydrophobicity characterization. ANS is a fluorescent blue colored dye. The naphthalene and aniline ring are hydrophobic giving ANS its high affinity for hydrophobic patches on proteins or virus. ANS does not fluoresce in water or polar environments but becomes fluorescent when bound to hydrophobic patches [180]. The dye adsorption method has been found useful in the characterizing the relative hydrophobicity of biomolecules and nanoparticles because it is easily applicable to nanosized materials, and has shown enhanced selectivity with increasing molecule surface area, and concentration [178]. Using dye adsorption, the hydrophobicity of protein [16, 181], and nanoparticles [176, 182] have been characterized.

In dye adsorption to quantify hydrophobicity, different methods of analysis are adopted. There is the partitioning method which uses the plot of the partitioning quotient of test molecule in test solution versus the surface area of the molecule being measured [176]. The plot is usually a straight-line, and the slope of the line gives the measure of hydrophobicity for the test molecule. The partitioning quotient is obtained based on the ratio of the mass of dye adsorbed by the molecule to that adsorbed in the test solution while the surface area is calculated with an assumption of monodispersed molecule and constant geometry [176]. With the partitioning method, the dye concentration can be kept constant while the test molecule concentration is varied. The hydrophobicity of NPs,

aqueous nC<sub>60</sub> (aqu-C<sub>60</sub>), tetrahydrofuran-nC<sub>60</sub> (THF-nC<sub>60</sub>), fullerol, nano-gold coated with citrate (Au-CIT), nano-silver coated with PVP (Ag-PVP), citrate (Ag-CIT) and gum arabic (Ag-GA) was characterized based on their adsorption of hydrophobic -Rose Bengal. The adsorption was analyzed using a plot of partitioning quotient vs NP surface area. The slope of the plot was used as a marker for the NP surface hydrophobicity. Results showed that Rose Bengal adsorbed to other NPs tested except Ag-CIT and fullerol [176]. Since hydrophobicity is based on the slope of the plot in this method, the hydrophobicity of NPs that didn't adsorb any dye could not be characterized. The final findings revealed that the procedure used to prepare the nanoparticles influenced their ultimate hydrophobicity. When synthesizing aqu-nC<sub>60</sub>, the prolonged mixing caused partial hydroxylation of the fullerene on its surface. THF-nC<sub>60</sub> had a lower hydrophobicity than aqu-nC<sub>60</sub> owing to the preservation of leftover hydrophilic THF on the surface of fullerene. The surface chemistry was altered by coatings of citrate, PVP, or GA intended to stabilize nano-Ag. CIT made nano-Ag hydrophilic, while PVP and GA rendered it hydrophobic. Also, due to the difficulty in calculating the surface area associated with this method, dye adsorption analysis using adsorption isotherm models was explored.

Common adsorption isotherm models have been used to determine the amount of dye adsorbed by a molecule. An example is the determination of the relative hydrophobicity for gold (Au) nanoparticles (NP), uncoated copper oxide (CuO) and silica NP with and without amine functionalization was quantified using Rose Bengal and Nile blue [182]. The adsorption of the dye to each NP was analyzed using Langmuir, Freundlich and linear adsorption isotherms. The results showed that CuO NP adsorbed both Rose Bengal and Nile Blue, making it slightly hydrophobic and hydrophilic. SiO<sub>2</sub> without amine adsorbed more Nile blue making it hydrophilic while SiO<sub>2</sub> with amine adsorbed more Rose Bengal making it hydrophobic. The fluorescence of 8-anilino-1-naphthalene sulfonate (ANS) dye has been used in quantifying the hydrophobicity of PPV [16] and proteins [16, 183-185]. The hydrophobicity was quantified using linear isotherm which is based on the slope of the line for the plot of ANS fluorescence versus the concentration of the test molecule [16, 186]. This adsorption isotherm method allows

hydrophobicity quantification independent of the molecule surface area. However, in selecting isotherm models for adsorption analysis, care must be taken to ensure that the model used incorporates the thermodynamic factors that are responsible for molecule adsorption.

In addition, an alternate method for analyzing dye adsorption for hydrophobicity quantification is based on determining the fluorescence or ultraviolet (UV) absorbance of unbound dye and relating it to a reference fluorescence or absorbance at fixed or variable dye concentrations. In using the UV absorbance of dye to quantify hydrophobicity, the amount of Coomassie Brilliant Blue G-250 (CBBG) adsorbed to protein was used in determining the hydrophobicity of myofibrillar proteins (MP) [186]. The binding of CBBG to proteins is attributed to the formation of an insoluble complex resulting from the hydrophobic interactions between CBBG, and the aromatic amino acid residues of proteins [187, 188]. The amount of CBBG adsorbed was quantified using the difference in the ultraviolet (UV) absorbance of a reference control and MP with adsorbed CBBG at a fixed dye concentration. This method of analysis is easy and doesn't require complicated mathematical calculation. However, the concentration selection must ensure that there will be differences between the controls and test samples at the initial and final stage. The differences in concentration between the initial and final stages allows fluorescence or absorbance differences.

Although, the dye adsorption technique for hydrophobicity determination has an advantage of being relatively easy to perform and analyze, affordable, useful for nanosized molecules with increasing surface area and concentration, it has various drawbacks. One of the drawback is electrostatic interaction interference. The dyes can be positively or negatively charged. Hence depending on the charge of the molecule being adsorbed, repulsive or attractive forces might decrease or increase the dye adsorption. Also, there is a possibility of heterogeneous adsorption sites on the molecule to be measured. This would result in an unreliable hydrophobicity characterization. In addition, the influence of the dye and molecule concentration on the adsorption kinetics may not be taken into consideration during the hydrophobicity quantification [189, 190]. This would make the hydrophobicity quantified incorrect. Therefore, a surface characterization

technique which can differentiate purely electrostatic and hydrophobic interaction is needed for biomolecules like virus is needed.

In this research, we used dye adsorption as one of the techniques to quantify virus hydrophobicity. The adsorption isotherm model was selected in analyzing the dye adsorption to prevent the errors associated with calculating the density and surface area of the virus pool. We used the Langmuir and Freundlich isotherm models.

### 2.3.3.5.1 Langmuir adsorption isotherm derivation

In this research, dye adsorption was used as a conventional method to quantify virus hydrophobicity. The results from the dye adsorption was analysed using adsorption isotherms with the Langmuir isotherm as one of the models used. The Langmuir adsorption isotherm is based on the following assumptions and equations [191]; the surface of adsorbent is made up of elementary or fixed sites, each of which can adsorb an adsorbate, surface of the adsorbent is homogenous, adsorbed molecule behaves ideally, only monolayer is formed during adsorption, no lateral interaction, and adsorbed molecules are localized.

The adsorption of molecule,  $X$  contained in a liquid with concentration,  $C_0$  to an adsorbent with vacant surface sites,  $S$  is given by **Equation 2.3.1**



Where,  $k_1$  is the rate of adsorption and  $k_2$  is the rate of desorption. To quantify the concentration of molecule,  $X$  on the surface of the adsorbent, we introduce the surface coverage parameter,  $\theta$  and another parameter  $N$  which indicates total number of sites.  $\theta$  is fraction of surface covered by molecules of  $X$ .  $1 - \theta$  is fraction of surface uncovered molecules of  $X$  or vacant sites.

Rate of adsorption,  $k_1$  is proportional number of vacant site or unadsorbed molecules,  $N(1 - \theta)$ , and represented using **Equation 2.3.2**

$$k_1 = k_1[C_0][S] = k_1[C_0]N(1 - \theta) \quad \mathbf{2.3.2}$$

Rate of desorption,  $k_2$  is proportional to adsorbed molecules,  $N(\theta)$ , **Equation 2.3.3**

$$k_2 = k_2[C_0 - S] = k_2N(\theta) \quad 2.3.3$$

At equilibrium,  $k_1 = k_2$ , see **Equation 2.3.4**, **Equation 2.3.5** and **Equation 2.3.6**

$$k_1[C_0]N(1 - \theta) = k_2N(\theta) \quad 2.3.4$$

$$\frac{k_1}{k_2} = \frac{(\theta)}{C_0(1 - \theta)} \quad 2.3.5$$

$$\frac{k_1}{k_2} = K_L \quad 2.3.6$$

$K_L$  is the equilibrium constant,  $C_e$  is the equilibrium concentration of X after adsorption.

$K_L$  can be expressed in terms of equilibrium concentration and vacant sites using

**Equation 2.3.7**. The Langmuir equation is as stated in **Equation 2.3.8**.

$$K_L = \frac{(\theta)}{C_e(1 - \theta)} \quad 2.3.7$$

$$\theta = \frac{C_e K_L}{1 + C_e K_L} \quad 2.3.8$$

An alternate way of representing Langmuir isotherm is based on adsorbed concentration of molecule X in equilibrium at the occupied sites, which is represented as  $q_e$ , and the maximum adsorbed concentration of molecule X for all available sites i.e. complete surface coverage with a monolayer,  $q_{max}$ . The relationship between  $q_e$  and  $q_{max}$  is given in **Equation 2.3.9**. Substituting the value of  $\theta$  in **Equation 2.3.8**, gives

**Equation 2.3.10**.

$$\theta = \frac{q_e}{q_{max}} \quad 2.3.9$$

$$q_e = \frac{C_e K_L q_{max}}{1 + C_e K_L} \quad 2.3.10$$

When  $C_e K_L \ll 1$ ,  $q_e = K_L q_{max} C_e$ . Most sites are open.

Linearizing the isotherm is represented using **Equation 2.3.11** and **Equation 2.3.12**.

$$\frac{C_e}{q_e} = \frac{1}{q_{max} K_L} + \frac{C_e}{q_{max}} \quad 2.3.11$$

$$\frac{1}{q_e} = \frac{1}{C_e q_{max} K_L} + \frac{1}{q_{max}} \quad 2.3.12$$

When  $C_e K_L \gg 1$ ,  $q_e = q_{max}$ . All sites are occupied.

From the linear isotherm plot of  $\frac{1}{q_e}$  vs.  $\frac{1}{C_e}$ , the intercept is  $\frac{1}{q_e}$ , which tells us about the occupied sites, the slope is  $\frac{1}{K_L}$  tells us about the vacant sites.

### 2.3.3.5.2 Freundlich adsorption isotherm derivation

The Freundlich isotherm model was also employed as a second model to analyze the dye adsorption conventional method used for quantifying virus hydrophobicity. The results obtained was compared to the unique approach of quantifying virus hydrophobicity presented in this research. The Freundlich adsorption isotherm is based on the following assumptions and equations [192]; the surface of the adsorbent is inhomogeneous and rough, there is interaction between the adsorbent and adsorbate, and adsorption is proportional to concentration. proportional to the concentration of molecule,  $E$  in the liquid.

The adsorbed concentration of molecule  $X$ , at the occupied sites of adsorbent,  $S$  is  $q_e$ .

The direct proportional relationship between  $q_e$  and the concentration of molecule,  $X$  in the liquid,  $C_e$  is given in **Equation 2.3.13** and **Equation 2.3.14**.

$$q_e \propto C_e \quad \mathbf{2.3.13}$$

$$q_e = k_f C_e^{\frac{1}{n}} \quad \mathbf{2.3.14}$$

$k_f$  and  $n$  are constants. At low concentrations, the amount of molecule,  $X$  adsorbed increases rapidly as concentration increases till it reaches a plateau at a certain concentration referred to as the saturation concentration.

$k_f$  is the Freundlich constant,  $C_e$  is the equilibrium concentration of  $X$  in the supernatant after adsorption,  $\frac{1}{n}$  is the non-linearity exponent that tells us about the strength of adsorption.

At low concentrations,  $\frac{1}{n} = 1$ ,  $q_e = k_f C_e^1$ . At high concentrations,  $\frac{1}{n} = 0$ ,  $q_e$  is independent on  $C_e$ ,  $q_e = k_f C_e^0$ . This is the plateau point on the graph. At intermediate concentrations,  $n > 1$ ,  $q_e = k_f C_e^{\frac{1}{n}}$ .  $q_e$  does not increase rapidly with increasing  $C_e$ . To find the value of  $n$  and  $k_f$ , the Freundlich equation is linearized to the log form as shown in **Equation 2.3.15**

$$\text{Log } q_e = \log k_f + \frac{1}{n} \log C_e \quad \mathbf{2.3.15}$$

The slope of a plot of  $\log q_e$  vs.  $\log C_e$ , is  $\frac{1}{n}$  and the intercept is  $\log k_f$ .  $1/n$  is the Freundlich isotherm constant for the interaction also referred to as the non-linearity exponent.  $1/n$  tells us about the strength of adsorption and surface heterogeneity of the virus. When  $0 < 1/n < 1$ , the adsorption is reversible but when  $0 > 1/n > 1$ , the adsorption is irreversible [193].

The Langmuir and Freundlich isotherm are commonly used models. However, the Freundlich isotherm has provided a better fit for most biological analysis especially those involving viruses [194]. This is mostly because the maximum adsorption capacity,  $q_{max}$  in the Langmuir model is rarely achievable due to limitations in acquiring high virus concentrations for adsorption experiments. The Freundlich isotherm provides a good fit for virus adsorption analysis because it describes the reversibility and deviation from ideality of virus adsorption processes. Unlike the Langmuir model that assumes homogeneity of the adsorption sites, Freundlich model assumes heterogeneity of the adsorption sites on the virus [195]. The Freundlich model is only valid for low virus concentrations above which it become non-linear. Hence, its suitability for our analysis due to low virus concentrations. It is also worth noting that the Freundlich model is an empirical model so most of the interactions cannot be accounted for based on the  $K_f$  value [196].

#### **2.3.4 Novel approach – single particle - chemical force microscopy (CFM)**

Chemical force microscopy is a technique that uses specific chemistries to modify an atomic force microscope (AFM) probe to allow direct investigation of chemical group interactions in surface characterization [197]. AFM is a non-optical imaging technique with spatial precision and for measuring sensitive force interactions [198]. It is an effective tool for the non-destructive surface characterization of topography, electric, magnetic, chemical, biologic, and, mechanical properties of a sample surface in air [199], liquids [200] or ultrahigh vacuum [201, 202]. Using the knowledge from interaction

forces obtained from the AFM, in-depth understanding of numerous biological and chemical process on single molecule particle level can be assessed. CFM has been used to investigate surface charge of numerous proteins, including bovine serum albumin (BSA), fibrinogen, myoglobin, and ribonuclease A [203]. To modify AFM probes, each protein was attached to the probe, and used pull off (adhesion) forces was measured on two positively charged surfaces in different solution pH. A plot of adhesion force versus solution pH was obtained for the proteins, and the point at which the concavity of the curve changes was denoted as the pI [203]. This provides an insight into how CFM can be used in characterizing the surface characteristics of viruses. Beyond modifying the surface of the probe with a biomolecule, functional chemistries can also be used for probe modification to measure force interactions of biomolecules [158, 204].

#### *2.3.4.1 Working principles of AFM*

The AFM functions by using a flexible cantilever which possesses a sharp tip attached near the end to scan across the surface of a sample in a perpendicular direction to detect the interaction force between the tip and sample [205]. During measurement on the AFM, a piezoelectric scanner ensures the lateral and vertical positioning of the mounted sample with high precision as shown in **Figure 2.9** [206]. When the AFM tip comes in contact with the sample and scans the surface, the tip is deflected due to the height of the artifacts on the sample surface, and the interaction forces between the tip and sample. The AFM tip deflection is recorded by a laser beam reflected on the AFM cantilever and transmitted to a photodiode. By actuating the cantilever in  $z$  through a feedback-controlled piezo, detected variations in cantilever deflection or oscillation are rectified to a setpoint value. The feedback loop ensures near constant vertical deflection of the cantilever to prevent large changes in the interaction forces [205]. In order to estimate the height at a particular  $x, y$  - coordinate, these corrected voltages provided to the  $z$  piezo are recorded and connected to a voltage-distance calibration standard. The cantilever scanning coordinates in the  $x, y$ , direction with a  $z$  height displacement generates 3D topographic image of the sample surface [205, 206].

The measured interaction forces between the tip and samples are mostly influenced impacted on by the size and shape of the tip, and the environmental conditions during measurement. In AFM measurements, there are long (electrostatic, magnetic) and short (oscillatory, hydrophobic) range forces acting between the tip and samples. It is important to isolate each force type to avoid recording unwanted forces [207, 208]. At high humidity, capillary forces can be generated resulting to condensation on the tip. These capillary forces can induce high interaction forces between the tip and samples. Hence, capillary forces should be avoided by constant monitoring of humidity or measurement should be performed in a closed chamber with nitrogen or argon [209].

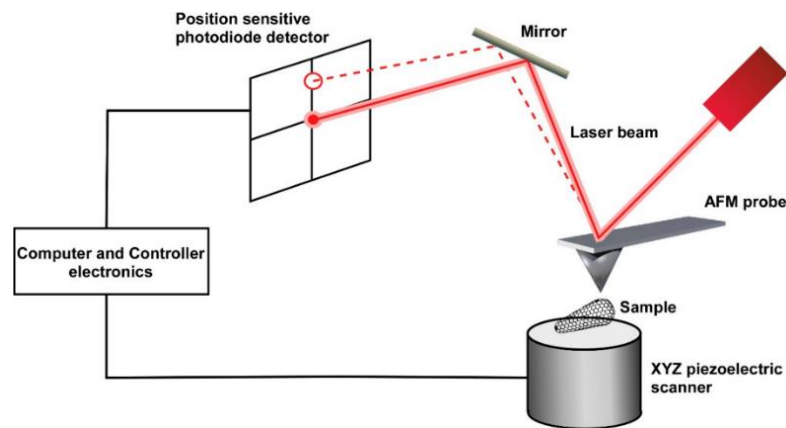


**Figure 2.9: Illustration of AFM function.** The AFM tip has a cantilever which comes in contact with the sample. The laser beam incident on the cantilever. The photodiode records cantilever deflections as the tip scans the sample surface. The cantilever deflection which is reflected on the photodiode through the mirror. The cantilever deflection and tip-sample distance is processed by the computer and controllers [210].

#### 2.3.4.2 AFM tip properties

The cantilevers used in AFM measurements have differences in terms of manufacturing materials and shape. The cantilever is typically made from silicon, Si or silicon nitride,  $\text{Si}_3\text{N}_4$  with a length of 100-200microns, and allow very small forces to be measured [206]. Cantilevers can be classified based on their shape as either rectangular or triangular. For lateral force measurements and contactless mode, rectangular cantilevers are preferred. Cantilevers with triangular shapes are easier to use and commonly used in

contact mode because their behavior to lateral forces is complex [209]. The main properties of an AFM tip are its surface energy and its radius [211]. The tip of the cantilever has a radius of curvature of about 2-50 nanometers (nm) which allows it to measure pico newton (pN) force ranges between samples.

#### *2.3.4.3 AFM measurement modes*

Technological advances have resulted to the introduction of various distinct modes in the AFM setup. Despite the fact that the majority of the AFM modes are applicable to all types of samples, they all do not produce same quality of data. The proper application of these measurement modes allows the exploration of interactions even on molecular basis. The contact and non-contact modes are the major categories of AFM set up.

The contact mode involves bringing the AFM tip in direct contact with the sample surface and allowing it to scan across while the deflection of the tip is recorded. It can be used in both air and liquid. The contact mode is used either in the constant force or constant height set up. For the constant force mode, a feedback loop is employed to move the sample or tip upward and downward while deflection is fixed. The  $z$  displacement is equivalent to the height variations in the  $x, y$  coordinate scan of sample surface. These combinations of the vertical and lateral measurements maps yield images of the sample surface topography. Frictional forces develop between the tip and sample surface due to continuous contact. These frictional forces lead to damage of the tip or samples. Hence, the contact mode is not favorable for biologic samples because of their softness. This mode may also be employed for surface topography imaging of biologic samples when minor stresses are applied [212, 213]. For the constant height mode, cantilever deflection is directly measured, and the deflection force on the tip is utilized to compute distance from surface. This measurement has no feedback loop, therefore it's good for rapid scanning of samples with minimal height variations. The constant height mode is utilized to quickly examine biological structural changes [214, 215].

The non-contact mode involves bringing the tip close enough to the sample surface at distances of about 5 – 10 nm [216]. There are different variations of the non-contact mode. Because the tip – samples have no direct contact, frictional forces can be neglected, which is a major advantage of the non-contact mode. The absence of frictional forces makes non-contact mode a preferred option in sampling biologic materials. Also, there is only a small chance of altering the surface features of biologic materials using the non-contact mode. Compared to contact mode, non-contact mode has low lateral and  $z$ -resolution, which is a major disadvantage. The non-contact mode has been used to explore cell surfaces [217, 218]. To solve the problems associated with the non-contact mode, the tapping mode was introduced.

The tapping mode is based on the non-contact mode technique. It can also be referred to as the dynamic force or intermittent contact mode [216]. Tapping mode AFM may be performed in either air or liquid. For the tapping mode, the AFM probe is oscillated above the sample using the tip resonance frequency [219] with the tip touching the sample at intervals [220]. During scanning, an electrical feedback circuit keeps the probe oscillation at a consistent amplitude. The amplitude of vibrations diminishes, and a phase shift happens when the AFM tip interacts with the sample surface. The amplitude or phase shift when the sample or the tip is moved in  $z$  -coordinate can be selected as the input parameter of the feedback loop to obtain the topographic information of the sample [220]. The main advantage of tapping mode is that it prevents the lateral and vertical shear stresses found in contact mode, which can harm the structure of the sample being scanned.

The non-contact and tapping mode are based on the oscillation of the AFM probe and its resonance frequency [221, 222], therefore can be classified as resonance modes [220]. For the resonance modes, the oscillation of the cantilever is dynamic and irregular. Also, the resonance mode requires AFM probe calibration to obtain resonance peak and adjust parameters such as driving frequency, free vibration amplitude, setpoint, and feedback gains. There are other types of the non-contact mode which are classified as the non-resonance mode. These include the lateral force microscopy [223, 224], force - volume [225], peak force tapping [226], hybrid [227], digital pulse-force [227, 228]. For

these non-resonance modes, the AFM probe oscillates very slowly, and below its resonant frequency [220]. The AFM tip contacts the sample surface in a comparable manner to the tapping mode, travelling toward and then out from the sample in the off-resonance mode. The deflection of the cantilever represents the interaction force as the tip interacts with the sample. The topographic image of the sample may be determined by regulating the peak force on the sample. The contact force between the tip and sample can be precisely detected and regulated in real time because of the slow oscillation of the AFM probe. Also, the force-distance (F-D) curve, which depicts the samples adhesion characteristics can be obtained. Off-resonance modes are therefore frequently employed in biology [229, 230].

In this research, the peak force tapping mode in liquid was utilized because it enables capturing the quantitative nanomechanical properties of samples and can be used at high scan rates. It is also able to produce high resolution mapping of the sample surface. The liquid environment makes it possible to probe the virus surface properties of interest at physiologic conditions with buffer conditions that are typically used for virus purification.

#### *2.3.4.4 Force – Distance measurement*

During the interaction of the AFM probe with a sample surface, the AFM isn't only capable to producing topographic images but is also able to map the biophysical characteristics using recorded force-distance (F-D) curves [231]. F-D curves are recorded during the movement of the piezo which brings the cantilever to the sample surface and the cantilever is then deflected and moved away from the sample surface [231]. The F-D curves is an  $x$ - $y$  plot with the  $x$ -axis as the distance which the piezo travels to bring the AFM prove in contact with the sample and the  $y$ -axis as the deflection of the cantilever. From the F-D curves the approach and retract behavior of the cantilever is recorded as shown in **Figure 2.10**. The approach curve which is when the cantilever contacts the sample provides information about the viscoelastic characteristics of the sample while the retract portion which is the separation or pull away of the tip from the sample provides

information about the adhesion force properties of the sample to the tip or molecule attached to the tip [232].

The different regions in the F-D curve shown in **Figure 2.10** represents how the tip and sample interacts. At the start of an experiment, point A, the cantilever approaches the samples, but the force is too small to be detected. At point B, the interaction between the tip and sample due to van der Waal or capillary forces increases and overcomes the spring constant of the AFM probe causing the AFM tip to come in contact with the sample. The tip remains in contact with the sample causing a deflection of the AFM probe and increasing repulsive forces if the deflection setpoint is exceeded. To prevent damage of the tip, at point C, the tip starts to retract from the sample surface. However, the tip remains in contact with the sample and is deflected downwards usually due to some attractive forces which might be hydrophobic or electrostatic. These forces are recorded as adhesion force in point D. The force from the cantilever will be strong enough to overcome the adhesion force at some tip-sample distance, allowing the tip return to the start point of measurement. The force obtained from the F-D curve is then translated into tip-sample interaction.

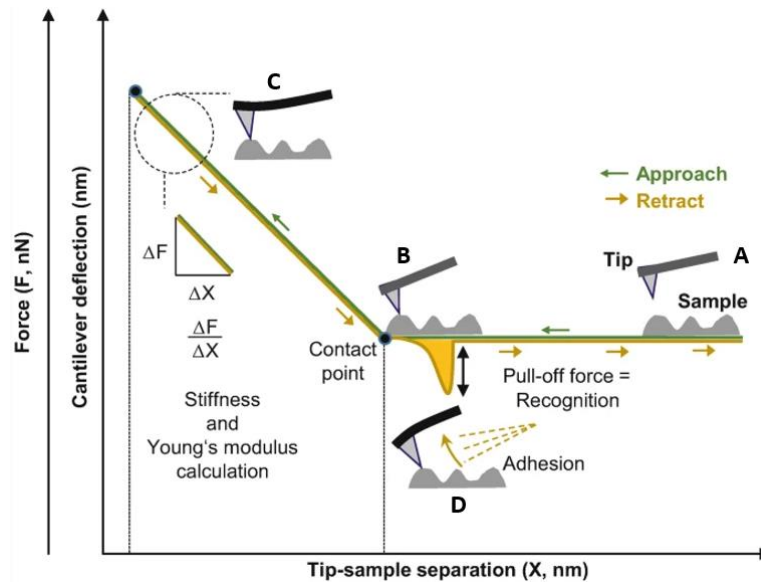


**Figure 2.10: Force-distance curve schematic.** The AFM tip comes in contact with the sample surface and exerts a predetermined loading force, resulting to cantilever deflection. The tip is held on the sample surface by an adhesive force but it eventually breaks free as the tip is retracted. Those adhesion forces can be calculated from the pull-off force region. Reprinted from [233] with permission.

The force obtained between the tip and the sample interaction has a direct relationship with the cantilever deflection [234]. Using Hooke's law as shown in **Equation 2.3.16**, the force,  $F$  is obtained using the spring constant,  $k$  of the AFM probe and the AFM probe deflection through a distance,  $x$ . The spring constant is negative in the equation because the force exerted by the probe is in the direction opposite to the distance travelled.

$$F = -kx \quad \mathbf{2.3.16}$$

The spring constant of the AFM probe is usually experimentally determined at the start of the experiment using the thermal fluctuation by obtaining the thermal noise spectrum of the cantilever deflection of the natural frequencies of oscillation [235].  $x$  is obtained using **Equation 2.3.17**.

$$x = z - \Delta z \quad \mathbf{2.3.17}$$

Where,  $z$  is the distance between the AFM probe at rest and the sample surface while  $\Delta z$  is the summation of cantilever deflection and sample deformation [232].

Using the AFM, probing single molecule have becoming possible. The single molecule measurements enable the probing of biologic molecules in their natural environment to reveal biophysical and biochemical interactions, and properties that would otherwise have been impossible for an individual molecule [200, 236, 237]. The single particle measurements allow the study of interaction between distinct species without damage their natural form. Since the AFM probe can be modified with chemistries and ligands of interest, the single particle measurements allow the probing of the adhesion forces between biomolecules and modified AFM probes. Using single-molecule AFM, the isoelectric point of PPV and BVDV have been quantified based on their interaction with AFM probes modified with positive and negative charged chemistries [158]. Also, the hydrophobicity of PPV and BVDV using the single-particle measurements has been reported [200].

Single – particle CFM offers an advantage of characterizing virus charge and hydrophobicity at a nanoscale while also being able to concurrently visualize the virus topography. The CFM allows the use of trace amount of virus volumes and does not require extremely high virus concentration for measurements. With the single – particle

CFM, the heterogeneity in the surface characteristics of the virus samples can be observed, and the overall quantified charge or hydrophobicity would be based on the contributions of particles in the virus pool. Since, the topographical and dimension of the virus particles can be observed during measurement, the effect of sample impurities on the surface chemistry characterization is negligible.

The viral samples utilized for CFM measurements were immobilized on a gold coated glass slide in this research, and the AFM probes were modified with charge and hydrophobic functional groups. The entire technique for probe modification and viral immobilization is found in **Chapter 3 - 5**. This surface chemistry analysis provides significant information for enhancing chromatographic purification procedures that rely on viral charge and hydrophobicity. The charge and hydrophobicity data may be utilized to choose a suitable chromatography ligand. It would also help in the selecting the order in which various chromatography types can be mixed depending on how they affect the viral surface characteristics. Furthermore, because CFM can be measured in an aqueous environment, CFM may be utilized to optimize the buffer compositions and conditions used for viral purification.

### **3 Virus surface hydrophobicity characterization using chemical force microscopy**

#### **3.1 Introduction**

Viruses are nanometer-sized particles that consist of encapsulated genetic material. Non-enveloped viruses are protein shells that contain genetic material, whereas enveloped viruses have both protein capsids and a lipid bilayer [238]. Viruses exist at a unique nanometer- size scale where thermal and electrostatic energies converge [239, 240]. This makes virus biology not only unique but also makes measuring many of the physicochemical properties of viruses very difficult in this noisy environment. Virus physicochemical properties govern their biological responses to virus attachment, penetration, uncoating, expression, assembly, and release [241, 242]. Measuring the physiochemical properties of viruses, which are affected by ionic strength, pH, and temperature [243], can help us understand the virus life cycle. As more therapeutic uses of viral capsids are developed, including vaccines and as drug and gene delivery vectors, more thorough characterization of the capsids is needed.

Hydrophobicity is one of the least understood and difficult to characterize physicochemical properties of any biomolecule. Hydrophobicity governs biomolecule adhesion through van der Waals forces arising from the mobility of water molecules at the molecular surface [15, 244]. For viruses in particular, hydrophobicity affects aggregation and disaggregation [18, 137] and adsorption to surfaces [130]. The hydrophobicity of ideal, apolar substances has been described thermodynamically as the length scale of water structure perturbation and the enthalpy of hydration using the Lum-Chandler-Weeks theory [245]. According to this theory, hydrophobicity is the rearrangement of water molecules and the breaking of hydrogen bonds between water molecules at the interface between a hydrophobic surface and a hydrophobic substance, resulting in a decrease in the hydration enthalpy [245]. The broken hydrogen bonds result in the formation of cavities in the water structure through the exclusion of water molecules from their occupied volume. The cavity represents an area where hydrogen

bonding cannot take place [246]. However, the hydrophobicity of viruses cannot be sufficiently characterized based on these theories due to the proximity of chemical heterogeneous (polar and apolar) groups on the virus surface. As a result, a method for hydrophobic characterization that can reflect the complex nature of virus surfaces is required.

A conventional way to characterize virus hydrophobicity is through the analysis of crystal structures. The solvent-accessible surface area (SASA) of different amino acids on the virus surface can be used to compare surface hydrophobicity [247]. MS2 [14], rotavirus [15], and many parvoviruses [16] have been characterized by a comparison of their SASA. However, without accounting for surface roughness, the evaluation of the solvent accessible surface area is often too elementary to be meaningful [244, 248]. Another approach is to determine the cavity free energy map that exists around a protein or virus. This context-dependent hydrophobicity prediction method observes water molecule cavities around proteins [244]. Hydrophobic molecule volumes are utilized as probes in this approach to map protein hydration shells. It is a context dependent method because the cavity utilized to assess protein hydrophobicity is reliant on the shape and size of the probe. Also, there is a possibility of dispersive interactions between the probe molecule and proteins that might not be accounted for in this method. These methods described may give some general comparison on biomolecule hydrophobicity, but the high surface complexity of viruses make them difficult to apply accurately. Therefore, an experimental method is still needed.

Experimental measurements of virus hydrophobicity often take advantage of the adsorption of viruses and proteins to hydrophobic surfaces. Hydrophobic interaction chromatography (HIC) characterizes hydrophobicity based on the buffer concentration required to elute the compound from the chromatography column [16, 18, 130, 147, 249]. This approach is merely qualitative. HIC can be problematic in characterizing hydrophobicity because not only does binding rely on hydrophobic interaction, but other interactions may occur between the resin and the biomolecule being measured. Also, solution conditions that promote hydrophobic interactions also promote aggregation. This

aggregation can also interfere with the measurement of hydrophobicity [250, 251]. These drawbacks make the HIC method less reliable and useful.

Dye adsorption for hydrophobicity characterization uses special dyes that bind specifically to hydrophobic patches on biomolecules or nanoparticles. This method allows the quantification of hydrophobicity for particles of varying sizes and surface area [176]. Using the adsorption of ANS (8-aniline-1-naphthalene sulfonic acid), which fluoresces when bound to hydrophobic patches on biomolecules, the hydrophobicity of porcine parvovirus (PPV) [16] and proteins [252] has been characterized. Hydrophobic Rose Bengal, which has a strong absorbance at 543 nm, adsorption to nanoparticles have been used to characterize hydrophobicity [176, 182]. Hydrophobicity is then characterized based on the adsorbed dye concentration which is obtained from the difference between initial and final dye concentration. This method has a major disadvantage of requiring high-purity product to prevent the adsorption of the dye by impurities.

The atomic force microscope (AFM) has emerged as a tool to characterize the surface properties of materials at the nanoscale [206, 253]. AFM can measure physicochemical properties in an aqueous environment and at room temperature, resulting in the characterization of biomolecules in near-physiological conditions [254]. AFM is an established method for measuring the size of single-cells and bacteriophages [255], characterization of changes in structure and adhesion properties of cells and viruses [231], and measuring the mechanical properties of biomolecules [256, 257]. The AFM tip can be modified and used to probe the interaction force between the modified tip and biomolecules [158, 200, 203], often referred to as chemical force microscopy (CFM) [258, 259]. CFM has been used to measure the isoelectric points of viruses, [158, 204] and proteins [203] and to characterize the interaction of potential drugs with their receptors to quantify effective dosage requirements [216, 260]. CFM has the disadvantages of requiring specialized training for the operation of the microscope, being time-consuming even for a seasoned user, and being impractical for in-line determination of virus hydrophobicity. However, CFM allows the quantification of virus hydrophobicity on a nanoscale level using small volumes of virus samples and measures

virus hydrophobicity at a single particle scale. Therefore, variations in the hydrophobicity of the particles in a virus pool can be traced.

We have used CFM to characterize the hydrophobicity of two viruses, PPV and BVDV. The CFM measurements were compared to dye adsorption tests using PPV and BVDV to investigate alternative metrics of hydrophobicity. CFM introduces a novel method for measuring virus hydrophobicity at the single particle level and investigates how hydrophobic adhesion to virus particles changes in a variety of solution conditions. This characterization could highlight new understanding of virus adhesion during the virus life cycle, as well as during therapeutic applications.

## 3.2 Materials and methods

### 3.2.1 Materials

Sodium phosphate dibasic heptahydrate (ACS grade, 98.0–102.0%), sodium phosphate monobasic monohydrate (ACS grade, 98.0–102.0%), poly (ethylene glycol) (PEG 8000, average MW: 8kDa), sodium chloride (ACS grade,  $\geq 99.0\%$ ), 12-mercaptododecanoic acid ( $\text{HS}(\text{CH}_2)_{11}\text{COOH}$ , 96%), 1-dodecanethiol ( $\text{HS}(\text{CH}_2)_{11}\text{CH}_3$ ,  $\geq 98\%$ ), 11-mercapto-1-undecanol ( $\text{HS}(\text{CH}_2)_{11}\text{OH}$ ,  $\geq 99\%$ ), sodium dodecyl sulfate (BioReagent,  $\geq 98.5\%$ ), and Rose Bengal (95%), were purchased from Sigma-Aldrich (St. Louis, MO). N-hydroxysulfosuccinimide (NHS) and 1-ethyl-3-(3-dimethyl aminopropyl) carbodiimide hydrochloride (EDC) were purchased from ThermoFisher Scientific (Waltham, MA). Eagle's minimum essential medium (EMEM), Dulbecco's modified eagle's medium (DMEM), fetal bovine serum (Mexico origin) (FBS), horse serum, 10,000 U/ml penicillin-streptomycin (pen-strep), 0.25% trypsin-EDTA (1X), phosphate buffered saline pH 7.2 (1X), sodium pyruvate and sodium bicarbonate (7.5%) for cell culture and virus propagation were purchased from Gibco™ (Grand Island, NY). Ethanol 200 proof was purchased from Decon Labs. Inc (King of Prussia, PA). 3M (Saint Paul, MN) Emphaze AEX Hybrid Purifiers were provided by 3M. Biotech cellulose ester 1000 kDa dialysis tubing (Rancho Dominguez, CA). BioRad Econo-Pac 10DG desalting

column (Hercules, CA). Thiazolyl blue tetrazolium bromide (MTT) (98%) was purchased from Alfa Aesar (Haverhill, MA). Hydrochloric acid (HCl, ACS grade, 36.5–38.0%) was purchased from Fisher Scientific (Pittsburgh, PA). CSG10/Au and CSG30 AFM probes were purchased from NT-MDT Spectrum Instruments (Moscow, Russia). All aqueous solutions or buffers were prepared using purified water with a resistivity of  $\geq 18 \text{ M}\Omega\cdot\text{cm}$  from a Nanopure filtration system (Thermo Scientific) and filtered using a  $0.2 \mu\text{m}$  disposable bottle top filter or a  $0.2 \mu\text{m}$  syringe filter (VWR) before use.

### **3.2.2 Propagation and titration of cells and virus**

Porcine kidney cells (PK-13, CRL-6489) were purchased from the American Type Culture Collection (ATCC) and were cultured using EMEM augmented with 10% v/v FBS and 1% v/v pen/strep. Porcine parvovirus (PPV) NADL-2 was gifted through the generosity of Dr. Ruben Carbonell at North Carolina State University. PPV was propagated on PK-13 cells, as previously described [261], and then stored at  $-80 \text{ }^\circ\text{C}$  until used. Bovine turbinate cells (BT-1, CRL-1390) and (BVDV) NADL strain were purchased from ATCC and USDA APHIS respectively. BT-1 were cultured in DMEM with 10% v/v horse serum and 1% v/v pen/strep. BVDV was propagated in BT-1 cells as described previously [158]. PPV and BVDV were semi-purified through dialysis using a 1000 kDa dialysis tubing at  $4 \text{ }^\circ\text{C}$  for 2 days with two PBS buffer exchanges. The virus was further purified with a desalting column. Both viruses were titrated using the MTT cell viability assay as previously described [158, 261]. Using the MTT assay, the virus stocks were approximately  $1 \times 10^8 \text{ MTT}_{50}/\text{ml}$  for PPV and  $1 \times 10^7 \text{ MTT}_{50}/\text{ml}$  for BVDV.

### **3.2.3 Virus and control surface preparation**

Pre-cleaned glass slides were coated with 5 nm chromium and 35 nm gold sequentially using a Perkin-Elmer Randex sputtering system (Model 2400, Waltham, MA). Gold-coated glass slides were cleaned with 100% ethanol, heated to  $65 \text{ }^\circ\text{C}$ , dried, and stored at room temperature in a dry container until time of use. Gold-coated glass slide surface modification using a self-assembled monolayer (SAM), and virus immobilization followed the same procedure as described in previous work [158].

Negative control surfaces were hydroxyl (-OH) terminated gold-coated glass slides which were prepared by immersing gold-coated glass slides in a 14 ml solution containing 2 mM HS(CH<sub>2</sub>)<sub>11</sub>OH in ethanol for 24 hours. Positive control surfaces were alkyl (-CH<sub>3</sub>) terminated gold-coated glass slides prepared by immersing gold-coated glass slides in a 14 ml solution containing 4 mM HS(CH<sub>2</sub>)<sub>11</sub>CH<sub>3</sub> in ethanol for 24 hrs.

### **3.2.4 Buffers**

Phosphate buffered saline (PBS) solution at pH 7.2 was prepared by mixing a solution of 1.06 mM sodium phosphate monobasic, 2.97 mM sodium phosphate dibasic, and 155 mM sodium chloride. PBS with additional salt concentrations were made using additional 195 mM or 845 mM sodium chloride. 4 – 10% ethanol or PEG 8000 was added to PBS. A solution of 1M NaOH or HCl was used to adjust the pH, and pH was measured with a calibrated Fisherbrand Accumet AE150 benchtop pH meter (Hampton, NH).

### **3.2.5 AFM probe functionalization**

Probes used for force measurements were the NT-MDT CSG10/Au AFM probes (spring constant - 0.1 – 0.5 N/m, tip radius – 10 nm). AFM probes were functionalized using a solution of 4 mM HS(CH<sub>2</sub>)<sub>11</sub>CH<sub>3</sub> in ethanol for 24 h, rinsed with ethanol, and air-dried in a chemical hood. Probes functionalized with alkyl group (HS(CH<sub>2</sub>)<sub>11</sub>CH<sub>3</sub>) were used within 96 hrs after functionalization and were tested using the control glass slides to ensure proper functionalization before use.

### **3.2.6 AFM imaging, force measurement, and analysis**

All hydrophobicity force measurements were carried out using a Bruker Dimension ICON atomic force microscope with ScanAsyst (Santa Barbara, CA). Virus surfaces after immobilization and control surfaces were imaged using a NT-MDT CSG30 AFM probe in tapping mode with PBS solution. Using peak force quantitative nanoscale mechanical mode (Peakforce QNM), hydrophobicity measurements were carried out using NT-MDT CSG10/Au AFM probes functionalized with a methyl group. The spring

constant of functionalized probes were obtained using the thermal tuning function on the AFM prior to use. Different solutions were used for the force measurements. All experiments were performed at room temperature. Between 100 - 150 force distance (F-D) curves were obtained for each probe/sample combination. Virus and control force measurements were conducted in triplicates resulting in an average of 300 F-D for each sample set. Data analysis was performed with Bruker Nanoscope Analysis software.

### 3.2.7 Dye adsorption

Rose Bengal was prepared in nanopure water. Viruses were purified using a 3M Emphaze anion exchange filter attached to a Cytiva (formerly, GE) AKTA Pure FPLC (Malborough, MA) [262, 263], and dialyzed into the testing buffer. At each dye concentration, equal volumes of dye and virus were combined into a microcentrifuge tube, placed on a rotational shaker, and allowed to mix for 120 minutes. Afterwards, the viruses were separated from unabsorbed dye by centrifugation (ThermoScientific Sorvall ST16R, Waltham, MA) for 35 mins at 15,200 rpm. To estimate the dye concentration, the supernatant containing unabsorbed dye in the tube was placed into 96-well plates and light absorbance was measured using a BioTek (now Agilent) Synergy HTX Multimode reader UV-Vis spectrophotometer (Santa Clara, CA) at a wavelength of 543 nm. The wavelength was selected based on the manufacturer's recommendations and confirmed by experiments testing a range of wavelengths (543 – 600nm) to ascertain the wavelength of maximum absorbance (See **Table A.1.1**). Blank tests were also carried out, with dye solutions containing buffers and water but no virus and was monitored for 180 minutes. This was done to guarantee that no dye was adsorbed onto the microcentrifuge tubes over time, which would interfere with spectrophotometer measurements of dye concentrations (See **Figure A.1.1**). All absorbance measurements tests were done in triplicate, and the mean values were utilized to analyze the results. The amount of dye that was absorbed to the virus particles,  $q_e$ , is calculated using **Equation 3.2.1**.

$$q_e = (C_o - C_e) \frac{V}{M} \quad 3.2.1$$

Where,  $C_o$  (mg/L) is the initial dye concentration,  $C_e$  (mg/L) is the concentration of dye in the supernatant after centrifugation,  $V$  is the volume of mixture (ml) and  $M$  is the concentration of virus (MTT<sub>50</sub>/ml). The dye adsorption was fit to the Langmuir **Equation 3.2.2** and Freundlich **Equation 3.2.3** isotherm models. These models were linearized and fit by minimizing the sum of squared errors using Microsoft Excel to obtain values for the adsorption constants in the models.

$$q_e = \frac{q_{\max} K_L C_e}{(1 + K_L C_e)} \quad \mathbf{3.2.2}$$

$$q_e = k_f C_e^{1/n} \quad \mathbf{3.2.3}$$

Where,  $q_e$  (mg/MTT<sub>50</sub>) is the amount of dye adsorbed per virus concentration and  $C_e$  (mg/L) is the equilibrium concentration of dye after adsorption.  $K_L$  (L/mg) and  $q_m$  (mg/MTT<sub>50</sub>) are the Langmuir constant and maximum adsorption capacity for monolayer adsorption respectively.  $k_f$  (L/MTT<sub>50</sub>), and  $1/n$  are the Freundlich constants for adsorption capacity and interaction respectively.  $1/n$  indicates the strength of adsorption and surface heterogeneity of the virus. When  $1/n < 1$ , adsorption is reversible, but when  $1/n > 1$ , the adsorption is irreversible [193].

### 3.3 Results

Hydrophobicity controls in a large part both capsid protein folding and capsid assembly, which is integral to capsid integrity and the interaction of virus particles with cells. Even though hydrophobicity is an extremely important property, the measurement of hydrophobicity is difficult. Here, virus hydrophobicity is measured by chemical force microscopy (CFM) utilizing an atomic force microscope (AFM) to probe the adhesion force between a functionalized probe and a virus, as shown in **Figure 3.1**. A similar method using charged functionalized AFM probes has been used to determine the isoelectric point of three viruses [158, 204]. By changing the probe functionalization, we are now applying CFM to measure virus hydrophobicity.

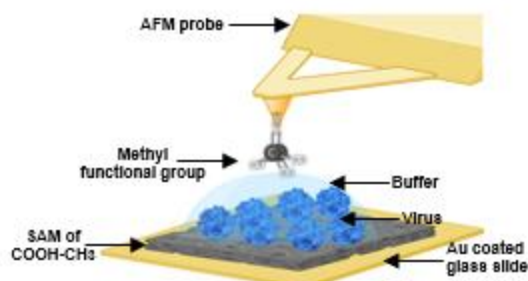


**Figure 3.1 CH<sub>3</sub> functionalized AFM probe in contact with viruses.** A gold coated glass slide is functionalized with a self-assembled monolayer of thiol compounds that are 50/50 COOH and CH<sub>3</sub>. The viruses are covalently bound to the COOH groups with NHS/EDC chemistry. The functionalized AFM probe measures the forces between the functionalized tip and viruses on the surface in different liquid environments. (Created with Biorender.com).

Non-enveloped porcine parvovirus (PPV) and enveloped bovine viral diarrhea virus (BVDV) are the model systems used to measure virus hydrophobicity. PPV has a diameter of 18-26 nm and an isoelectric point of 4.8-5.1 [158, 264]. The principal structural protein of PPV is VP2, which accounts for about 80% of the total capsid protein content [265]. PPV is a primary causative agent of porcine reproductive failure [266]. BVDV is an enveloped virus containing a nucleocapsid surrounded by an outer envelope lipid bilayer. The lipid bilayer contains glycoproteins that mediate pathogenesis and virus adhesion [267]. BVDV has a diameter of 40-60 nm and an isoelectric point of 4.3-4.5 [158]. BVDV has three major structural proteins: a transmembrane protein (M), a core nucleocapsid protein (C), and a surface protein (E) [268]. The surface protein E2 makes up about 70% of the envelope protein [269]. BVDV is a major causative agent of reproductive failures in cattle [270].

### 3.3.1 Virus hydrophobicity by CFM

Initial virus hydrophobicity experiments measured the adhesion of PPV and BVDV to a hydrophobic CH<sub>3</sub>-terminated AFM probe in PBS at pH 7.2. Imaging and height analysis of the virus particles and SAM confirmed proper immobilization of the virus to the surface (see **Figure A.1.2**). Probe functionalization was confirmed by measuring the adhesion of the CH<sub>3</sub>-terminated AFM probe to a CH<sub>3</sub>-modified gold

coated slide as positive control and an OH-modified gold coated glass slide as a negative control. Control data is shown in **Figure A.1.3** Once probe functionalization was confirmed, adhesion to PPV and BVDV in PBS was measured and the data are shown in **Figure 3.2**. Since the PPV measurements showed low hydrophobic interaction, NaCl was added to the solution to increase hydrophobic interactions [271, 272]. The adhesion of PPV to the CH<sub>3</sub>-tip was low for all salt concentrations tested, as shown in **Figure 3.2**. The hydrophobicity of BVDV was an order of magnitude higher than PPV and increased with increasing salt concentration. Frequency histograms (see **Figure A.1.4**) and force summaries for the triplicate samples measured for PPV and BVDV in all salt concentrations can be found in **Figure A.1.5** respectively. This preliminary data demonstrates that BVDV is much more hydrophobic than PPV.

Virus hydrophobicity was further explored using additives to enhance hydrophobic interaction. PEG was added because it has been shown to enhance hydrophobic interactions between proteins and a hydrophobic media [273, 274]. The increased hydrophobic interaction is likely due to preferential exclusion of PEG from the proteins. The large hydrodynamic radius of PEG molecules and strong interaction of PEG with water molecules leads to a deficit of PEG and water molecules around the virus [275-277]. PEG concentrations were limited to a maximum of 10% because the soft AFM probe could not be used in viscous solutions. Ethanol was also used as an additive to increase hydrophobicity because it is an organic polar solvent that can displace the water molecules in the virus solvation shell [278]. The water displacement results in the exposure of hydrophobic patches on the virus surface, leading to an increase in hydrophobic interaction. The increased hydrophobic interaction of DNA and protein is demonstrated by their precipitation in ethanol solutions. Due to the unfavorable thermodynamic interactions caused by ethanol, the hydrophobic patches are forced to cluster together to form precipitates [279, 280]. None of the cosolvents at the concentrations tested inactivated the viruses (see **Figure A.1.6**).

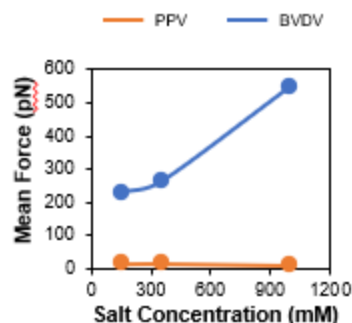


**Figure 3.2 Salt concentration effect on PPV and BVDV adhesion.**

The addition of PEG resulted in an increase in hydrophobic adhesion force for PPV and BVDV, as shown in **Figure 3.3**. It is likely that the preferential exclusion of PEG from protein surfaces also applies to the viruses tested. However, with the addition of ethanol, an increase in adhesion force was only observed for PPV, while a decrease in adhesion force was observed for BVDV. This difference in adhesion of PPV and BVDV might be due to the hydrophilic head groups in the BVDV lipid bilayer establishing hydrogen bonds with ethanol [281, 282]. As a result, the hydrophobic contact between BVDV and the CH<sub>3</sub>-tip is reduced, resulting in a decrease in measured adhesion force.

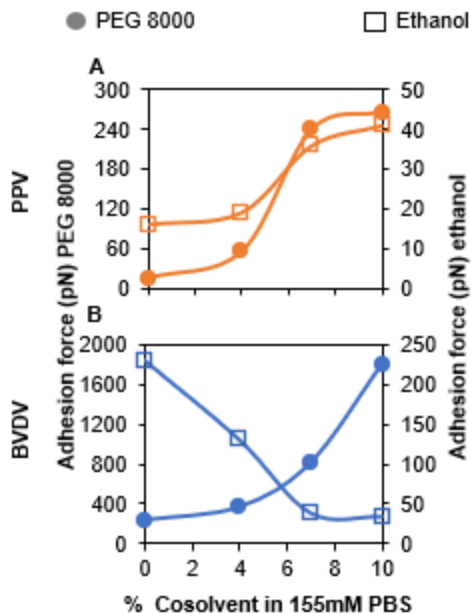


**Figure 3.3 Cosolvents change hydrophobic interactions.** The addition of PEG 8000 and ethanol to PBS altered the CFM adhesion force. (A) PPV and (B) BVDV with the addition of polyethylene glycol (PEG) 8000 and ethanol. Each data point is the mean of at least 150 measurements with three different combinations of probes and virus surfaces.

### 3.3.2 Virus hydrophobicity by dye adsorption isotherms

Dye adsorption is commonly used to measure the hydrophobicity of nanoparticles [176]. We chose to use the dye Rose Bengal because it has been used previously to characterize the hydrophobicity of nanoparticles. Rose Bengal can bind the virus via its hydrophobic tail [176]. To test if dye adsorption could measure the hydrophobicity of viral particles, we added various dye concentrations to a constant virus concentration. The adsorption isotherms are shown in **Figure 3.4**. The goal was to compare the dye adsorption technique, which is a more established method of measuring hydrophobicity, to the CFM results.

Rose Bengal was a good fit for the isotherm models. In comparing the correlation coefficient ( $R^2$ ) obtained for the Langmuir and Freundlich model fits shown in **Table 3.1**, the Freundlich isotherm has the best fit for Rose Bengal adsorption to PPV and BVDV. The Langmuir equation is an unsuitable model for hydrophobic viral adsorption because it is unable to account for multivalent interactions [283] and enhanced hydrophobic

interaction of the virus due to increased salt concentration [149, 284, 285]. The Freundlich isotherm has become relevant in most biologic applications because it describes the reversibility and deviation from ideality of biologic adsorption processes [286], and assumes heterogeneity of the adsorption sites [195], which are valid assumptions for viral particles. The Freundlich model is only valid at low concentrations, which is also well suited to viral formulations.

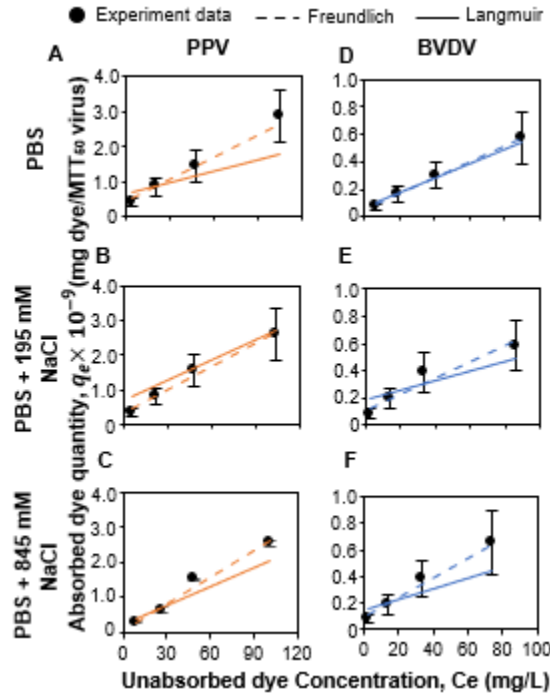


**Figure 3.4 Adsorption isotherms for PPV and BVDV.** Fixed concentrations of PPV and BVDV were combined with various concentrations of Rose Bengal in different concentrations of salt. The isotherms were fitted using the Langmuir, and Freundlich models (A) PPV in 1X PBS (B) PPV in 1X PBS + 195mM NaCl (C) PPV in 1X PBS + 845mM NaCl (D) BVDV in 1X PBS (E) BVDV in 1X PBS + 195mM NaCl (F) BVDV in 1X PBS + 845mM NaCl. Each data point is in triplicate, and the error bars represent the standard deviation.

The  $K_f$  values in **Table 3.1** can be used to evaluate the adsorption of Rose Bengal. The larger the  $K_f$  value, the smaller the amount of Rose Bengal dye adsorbed (less hydrophobic interaction) to the virus. For PPV, with increasing salt concentration, the  $K_f$  value decreases, indicating increased hydrophobic interaction of PPV with Rose Bengal dye. For BVDV, as salt concentration increased, the  $K_f$  value increases, indicating

decreased hydrophobic interaction between BVDV and Rose Bengal dye. This may indicate that the hydrophobicity measured by Rose Bengal adsorption and ethanol addition with the CFM may be similar. For PPV and BVDV, the  $1/n$  values are less than 1, as shown in **Table 3.1**, indicating reversibility of the adsorption.

**Table 3.1** Summary of isotherm parameters for adsorption of Rose Bengal to PPV and BVDV

	PPV			BVDV		
	PBS	PBS + 195 mM NaCl	PBS + 845 mM NaCl	PBS	PBS + 195 mM NaCl	PBS + 845 mM NaCl
<b>Langmuir</b>						
$q_{\max, RB}$ (mg/MTT <sub>50</sub> )	2.00E-09	3.33E-09	5.00E-09	1.00E-08	5.00E-09	5.00E-09
$K_{l, RB}$ (L/mg)	5.00E-02	3.00E-02	6.67E-03	1.25E-02	1.00E-01	6.67E-02
$R^2$	0.92	0.87	0.98	0.99	0.99	0.95
<b>Freundlich</b>						
$1/n_{, RB}$	6.46E-01	7.06E-01	9.32E-01	7.79E-01	5.58E-01	6.28E-01
$K_{f, RB}$ (L/MTT <sub>50</sub> )	1.28E-10	9.86E-11	3.52E-11	1.70E-10	4.99E-10	4.16E-07
$R^2$	0.99	0.99	0.98	0.99	0.99	0.99

### 3.4 Discussion

Viruses have chemically heterogenous surfaces comprising both hydrophobic and hydrophilic patches, making them difficult to characterize. There is a need to develop a standard characterization technique for measuring virus and protein hydrophobicity. Understanding virus hydrophobicity could shed light on the mechanism of viral interactions in manufacturing and biology.

We have demonstrated that the hydrophobicity of viruses can be characterized and quantified using CFM. It is likely that we are measuring direct hydrophobic interaction and not other non-specific or less defined interactions. When a hydrophobic tip enters the buffer solution, hydrogen bonds between water molecules of the buffer solution are broken to accommodate the hydrophobic tip. There is a cavity around the tip and a cavity around the hydrophobic virus that likely allow direct van der Waals interactions to take place and be measured [149, 248, 287].

Virus hydrophobic interactions should be affected by ionic strength. However, results in **Figure 3.2** showed low adhesion of the hydrophobic probe to PPV. Studies

have shown that the VP2 protein, which accounts for about 80% of PPV surface protein, is mostly hydrophilic [265]. With this large area of hydrophilic amino acids, it is likely that the salt concentrations used were not able to suppress the virus-solvent interactions for PPV. For BVDV, the crystal structure of E2 protein, which is about 70% of the envelope protein, is hydrophobic [269].

Cosolvents can induce changes in water structure that alter the interplay between the virus hydration layer and other surfaces. Cosolvents can be grouped as kosmotropes or chaotropes. The kosmotropic cosolvent PEG is more polar than water; thus, water forms a very strong network around the PEG [288]. PEG molecules interact with the water molecules in the buffer solution and hydration shell of the virus through hydrogen bonding, resulting in preferential exclusion of PEG from the virus hydration shell. This results in a decrease in virus-water interactions, in turn exposing the hydrophobic patches of the virus to the CH<sub>3</sub>-tip during CFM measurements. As predicted, raising the PEG concentration increased the measured hydrophobic interaction, as shown in **Figure 3.3**. At 7 w/w% PEG, PPV becomes saturated and no more increase in hydrophobic interaction occurs. The saturation point for BVDV was not reached at 10 w/w% PEG, and the hydrophobic interaction continued to increase. Although our previous work studying the effect of PEG MW on the partitioning behavior of viruses in an aqueous two-phase system (ATPS) does not support the preferential exclusion theory [289], the partitioning of virus to the PEG phase in the previous study can be attributed to the electrostatic potential difference between the PEG and citrate phase and not solely hydrophobic interactions. However, PEG exclusion does describe the hydrophobic interactions measured with CFM.

Ethanol is less polar than water and a chaotropic cosolvent that reduces the degree of hydrogen bonding between water molecules [290]. PPV showed an increase in adhesion as the concentration of ethanol increased, as shown in **Figure 3.3**. Ethanol causes a disruption of the hydrogen bonds in the bulk water and hydration shell of the virus, making ethanol preferentially bind to the virus. This preferential binding can result in repulsion between the hydrophilic portions of the virus proteins, thereby reducing their inter-helical interactions and exposing the hydrophobic regions [291]. Studies have

shown protein aggregates because of conformational changes induced by addition of ethanol to solutions containing salt. Addition of ethanol to PBS reduces the dielectric constant of the solution, which changes the fraction of protein negative charge neutralized by the counterions of the salt ions [292, 293]. Although the adhesion force for PPV increased with the addition of ethanol, the binding of PPV to the hydrophobic probe was still very low. Measurements for BVDV showed that the addition of ethanol brought about a decrease in measured adhesion force as shown in **Figure 3.3**. This means that addition of ethanol resulted to an increase in BVDV solubility, since ethanol can form hydrogen bonds with the hydrophilic head group of lipids [281, 282]. This interaction will result in an increase in the amount of ethanol present in the virus hydration shell and decreasing the surface area of exposed hydrophobic patches.

From the dye adsorption experiments, Rose Bengal adsorption on PPV and BVDV revealed that PPV was more hydrophobic than BVDV, see **Figure 3.4** and the  $K_f$  values in **Table 3.1**. The  $K_f$  value, which represents adsorption capacity, establishes a link between the amount of virus adsorbed and the dye volume. When the  $K_f$  value is low, more virus particles have adsorbed the dye, suggesting a strong hydrophobic interaction. This difference in PPV and BVDV binding to Rose Bengal dye might be due to greater binding sites for Rose Bengal dye on the protein capsids of PPV compared to the lipid bilayer with encapsulated proteins of BVDV.

When the results from both methods are compared, the practical advantage of using CFM over dye adsorption for virus hydrophobicity is demonstrated. Non-hydrophobic interactions can be screened out using the CFM. Furthermore, with CFM, the surface scan prior to force measurements allows for the removal of particles smaller or larger than virus particles. Only the viruses are measured as a result of this screening. This is not true for dye adsorption. The dye adsorption method is incapable of distinguishing between virus particles and impurities that may have the same hydrophobicity as the virus but differ in size. As a result, the dye adsorption measured cannot be defined solely as the virus hydrophobicity. Furthermore, because the dye has charge properties, secondary contributions to adhesion based on electrostatic interactions cannot be eliminated. However, because the CFM probe is purely hydrophobic,

contributions from charge is likely not a contributor to cannot be used to probe-virus adhesion.

### **3.5 Conclusions and future work**

Virus hydrophobicity is a major determinant in predicting the fate and transport of virus in biologic systems. We demonstrated that the hydrophobicity of a non-enveloped and an enveloped virus can be measured in a near physiologic state by measuring adhesion force using CFM. We found that hydrophobic interactions of viruses can be impacted by the composition of the buffers, a fact often overlooked when using conventional hydrophobicity quantification techniques. With the CFM method, increasing the salt concentration did not increase the hydrophobic interaction of the non-enveloped PPV but enhanced the hydrophobic interaction of enveloped BVDV. The addition of PEG caused increased hydrophobic interaction for PPV and BVDV, likely due to the preferential exclusion of PEG on the virus surface and its strong water binding. With ethanol addition, which likely binds to the virus, the results were mixed. PPV, which is made of protein, increased in hydrophobicity after ethanol binding, while BVDV, which is made of a lipid bilayer and spike proteins, decreased in hydrophobicity. It is likely that ethanol binding to protein exposes hydrophobic patches whereas binding to lipid headgroups decreases hydrophobic interaction.

The CFM results were compared to a more conventional measurement of hydrophobicity: dye adsorption. The dye adsorption correlated with the CFM results in ethanol, but not in pure salt or PEG. The CFM method for measuring hydrophobicity can characterize the virus hydrophobicity using minimal volumes of virus and buffers. The ability to work in an aqueous environment to predict viral hydrophobicity makes CFM suitable for virus characterization in physiological conditions. Experimental, single-particle measurements of hydrophobicity of virus particles in varying solution conditions will greatly expand our understanding of virus surface adhesion.

For future work, the effect of other additives like surfactants and osmolytes on virus hydrophobicity should be explored. This will allow results from CFM

measurements to be compared to existing theories on the effect of these hydrophobic interaction modifiers.

## 4 Understanding the Separation of Empty and Full AAV Capsids on Ion Exchange Chromatography by Chemical Force Microscopy

### 4.1 Introduction

Adeno-associated virus (AAV) has been identified as a powerful gene delivery vector to treat a variety of single gene disorders. The success of AAV as a gene delivery vehicle has been demonstrated by several pre-clinical and clinical studies. The European Medicines Agency (EMA) approval of Glybera (for lipoprotein lipase deficiency), and the Food and Drug Administration (FDA) approval of Luxturna (for retinal dystrophy), and Zolgensma (for spinal muscular atrophy), as well as the large number of clinical trials involving AAV, demonstrate the potential of AAV as a gene delivery vector [134, 294-296]. There are over 136 ongoing clinical trials utilizing AAV for gene therapy around the world as of 2021 [38, 297, 298].

AAV is a non-pathogenic, non-enveloped, icosahedral virus in the *Parvoviridae* family [299]. AAV has a diameter of 18-26nm, with a protein capsid comprising three virus protein subunits (VP1, VP2, and VP3) that surround and protect a linear, single-stranded DNA genome of 4.7kb in length [105, 300]. AAVs are produced recombinantly by a triple plasmid infection, where replication and capsids proteins are on one plasmid, the therapeutic gene of interest in on another plasmid, and further replication proteins from another viral vector are on the third [70]. Replication and capsid proteins are produced and the assembled capsid is trafficked to the nucleus [301]. Here, the DNA containing the gene of interest is packaged into the capsid by the Rep53/40 proteins' helicase/ATPase domain [302]. Since DNA packaging is regarded as a rate-limiting step [301], so many empty capsids remain unfilled or are filled with fragmented DNA (partially full capsids) [303]. The empty capsids can be greater than the full or partially full capsids by about 25-fold [113, 300]. Due to the absence of the DNA in these empty virus particles, they are not intrinsically functional for gene therapy.

The empty particles are a process-related impurity and may cause negative clinical outcomes. The empty capsids limit the efficacy of the gene therapy drug product resulting in high dosing requirements to trigger the required therapeutic effect [86]. High capsid dosing may cause anti-capsid T-cell responses [304]. Cell-mediated immunity that targets the AAV protein capsid can lead to the removal of transduced tissues that have already been infected with therapeutic AAV [305]. This cytotoxic effect has been associated with the presence of empty viral particles, which leads to a loss of the gene of interest and a decrease in the expression of the target therapeutic protein [306]. As a result, lowering the ratio of empty to full viral particles is likely beneficial in order to lower immunogenicity and competition for receptor binding sites, which limits transduction efficiency [67, 77, 169, 307].

A key step in the downstream purification of AAV vectors is the removal of empty capsids. This ensures the high potency of the gene therapy product and meets the quality and safety recommendations set by regulatory agencies [300, 306, 308]. There are two major techniques employed for separating the empty AAV capsids from the full capsids: separation by density and by charge. The empty capsids are less dense than the full capsids due to the absence of DNA. Based on the density differences, empty AAV capsids may be separated from full capsids by gradient ultracentrifugation using cesium chloride (CsCl) or iodixanol [309, 310]. Gradient ultracentrifugation method offers the advantage of being applicable to several AAV serotypes and efficiently separates the empty capsids from the full capsids. However, ultracentrifugation is not scalable, making it difficult to make the large quantities needed in manufacturing.

Chromatographic methods based on surface charge differences are a manufacturing scale alternative to separate empty and full capsids. Isoelectric point (pI) measurements of various AAV serotypes have indicated that the full capsids have a slightly lower pI than empty capsids [304]. Ion exchange chromatography (IEX), cation [89] and, more typically, anion exchange chromatography [311, 312] have demonstrated an ability to separate empty from full AAV capsids. The pH and conductivity of buffers control IEX separation of empty and full AAV capsids. Extreme pH can lead to damage of the viral particles, which compromises the capsid stability [313, 314]. While IEX can

be considered serotype-independent, its effectiveness can be restricted by the buffer conditions, AAV capsids solubility and overall surface charge distribution [307]. With IEX, it is not uncommon to have an overlap in the peaks between the empty and full capsids peaks, which can lead to a loss of full capsids [315]. However, IEX continues to be a popular approach for separation of empty and full AAV capsids because of its widespread use and familiarity in downstream manufacturing, established infrastructure, reproducibility, and ease of scalability [113]. Although, chromatography is the most preferred method for separating empty and full AAV capsids, it requires resins and buffer conditions that are uniquely developed and tailored for each serotype which is quite a challenging exercise [307].

The process of optimizing chromatographic separation for empty and full AAV separation is tedious, time consuming and requires large volume of buffers and virus. A unique approach to study the interaction of virus with chromatography ligands is by using chemical force microscopy (CFM). CFM uses a functionalized atomic force microscopy (AFM) tip to measure the force interactions of the chemistry on the functionalized tip and a surface. CFM has been used to measure the charge of proteins in different buffer conditions [203] and has more recently been applied to measure the charge of viruses [204, 316]. CFM uses very little sample, which is often in short supply during chromatography development, and can mimic the ligand and buffer environment inside of a chromatography column. Understanding interaction forces of ligands and analytics should give us improved insight into the chromatography process.

For this study, we functionalized an AFM probe with a quaternary amine to simulate a strong AEX ligand. The buffers used had similar composition to those utilized for chromatography. CFM provided insight into some of the interactions taking place in the AEX column beyond electrostatic interactions. Measured differences between empty and full AAV capsids give us new understanding of the magnitude of differences between empty and full capsids when adhering to positively charged or hydrophobic surfaces. This knowledge can be exploited to optimize the buffer conditions for empty and full capsid AAV separation using less virus and buffer volumes.

## 4.2 Materials and Methods

### 4.2.1 Materials

Sodium phosphate dibasic heptahydrate (ACS grade, 98.0–102.0%), sodium phosphate monobasic monohydrate (ACS grade, 98.0–102.0%), sodium chloride (ACS grade,  $\geq 99.0\%$ ), sodium citrate tribasic dihydrate (ACS reagent,  $\geq 99\%$ ), L-Histidine (BioUltra,  $\geq 99.5\%$ ), 11-mercaptoundecyl-N, N, N-trimethylammonium bromide ( $\text{HS}(\text{CH}_2)_{11}\text{N}(\text{CH}_3)_3\text{Br}$ ), Trizma base ( $\text{NH}_2\text{C}(\text{CH}_2\text{OH})_3$ ,  $\geq 99.8\%$ ), 12-mercaptododecanoic acid ( $\text{HS}(\text{CH}_2)_{11}\text{COOH}$ , 96%), 1-dodecanethiol ( $\text{HS}(\text{CH}_2)_{11}\text{CH}_3$ ,  $\geq 98\%$ ), 11-Mercapto-1-undecanol ( $\text{HS}(\text{CH}_2)_{11}\text{OH}$ ,  $\geq 99\%$ ), were purchased from Sigma-Aldrich (St. Louis, MO). Magnesium chloride hexahydrate (ACS reagent,  $\geq 99\%$ ), sodium acetate, anhydrous (ACS reagent,  $\geq 99\%$ ), poloxamer 188, N-hydroxysulfosuccinimide (NHS) and 1-ethyl-3-(3-dimethylaminopropyl) carbodiimide hydrochloride (EDC), and plain microscope slides (25 x 75 x 1mm) were purchased from ThermoFisher Scientific (Waltham, MA). CSG10/Au and CSG30 probes were purchased from NT-MDT Spectrum Instruments (Moscow, Russia). Ethanol 200 proof was purchased from Decon Labs. Inc (King of Prussia, PA). All aqueous solutions or buffers were prepared using purified water with a resistivity of  $\geq 18 \text{ M}\Omega \cdot \text{cm}$  from a nanopore filtration system (Thermo Scientific) and filtered using a 0.2 $\mu\text{m}$  disposable bottle top filter before use.

### 4.2.2 Methods

#### 4.2.2.1 AAV production

Triple co-transfection of the pHHelper, pAAV ITR-expression vector, and pAAV Rep-Cap plasmid DNA into HEK cells resulted in the production of AAV3B.

#### 4.2.2.2 Virus samples and control surface preparation

Using a Perkin-Elmer Randex sputtering system (Model 2400, Waltham, MA), cleaned glass slides were coated with 5 nm chromium followed by a gold layer of 35 nm. The gold-coated glass slides were washed with 100% ethanol heated to 65°C, dried, and

kept in a clean petri-dish until use. The virus particles were immobilized using the same methodology as in our earlier study of virus isoelectric points [158].

Control surfaces were utilized to check probe functionalization. For hydrophobic measurements, hydroxyl (OH<sup>-</sup>) terminated gold-coated glass slides were prepared by immersing gold-coated glass slides in 14 ml of 2 mM HS(CH<sub>2</sub>)<sub>11</sub>OH or 4 mM HS(CH<sub>2</sub>)<sub>11</sub>CH<sub>3</sub> in ethanol for 24hrs. For the charge measurements, quaternary amine (N(CH<sub>3</sub>)<sub>3</sub>) terminated gold-coated glass slides were prepared by immersing gold-coated glass slides in 14 ml of 4mM HS(CH<sub>2</sub>)<sub>11</sub>N(CH<sub>3</sub>)<sub>3</sub>Br in ethanol for 48hrs or carboxyl (COOH<sup>-</sup>) in 14 ml of 4 mM HS (CH<sub>2</sub>)<sub>11</sub>COOH in ethanol for 24hrs.

#### *4.2.2.3 Preparation of buffers*

Sodium acetate solution was prepared by making a 135 mM and 185 mM solution and magnesium chloride solution was prepared by making a 5 mM solution. Tris-HCl solution was prepared by making a 100 mM solution with Trizma base. A solution of 1M NaOH or HCl was used to adjust the acidic or basic level, and pH was measured with a calibrated Fisherbrand Accumet AE150 benchtop pH meter (Hampton, NH).

#### *4.2.2.4 AFM probe functionalization*

The force probes employed for force measurements were the NT-MDT CSG10/Au AFM probes (spring constant - 0.1 – 0.5 N/m, tip radius – 10nm). For hydrophobic functionalization, the AFM probes were placed in a clean petri-dish containing 14 ml ethanol solution with 4 mM HS(CH<sub>2</sub>)<sub>11</sub>CH<sub>3</sub> for 24hrs. For charge functionalization, the AFM probes were placed in a clean petri-dish containing 14ml ethanol solution with 4 mM HS(CH<sub>2</sub>)<sub>11</sub>N(CH<sub>3</sub>)<sub>3</sub>Br for 48hrs. Following immersion, the probes were washed with 25ml ethanol, dried in a chemical hood, and carefully stored in a clean AFM probe box. The functionalized probes lasted 96 hours and were checked using the control gold-coated glass slides to guarantee functionalization before usage.

#### 4.2.2.5 Force measurements and analysis

Using a Bruker Dimension ICON atomic force microscope equipped with the ScanAsyst system in peak force quantitative nanoscale mechanical mode (Peakforce QNM) and the corresponding functionalized NT-MDT CSG10/Au AFM probes, hydrophobicity and charge force measurements were obtained. The AFM's thermal tuning feature was used to determine the spring constant of the functionalized probes. Functionalized probes were utilized to scan the viral surface in PBS at pH 7.2 or the test solution for hydrophobic measurements while 20mM PB at pH 7 or the exact test solution was used for the charge measurements. We averaged 150 F-D curves from triplicates for each condition, with 50 to 150 curves acquired for each probe/sample combination. All the tests were done at the room temperature and the humidity closely monitored. The same approach was used for the control measurements. The curve analysis function of the Bruker Nanoscope Analysis Software was used to process the data.

### 4.3 Results and Discussion

Initial chromatography runs were conducted to create an enriched pool of empty AAV capsids and an enriched pool of full capsids. The anion exchange chromatogram (AEX) had two unique peaks, as shown in **Figure 4.1**. The wash peak contained the empty AAV3B capsids while the elution peak contained the full AAV3B capsids, as determined by the  $A_{260}/A_{280}$  absorbance ratio [317, 318] and shown in **Table 4.1**. Fractions from the flow-through and wash were combined to make the enriched empty pool of AAV3B capsids and the second peak was kept as the full pool. The  $A_{260}/A_{280}$  absorbance ratio of the initial virus pool for the empty and full capsids closely aligned with the expected absorbance ratios of 0.6 and 1.3 for empty and full AAV capsids, respectively [317, 318].

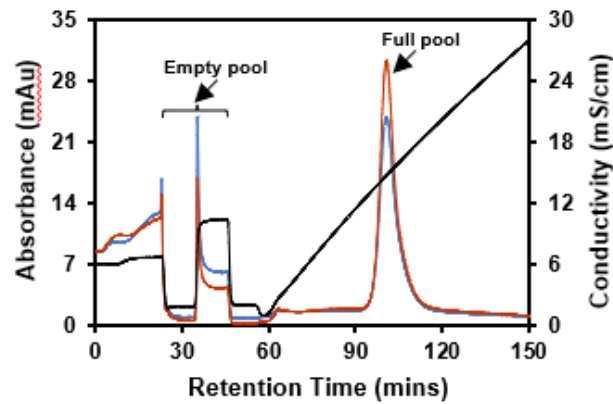


**Figure 4.1: Chromatogram for AAV initial pool loaded at high conductivity.** The empty capsids were collected in the wash step while the full capsids were collected in the peak for full capsids. Red and blue traces correspond to  $A_{260}$  and  $A_{280}$  respectively. Black trace corresponds to conductivity.

After the enrichment of each virus pool, the pools were dialyzed against a low-conductivity buffer to allow for further AEX analysis. The empty and full AAV3B capsid pools were each loaded at 2.3 mS/cm onto separate AEX columns, as shown in **Figure 4.2**. The titers and  $A_{260}/A_{280}$  of each peak are summarized in **Table 4.1**. The first peak had a  $A_{260}/A_{280}$  that would be expected for an empty peak, but the second likely had some full capsids in the peak, with a  $A_{260}/A_{280}$  ratio of 1.08 (see **Table 4.1**). Only one peak at a  $A_{260}/A_{280}$  ratio of 1.29 was found in the full capsids (**Table 4.1**). We concluded that the full capsid pool was fairly pure and that there were some full capsids in the empty pool.

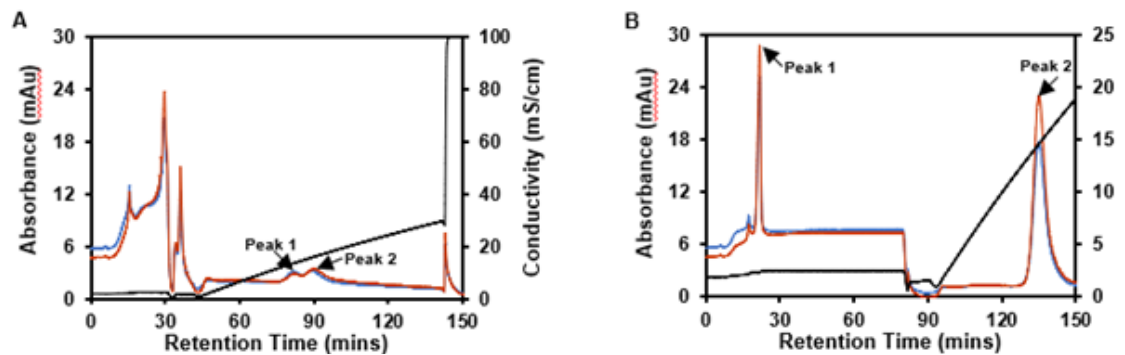


**Figure 4.2: Chromatograms showing peaks of AAV loaded on an AEX column using low conductivity buffer at pH 8.8** (A) Empty capsids (B) Full capsids. Red and blue traces correspond to  $A_{260}$  and  $A_{280}$  respectively. Black trace corresponds to conductivity.

**Table 4.1.** Summary of physical titer, absorbance, and conductivity for each peak from chromatograms.

	Initial virus pool	Empty capsids load	Full capsids load
Load Concentration (vp/ml)	2.55E+13	3.77E+11	1.31E+12
Absorbance, $A_{260}/A_{280}$	Empty peak -0.64 Full peak -1.27	Peak 1 - 0.91 Peak 2 - 1.08	Peak 1 - 1.19 Peak 2 - 1.29
Load Conductivity (mS/cm)	6	2.3	2.3
Elution Conductivity (mS/cm)	Empty peak – 10.3 Full peak – 14.8	Peak 1 – 13.5 Peak 2 – 16.0	Peak 1 – 2.37 Peak 2 – 14.7

To better understand the differences between empty and full AAV capsids and how they adhere to AEX columns, we used chemical force microscopy (CFM). CFM allowed the study of adhesion by positive charge and hydrophobicity to be separated. Virus particles were covalently immobilized onto a surface and the adhesion force for different AFM tip chemistries as measured, as shown in **Figure 4.3**. It is important that the virus be covalently attached to the surface so that the bond breaking that is measured is between the AFM tip and the virus, and not the virus and the gold surface. Using different chromatography buffer conditions, the adhesion and elution of AAV3B on AEX was measured to better understand the nature of the adhesion.

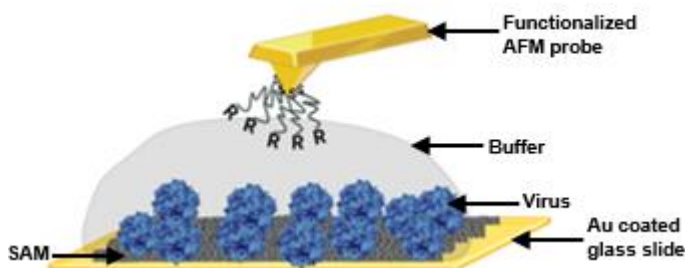


**Figure 4.3: Measurement for viruses using CFM.** AFM probe functionalized with either a positive charge or hydrophobic chemistry in contact with virus particles covalently bound using the COOH-CH<sub>3</sub> self-assembly monolayer on a gold-coated glass slide in a liquid environment. Image was created with Biorender.com. Adopted from [204].

#### 4.3.1 Differential binding analysis based on buffer pH and conductivity of empty – full AAV capsids.

Initial CFM experiments measured the adhesion between a quaternary amine CFM tip ( $-NR_3^+$ ), and the empty and full AAV3B capsids in buffers with varying pH and conductivities to understand the influence of these buffer conditions on the binding of AAV. Control data can be found in **Figure A.2.1**. We started by exploring the adhesion differences between empty and full AAV3B at low pH. This pH range was selected because it is typical for eluting AAV capsids in affinity chromatography [158, 204]. Also, low pH has been associated with the destabilization of AAV capsids, through structural changes at the 5-fold symmetry, and the induction of side chain amino acids conformation. CFM measurements in this pH range allows us to explore the possibility of capsid instability recognition using CFM [319, 320]. At pH 2.5, differences were observed between the adhesion of empty and full AAV3B capsids, as shown in **Figure 4.4**. For the empty AAV3B capsids at pH 2.5, increasing the conductivity from 10.96 mS/cm to 20.40 mS/cm resulted in a 25 pN adhesion force decrease. This small decrease implies that conductivity did not change the binding of the empty capsids to the positively charged probe at pH 2.5. The full AAV3B capsids at pH 2.5 and conductivity of 10.96 mS/cm bound much stronger to the positively charged probe than the empty capsids, with the difference being 619 pN. However, with an increase in conductivity to 20.40 mS/cm, the adhesion of the full capsids decreased by 704 pN. It is interesting that the full capsids change their charge shielding with conductivity at pH 2.5, whereas the empty capsids do not. When the pH was increased to 4 and a low conductivity of 1.81 mS/cm, the full AAV3B capsids had 181 pN more adhesion force than the empty AAV3B capsids. While some differences between empty and full capsids were observed at lower pHs, higher pHs were also explored.

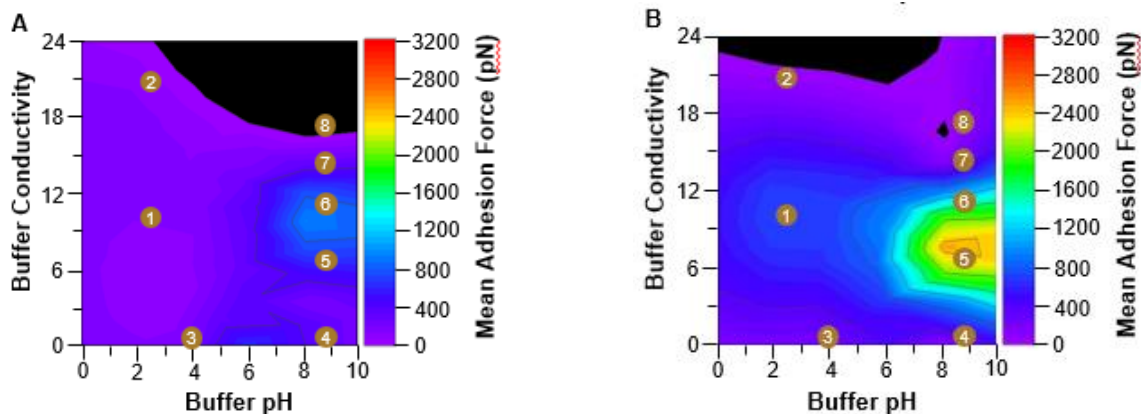


**Figure 4.4: AAV Force measurement as a function of buffer conductivity and pH** (A) Empty capsids (B) Full capsids. The points on this map indicate the solution conditions tested to show the effect of buffer pH and conductivity on the adhesion force.

Higher pHs were explored to determine how empty and full AAV 3B changed adhesion force to the positive probe. pH 8.8 was tested since this is a standard pH used in AEX chromatographic separation of AAV capsids [93, 319]. A difference of 125 pN was measured between the empty and full AAV3B capsids at 1.81 mS/cm and pH 8.8. Adhesion was much stronger at the higher pH to the positively charged probe, as would be expected. The highest measured adhesion difference was 2320 pN at a conductivity of 7.44 mS/cm, as shown in **Figure 4.4**. CFM measurements at pH 8.8 showed the greatest differences in adhesion between the empty and full AAV3B capsids, thus further experimentation was performed using only pH 8.8.

Conditions simulating AEX chromatography were tested to see if CFM adhesion would correlate to chromatography condition. Low conductivity binding conditions (1.81 mS/cm) showed low adhesion to the positive probe, as shown in **Figure 4.4**. This was interesting because this low conductivity condition was used as the binding condition in **Figure 4.2**. As the conductivity increased, the adhesion increased, with a peak for the full particles at 7.44 mS/cm and a peak for the empty particles at 11.48 mS/cm, as shown in **Figure 4.5a**. The peak for the empty particles was much smaller than the full, demonstrating that at intermediate conductivities, the full particles bound much more to the positively charged probe than did the empty. This is as expected because the full capsids are more electronegative [86, 315]. The adhesion histograms for AAV empty and

full capsids showing the adhesion force distribution using  $\text{NR}_3^+$  in the buffers with varying pH and conductivity can be found in **Figure A.2.2** & **Figure A.2.3**.

Interesting trends were observed when correlating the chromatography results with the CFM results. When considering the binding observed at pH 8.8 in AEX chromatography (see, **Figure 4.3b**), we discovered that the full capsids remain bound to the column at conductivities greater than 7.44 mS/cm before they were eluted. The CFM data, however, showed that at a conductivity above 7.44 mS/cm, the full capsids lost their binding strength. This pattern is indicative of a transition not related to charge contributions taking in place in chromatography which allows the full capsids to remain on the AEX column at conductivities above 7.44 mS/cm. This change, however, is not visible on the CFM. This indicates that CFM can only measure binding behavior and not elution behavior. Furthermore, in AEX chromatography, both empty and full capsids were eluted between 13.5 – 16 mS/cm, these corroborates with the CFM results since weak binding is observed for the full AAV capsids above 7.44 mS/cm and above 11.48 mS/cm for the empty capsids.

We hypothesized that the binding of empty and full AAV3B capsids in AEX at low conductivity may be enabled by hydrophobic interactions. This notion was validated by measuring the adhesion of the empty and full AAV3B capsids to a hydrophobic ( $-\text{CH}_3$ ) CFM probe. Control measurements confirmed the probe functionalization, see **Figure A.2.4**. As expected, the empty and full capsids bound strongly to the  $\text{CH}_3$  probe at low conductivity and the binding decreased with increasing conductivity, as shown in **Figure 4.5b**. The histograms for AAV empty and full capsids showing the adhesion force distribution using  $\text{CH}_3$  in the buffers with at pH 8.8 with varying conductivity can be found in **Figure A.2.5**. It was surprising the drop in hydrophobic interaction with the increase in conductivity, as it is assumed that hydrophobic interaction increases at higher ionic strengths. It is likely that this work did not go to a high enough conductivity to salt-out the AAV and increase the hydrophobic interaction.

Considering the behaviors of the empty and full AAV capsids at pH 8.8 with variable buffer conductivity, a secondary hydrophobic interaction may be contributing to the binding. Electrostatic interactions are treated as the sole potential interaction in AEX.

However, when the influence of hydrophobic interactions in the adsorption of alkanols [321] and alkanes [322] to an AEX resin was investigated, a significant connection was observed between the distribution coefficients, and the number of carbon atoms. There was a complementary interaction between hydrophobic and electrostatic interactions for the retention of alkanolic and alkanesulfonic acids in AEX [323]. The CFM findings obtained using CH<sub>3</sub> probes to evaluate AAV capsid adhesion showed that hydrophobic interactions dominate binding at low conductivity. When we compared the CFM data to AEX chromatography at low conductivity (see **Figure 4.2**), we discovered that the AAV capsids showed limited binding at low conductivity in CFM, while the capsid bound firmly in AEX. The binding in AEX at low conductivity might be as a result of hydrophobic interaction between AEX ligand and the AAV capsids. The CFM positive probe is purely positively charged and removes the effect of the column matrix, and potentially any hydrophobic interactions that may be occurring. At low conductivity and high pH, AAV particles bind using hydrophobic interaction and then move to an electrostatic mechanism to stay bound to the chromatography column during AEX. Due to the significance of secondary hydrophobicity in AEX separation, this knowledge is critical for designing and choosing AEX columns for empty and full AAV capsids separation [323]. Since hydrophobic interaction in AEX is dependent on the properties of the matrix, linkers and density of the functional groups on the ligand, if hydrophobic interaction contributes to binding, the AEX column design may need to be modified and buffer conditions optimized to accommodate hydrophobic interaction for improved empty and full capsid separation.

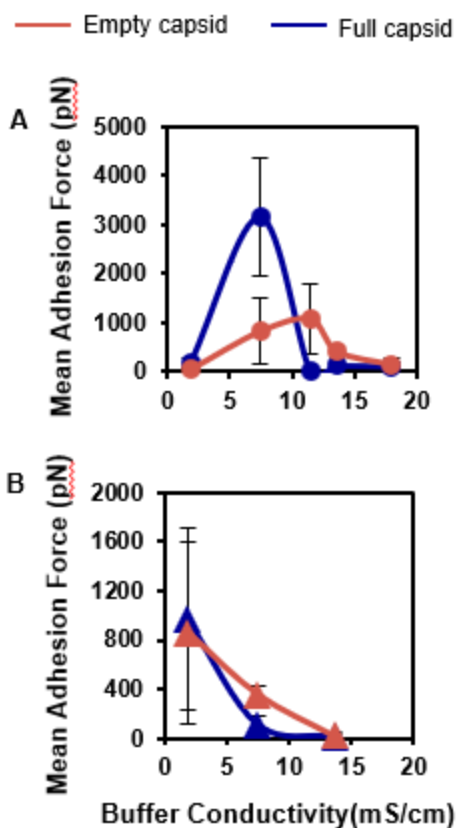


**Figure 4.5: Adhesion forces for AAV at pH 8.8** (A) Adhesion force measurements with a positive NR<sub>3</sub><sup>+</sup> functionalized probe and (B) with hydrophobic CH<sub>3</sub> functionalized probe.

### 4.3.2 Effect of Buffer Composition

The buffers used in the initial studies were mimics of the process conditions, which contained many buffer additives that were left over from previous process unit operations. Some additives were studied separately to better understand the impact of these specific additives to the adhesion of AAV3B to the positive CFM probe (see adhesion histogram in **Figure A.2.6** & **Figure A.2.7**). The base buffers tested at pH 8.8 was 100mM Tris. In the base buffer, there was no difference in binding between the empty and full capsids, as shown in **Figure 4.6a**. Sodium acetate was added to the base buffer to increase the conductivity. The adhesion force of the empty capsids peaked at 135 mM sodium acetate while the adhesion of the full capsids increased with increasing

sodium acetate concentration. At all sodium acetate concentrations tested, the empty capsids bound stronger than the full capsids.

P188, a non-ionic surfactant, was one of the additives of the buffers tested previously. When added at 0.01 w/w%, it greatly changed the binding profile of the empty and full capsids, as shown in **Figure 4.6b**. When P188 was added to the base buffer, the adhesion force measured for the empty capsids decreased with increasing concentration of sodium acetate while that of the full capsids increased with increasing sodium acetate concentration. However, when sodium acetate was completely removed from the buffer leaving only 100 mM Tris and P188, the full capsids had an adhesion force of over 4X times greater than the empty capsids, as shown in **Figure 4.6b**. Although P188 is a nonionic surfactant, its amphiphilic nature may bind to the virus surface and change how the virus interacts with a charged surface.

Another important component of the buffer is magnesium chloride. Addition of magnesium chloride to the base buffer increased the magnitude of adhesion force measured for the empty and full AAV3B capsids, as shown in **Figure 4.6c**. In the buffer containing 100 mM Tris and magnesium chloride, the empty capsids had an adhesion 1.5 times greater than the full capsids. Magnesium chloride is known to preferentially affect full capsids [324]. In AEX chromatography of a recombinant AAV2 showed that magnesium chloride reduces the retention time of the full capsids without affecting the empty capsids. This would imply that the full capsid in the presence of magnesium chloride reduces the negative charge on the virus, which is also what is shown in magnesium ion binding to DNA [325]. In another case, the interaction of 2 mM magnesium chloride with the glutamic acid on AAV8 resulted to the early elution of empty and full AAV8 from a strong quaternary amine column at low conductivity and pH [113], demonstrating that magnesium chloride can have an effect on empty and full capsids, as observed here in the CFM results. However, the binding strength is the opposite of what we see in our CFM results, where magnesium chloride increases binding strength and would thus increase the conductivity needed to elute the vector from an AEX column. Another possibility is that the magnesium chloride may compete for the binding sites of the quaternary amine, thus removing the full virus from the AEX column

at a lower conductivity, however it may not directly bind to the AAV capsid. There is still a lot to be learned about the effect of magnesium on AAV capsids.

Protein-metal ion binding is greatly aided by carboxyl groups, and this is particularly true in terms of chromatographic retention [113]. It was expected that the positive charge of magnesium ions ( $Mg^{2+}$ ) would counteract the negative charges of carboxyl groups on AAV empty and full capsids resulting in decreased binding. However, the effect of  $MgCl_2$  addition to the buffers containing Tris and sodium acetate resulted to an increase in the adhesion of the empty and full AAV capsids as shown in **Figure 4.6d & e**. These results deviate from what was obtained in previous studies on metal mediated charge modification of AAV8. The interaction of  $Mg^{2+}$  (at 2 mM magnesium chloride) with the glutamic acid on AAV8 resulted to the early elution of empty and full AAV8 from a strong quaternary amine column at low conductivity and pH [113]. In our CFM measurements with magnesium chloride, we utilized high pH and a range of conductivity. The CFM results might be indicative of the fact that the metal binding sites are not able to participate in the binding of divalent ions at high pH.

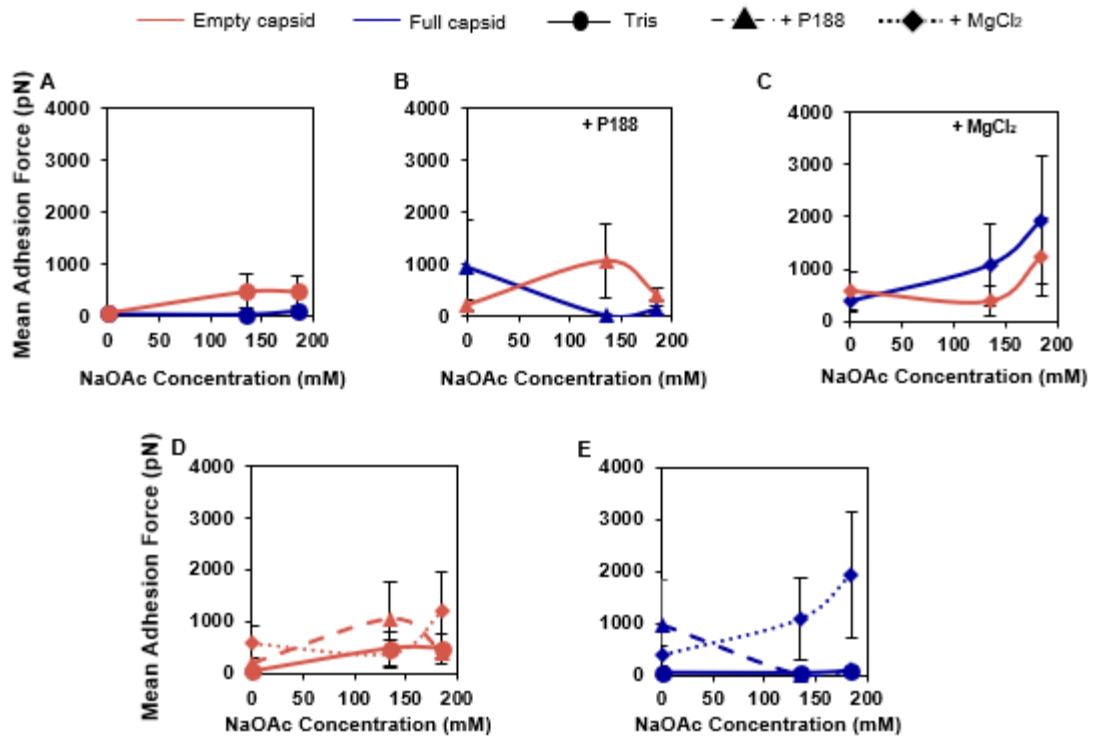


**Figure 4.6: The effect of salt concentration and surfactant at pH 8.8 on empty and full AAV3B.** (A) The adhesion force changes in empty and full capsids when sodium acetate was added to 100 mM Tris buffer. (B) The adhesion force changes in empty and full capsids when 0.01 w/w% P188 was added to sodium acetate + Tris buffer. (C) The adhesion force changes in empty and full capsids when 5mM magnesium chloride was added to sodium acetate + Tris buffer. (D) Effect of 5 mM magnesium chloride, 0.01% P188, and sodium acetate on empty capsids. (E) Effect of 5 mM magnesium chloride, 0.01% P188, and sodium acetate on full capsids.

Buffer conditions can affect the biologic and biophysical characteristics of AAV capsids [120]. In a series of CFM measurements using empty and full AAV capsids, we were able to mimic the chromatographic binding of empty and full AAV capsids to a strong quaternary amine AEX ligand while varying buffer conditions. There is a dependence of AAV capsid stability on pH. The pH can affect the flexibility and repulsion of the capsid proteins [96, 319]. At low pH, in our case at a pH less than 4, although the capsids may look intact, AAV capsids undergo conformational changes in acidic pH [320]. These conformational changes are likely caused by the externalization of the N- terminus of VP 1,2 and 3 protein regions. The N- terminus is positively charged and often tucks into the 5-fold axis to interact with the negatively charged DNA [320].

The externalization of the N- terminus might be responsible for the low adhesion force measured for empty AAV3B capsids at low pH. It is possible that the stronger binding of the full AAV3B capsids as compared to the empty capsids in pH less than 4 resulted from partial genome uncoating. However, it is more likely that changes in the overall charge of the amino acids on the coat of the virus causes this change overall when comparing low and higher pH.

#### **4.4 Conclusions and future work**

The adhesion of empty and full AAV to a strong positively charged quaternary amine probe was investigated in buffers with varying compositions, pH, and conductivity using CFM to simulate column chromatography conditions. From the CFM results obtained we were able to measure differences in the binding of empty and full AAV3B capsids to a positively charged quaternary amine surface. This information allowed us to understand that although anion exchange chromatography is described primarily based on electrostatic interactions, secondary hydrophobic interaction dominates binding at low conductivities and pH. Interesting binding trends for the addition of surfactant and magnesium chloride have also shown that the interaction of magnesium chloride greatly increases the binding of empty and full AAV3B capsids to a positively charged probe. This is the opposite often seen in chromatography where the addition of magnesium chloride often has the capsids eluting earlier than without magnesium chloride. The results points to the benefit that can be obtained in using CFM as a buffer selection and optimization tool needed to understand how the AAV capsids would bind in a chromatography run.

Future work for this project includes using the CFM to understand the effect of divalent ions at different concentrations and pH. The current study found that  $MgCl_2$  at high pH increased the binding of empty and full capsids to a strong AEX column.  $MgCl_2$  should be tested for its effect on the separation of empty and full AAV at lower pH ranges. Also, the effect of other salts with divalent ions such as  $CaCl_2$ , at high and low pH with varying concentrations should be explored on empty and full capsids separation

## **5 Single-Particle Characterization of SARS-CoV-2 Isoelectric Point and Comparison to Variants of Interest**

### **5.1 Introduction**

The recent pandemic involving SARS-CoV-2, which causes COVID-19, represents serious and emerging threats worldwide. While the majority of COVID-19 cases are largely asymptomatic or mild clinical presentation, some can be severe or deadly in infected patients. Severe cases often develop acute respiratory distress syndrome and are deadly in spite of intubation, mechanical ventilation, and costly ICU care. Viruses, like SARS-CoV-2 are single-stranded, RNA macromolecules that have complex surface physicochemical properties, which give rise to their adsorption behavior. The adsorption of viruses to surfaces could give rise to increased transmission. BLAST and FASTA scans are typical search tools, which are performed on a nucleotide or amino acid sequence to impart structural information or predict the protein function. Information from other structural methods, like protein crystallography, helps to elucidate function and behavior. However, we sometimes find that the prediction of function and other features, like isoelectric point (IEP) are not accurate and experimental measurements must be performed.

Understanding virus adsorption can help to facilitate safe practices. For example, learning how to repel viruses from surfaces or to adsorb them could be used to improve filtration devices and personal protective equipment. The physicochemical properties of the virus paired with environmental conditions facilitate virus adsorption [326, 327]. The adhesion mechanism through which viruses are adsorbed is driven by electrostatic [328] and van der Waals interactions [329] as described by the extended Derjaguin–Landau–Verwey–Overbeek (XDLVO) model [140, 330]. These interactions are controlled by environmental factors such as pH, temperature, and humidity [331]. Disrupting the adsorption of a virus to a surface can be achieved by manipulating the factors that contribute to the interactions.

Viruses have extremely complicated structures, as compared to proteins. One of the most prominent interactions for adsorption is electrostatic. While proteins can be described by their charge and IEP, which is the pH at which they are neutrally charged [88, 203], this type of description is more difficult for viral particles. Non-enveloped viruses have a protein shell that folds into a large nanoparticle structure. However, enveloped viruses, like SARS-CoV-2, have glycosylations and a lipid bilayer, making surface characterization much more difficult to predict and require experimental measurements.

Conventional methods for measuring virus IEP use bulk viral solutions. Zeta potential measures the electrostatic potential difference between the electric double layer surrounding the virus particle and the surrounding solution at the shear plane [332]. However, zeta potential requires a large volume of highly concentrated virus sample and is limited by virus solubility [333] and the presence of impurities [120]. Another IEP measurement is isoelectric focusing (IEF) using gels [334] and capillary isoelectric focusing (CIEF) [335]. IEF requires the fluorescent tagging of viruses, which requires pure, concentrated solutions [336]. Different methods are needed to measure virus IEP in natural solutions without high purity and concentration requirements.

We have developed a single-particle method to measure the IEP of virus with an atomic force microscope (AFM). The technique, called chemical force microscopy (CFM), uses a functionalized AFM tip to measure the adhesion force of the functionalized AFM tip and the virus immobilized on a surface [158, 200]. The adhesion is measured in different pH solutions, thus measuring a range of electrostatic interactions near the IEP. The IEP for the non-enveloped porcine parvovirus was found to be 4.8-5.1 [158] and this was found to be similar as the value determined by IEF of 5.0 [337]. However, when the IEP for the main surface protein was calculated with UniProtKB using the entire protein sequence, the IEP was determined to be 5.8 [158]. For the enveloped virus bovine viral diarrhea virus (BVDV), the discrepancy between the measured IEP value with CFM and the calculation of the IEP of the main spike protein was even greater, at 4.3-4.5 and 6.9, respectively [158]. Due to the post translational modifications, glycosylations, and lipid membrane, it is more imperative that enveloped

viruses have a measured IEP and not just use the calculated value from the spike protein amino acid sequence.

The IEP of SARS-CoV-2 has been calculated in different ways and can be found in **Table 5.1**. The IEP ranges from 5.2-6.2. This is a large range when the goal is to either adsorb or trap the virus or to repel it using electrostatic forces. The IEP values were obtained based on the identified proteins on SARS-CoV-2. The FASTA sequence was input into the ProtParam tool from the Bioinformatics Resource Portal ExPASy [338] to obtain the values of the IEP based on the protein sequence. A major disadvantage is that calculated IEP values do not consider that some amino acids are buried when the protein folds or any post translational modifications.

**Table 5.1.** Summary of current IEP values for SARS-CoV-2 S protein

Calculation/Method	Protein	IEP	Reference
Amino acid sequence	SARS-CoV-2 spike glycoprotein	5.9	[339]
ProtParam	SARS-CoV-2 spike glycoprotein	6.24	[116]
ProtParam	His-tagged SARS-CoV-2 RBD <sup>1</sup>	8.91	[335]
CIEF	His-tagged SARS-CoV-2 RBD <sup>1</sup>	7.36-9.85	[335]
CIEF	S1/S2 subunit with His-tag	4.41-5.87	[335]

<sup>1</sup>RBD – receptor binding domain

## 5.2 Materials and Methods

### 5.2.1 Materials

Sodium phosphate dibasic heptahydrate (ACS grade, 98.0–102.0%), sodium phosphate monobasic monohydrate (ACS grade, 98.0–102.0%), sodium chloride (ACS grade, ≥99.0%), sodium citrate tribasic dihydrate (ACS reagent, ≥99%), 11-mercaptoundecyl-N, N, N-trimethylammonium bromide (HS(CH<sub>2</sub>)<sub>11</sub>N(CH<sub>3</sub>)<sub>3</sub>Br), 12-mercaptododecanoic acid (HS (CH<sub>2</sub>)<sub>11</sub>COOH, 96%), 1-dodecanethiol (HS(CH<sub>2</sub>)<sub>11</sub>CH<sub>3</sub>, ≥ 98%), were purchased from Sigma-Aldrich (St. Louis, MO). N-hydroxysulfosuccinimide (NHS) and 1-ethyl-3-(3-dimethylaminopropyl) carbodiimide hydrochloride (EDC), and plain microscope slides (25 x 75 x 1mm) were purchased from ThermoFisher Scientific

(Waltham, MA). CSG10/Au and CSG30 probes were purchased from NT-MDT Spectrum Instruments (Moscow, Russia). Ethanol 200 proof was purchased from Decon Labs. Inc (King of Prussia, PA). All aqueous solutions or buffers were prepared using purified water with a resistivity of  $\geq 18 \text{ M}\Omega \cdot \text{cm}$  from a nanopore filtration system (Thermo Scientific) and filtered using a  $0.2 \mu\text{m}$  disposable bottle top filter before use.

## 5.2.2 Methods

### 5.2.2.1 *Virus samples, AFM probe functionalization and control surface preparation*

Using a Perkin-Elmer Randex sputtering system (Model 2400, Waltham, MA), cleaned glass slides were coated with 5 nm chromium followed by a gold layer of 35 nm. The gold-coated glass slides were washed with 100% ethanol heated to  $65^\circ\text{C}$ , dried, and kept in a clean petri-dish until use. The virus particles were immobilized using the same methodology as in our earlier study of virus isoelectric points [158].

The force probes employed for force measurements were the NT-MDT CSG10/Au AFM probes (spring constant - 0.1 – 0.5 N/m, tip radius – 10 nm. For positive charge functionalization, the AFM probes were immersed in a clean petri-dish containing 14 ml of 4mM  $\text{HS}(\text{CH}_2)_{11}\text{N}(\text{CH}_3)_3\text{Br}$  in ethanol for 48hrs while for negative charge, probes were immersed in carboxyl ( $\text{COOH}^-$ ) in 14 ml of 4 mM  $\text{HS}(\text{CH}_2)_{11}\text{COOH}$  in ethanol for 24hrs. Following immersion, the probes were washed with 25ml ethanol, dried in a chemical hood, and carefully stored in a clean AFM probe box. The functionalized probes lasted 96 hours and were checked using the control gold-coated glass slides to guarantee functionalization before usage. Control surfaces utilized to check probe functionalization was prepared using method similar to that for probe functionalization.

### 5.2.2.2 *Preparation of buffers*

Sodium acetate solution was prepared by making a 135 mM and 185 mM solution and magnesium chloride solution was prepared by making a 5 mM solution. Tris-HCl

solution was prepared by making a 100 mM solution with Trizma base. A solution of 1M NaOH or HCl was used to adjust the acidic or basic level, and pH was measured with a calibrated Fisherbrand Accumet AE150 benchtop pH meter (Hampton, NH).

### 5.2.2.3 Force measurements and analysis

Using a Bruker Dimension ICON atomic force microscope equipped with the ScanAsyst system in peak force quantitative nanoscale mechanical mode (Peakforce QNM) and the corresponding functionalized NT-MDT CSG10/Au AFM probes, charge force measurements were obtained. At the beginning of every force measurement, the spring constant of modified AFM probes was calibrated using the thermal tuning function on the AFM. The solution used for force measurements were either 20mM CB between pH 4 – 6 or 20 mM PB at pH 7.0. Every virus was probed once at two different points based on the virus diameter /modified probe radius of curvature ratio. Areas around the edges of the virus was avoided to prevent probing the glass surface without virus due to minor deflections experienced by the probe during measurements in liquid environment. All experiments were performed at room temperature. For each probe/sample combination at least 150 F-D curves were obtained. Force measurements was done in triplicates resulting to at least 450 F-D curves being made available for analysis. Taking into consideration every data point including those without any force (zero force was recorded at some point), data analysis was performed with the Bruker Nanoscope Analysis software.

## 5.3 Results and Discussion

We have used CFM to measure the IEP of SARS-CoV-2. Heat inactivated and gamma irradiated SARS-CoV-2 (USA-WA1/2020) isolate from BEI resources were covalently bound to a glass slide (see **Figure 5.1a**) and height analysis was performed on a Bruker Dimension ICON AFM with the ScanAsyst system (Santa Barbara,CA) using a Bruker AC-40 AFM probe. The heat inactivated virus contained many small particles (**Figure A.3.1**) and was not further tested. The virus was immobilized on a glass slide and adhesion measurements were carried out with a positive quaternary amine AFM probe

and a negative carboxylic acid AFM probe, as described previously [158, 200] (**Figure 5.1**). The measured IEP for SARS-CoV-2 (USA-WA1/2020) was 5.2-5.3. This is on the low end of the IEPs from calculated sources shown in **Table 5.1**.

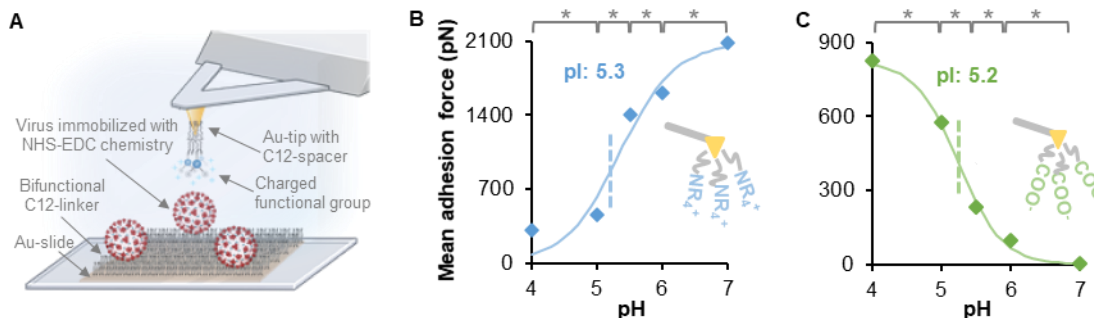


**Figure 5.1: Isoelectric point determination using CFM.** (A) Inactivated SARS-CoV-2 particles were covalently immobilized on a Au-coated slide that contained a self-assembled monolayer that presented COOH and CH<sub>3</sub> functional groups. NHS/EDC chemistry covalently bound the virus to the COOH groups [158, 200]. Au tips were functionalized to provide either negatively charged carboxyl (COO<sup>-</sup>) or positively charged quaternary amine (NR<sub>4</sub><sup>+</sup>) groups. Changes in the mean adhesion forces were measured with respect to pH with (B) a NR<sub>4</sub><sup>+</sup> probe or (C) a COO<sup>-</sup> probe. The data points of the mean adhesion force vs. pH were fit to a sigmoidal curve and the IEP was determined to be the infection point. The histogram of each individual point can be found in **Figure A.3.2**. \*p<0.05 from student's t-test. (Image A was created in BioRender.com).

Since only the wild type (USA-WA1/2020) could be obtained for experimental study, we compared the charge differences between two other variants of interest (VOI) that are currently circulating of SARS-CoV-2, B.1.1.7 and B.1.351. The charge of the WT virus and the variants can be found in **Figure 5.2**. The mutations are found in different parts of the spike protein, including the receptor binding domain and the furin cleavage site [340].

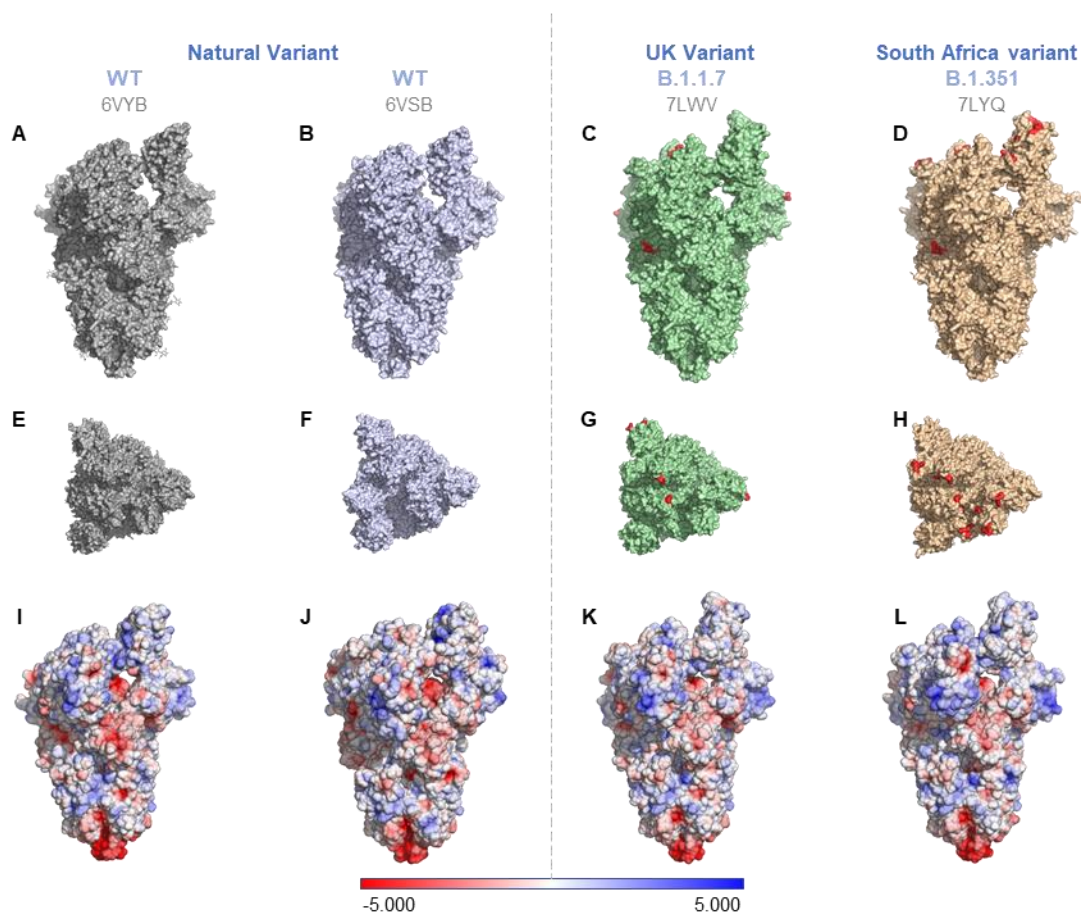


**Figure 5.2: Comparison of the mutations (Row 1 and 2) and surface electrostatic potentials (Row 3) on spike proteins of two VOIs with respect to the WT.** WT(PDB ID: 6VYB [341] (1<sup>st</sup> column) and 6VSB [342] (2<sup>nd</sup> column), B.1.1.7 (PDB ID: 7LWV [340]) and B.1.351 (PDB ID: 7LYQ [340])). (A-D) show the side view, 1<sup>st</sup> row, and (E-H) show the top view, 2<sup>nd</sup> row. For the VOIs, the AA mutations on the S proteins (see **Table 5.2** for details) are marked red with one residue before and after the actual mutational site for better visibility. (I-L) S-protein surface potentials of the WT and VOIs. The surface potentials were generated by preparing molecules with the pdb2pqr method and applying APBS electrostatics using PyMol v2.4.1.

The exact surface mutations of the WT and VOIs are found in **Table 5.2**. The charge density on the surface of the spike protein decreases in the VOIs. This would likely increase the IEP of the VOIs as compared to the WT. The charge on the RBD was slightly higher for the WT as compared to the two variants when 6VYB was used as the WT model (**Table 5.2**). However, the WT RBD charge was lower compared to the VOIs when 6VSB was used as a reference. Additionally, the E484K mutation made the B.1.351

variant slightly more positive compared to the B.1.1.7 variant. A similar effect was observed for surface hydrophobicity (**Table A.3.1**). The surface hydrophobicity was calculated by applying the Eisenberg hydrophobicity scale for the surface exposed residues [16] (**Figure A.3.3**). The WT was more hydrophobic as compared to the VOIs (**Table A.3.1**). Between the two VOIs, B.1.351 was more hydrophobic than B.1.1.7.

**Table 5.2.** Comparison of surface charge on S protein of the two VOI with the wild type.

Pango Lineage	Name	Mutations	PDB	Surface Charge (formal charge)	Surface Charge (partial charge)	RBD Charge
WT (Natural variant)	USA/WA1/2020	-	6VYB	-20	-17	9
		-	6VSB	-26	-23	6
B.1.1.7 (UK variant)	20J/501Y.V1	Δ69/70 Δ144Y N501Y A570D D614G P681H	7LWV	-12	-9	7
B.1.351 (South Africa variant)	20H/501.V2	K417N E484K N501Y D614G	7LYQ	-7	-4	8

Surface charges are based on the solvent accessible (SA) residues calculated in PyMol using APBS electrostatics. The boundary conditions used for single Debye-Huckel function were – solute dielectric constant: 2.000; solvent dielectric constant: 78.000; ionic strength: 150 mM; temperature: 310 K. RBD charges were calculated by adding the partial charges of the SA residues in the 319-541 region of chain B for 6VYB, 7LWV, and 7LYQ or chain A for 6VSB. The chain consideration was based on the chain identifier that showed an up configuration of the RBD in PyMol.

## 5.4 Conclusion

The IEP of SARS-CoV-2 was determined using CFM. The IEP in 20 mM salt was 5.2-5.3. This is on the low end of values calculated from different amino acid sequences of the spike protein. Enveloped viruses contain glycosylations on their spike proteins that likely change the IEP, thus requiring a measured IEP compared to a calculated IEP. CFM is a novel method to measure virus IEP, which does not require high purity and high concentration virus stocks. It is a single particle method that targets the virus particles individually for the measurement. Without access to VOI of SARS-CoV-2, their

sequence changes were used to calculate the change in surface charge and hydrophobicity as compared to WT. The VOI have a lower charge and lower hydrophobicity than the WT, and this may play a role in the increased transmission of the VOIs.

## 6 Conclusions and future work

### 6.1 Conclusions

In this dissertation, we were able to demonstrate the use of chemical force microscopy (CFM) in the characterization of the charge and hydrophobicity of viruses. CFM provides the opportunity to measure virus charge and hydrophobicity on a single - particle level which allows the inclusion of heterogeneity across a virus population in the characterization of these surface properties. CFM utilizes the tip of an atomic force microscope (AFM) which can be modified using any chemistry of interest. The adhesion force between the AFM tip and the virus surface is then measured and translated into binding interactions. The viruses to be measured in CFM were covalently attached to the surface of a gold coated glass slide. The covalent bonding was used to prevent the viruses from being pulled off the gold surface during measurement, and to ensure that the bonds being broken were between the virus and CFM tip and not the virus – gold surface bond. The first CFM measurement was the characterization of the hydrophobicity for porcine parvovirus (PPV), and bovine viral diarrhea virus (BVDV) as discussed in Chapter 3. The second and third set of CFM measurements focused on characterizing the hydrophobicity and charge of Adeno Associated Virus 3B (AAV3B) empty and full capsids and was discussed in Chapter 4. The charge characterization of SARS-CoV-2 used in estimating the isoelectric point based on CFM measurements was discussed in Chapter 5.

We have used a CFM probe with methyl group to study the hydrophobicity of PPV and BVDV as a function of buffer compositions. The goal of this project was to ascertain the ability of CFM to measure virus hydrophobic interaction and detect changes in this hydrophobic interaction when buffer condition changes. Phosphate buffer saline (PBS) was used as the base buffer composition. The salt concentration was increased through sodium chloride addition. Additives that can alter hydrophobic interactions was also added. The CFM was able to measure virus hydrophobicity in the base buffer and record changes in the hydrophobicity as buffer composition changed. We determined that BVDV is much more hydrophobic than PPV in PBS. The hydrophobicity of PPV and BVDV increased with the addition of PEG. The addition of ethanol resulted to an

increase in the hydrophobicity of PPV but not that of BVDV. The CFM results were also compared to virus dye adsorption measurements which utilized hydrophobic Rose Bengal and hydrophilic Nile Blue. The concentrations of the dye were varied while that of PPV and BVDV were kept constant. The dye adsorption experiments were used to characterize virus hydrophobicity changes with increasing NaCl concentrations in PBS. The dye adsorption results only showed good correlation for CFM with ethanol. This finding implies that, owing to the complexity of the viral surface, a hydrophobicity characterization approach capable of isolating hydrophobic and non-hydrophobic interactions responsible for virus adhesion or binding to a substrate is required. As a consequence, it is critical to measure viral hydrophobicity at the single-particle level using CFM in order to account for variability within the virus population and to filter out non-hydrophobic interactions. A solid and dependable technique of quantifying viral hydrophobicity like CFM may aid in the optimization of virus purification systems, buffer selection, gene therapy, and medication administration.

The charge and hydrophobicity of AAV3B empty and full capsids was characterized using CFM. The hydrophobicity of AAV3B was measured using the methyl-terminated CFM probes in buffers containing varying salt concentrations. The hydrophobicity of empty and full AAV3B capsids was high at low salt concentrations but diminished at higher salt concentrations due to the dominance of electrostatic interactions. A quaternary amine – terminated AFM probe was utilized to measure differences in the surface charge of empty and full AAV3B capsids at various solution composition, conductivity, and pH. CFM measurements showed that there are differences between the charge distribution on the empty and full AAV3B capsids. The comparison of CFM to chromatography showed that through the conductivity transitions in chromatography, the binding of the empty and full AAV3B capsids changes. This conductivity coupled with the pH and salt concentrations plays a huge role in virus binding for anion exchange chromatography (AEX). At low pH for empty and full AAV3B capsids, we were able to deduce that the capsid bind to a strong AEX column through hydrophobic interactions. The knowledge of the differences between the empty and full AAV3B capsids can help in designing and optimizing chromatographic systems

for virus purification. This will also help in the separation of empty capsids from the virus full capsids pool required for inducing the therapeutic effects for gene therapy.

AFM tips modified with carboxyl, and quaternary amine group chemistries at different pH was used to study the charge property of SARS-CoV-2 virus. The mean adhesion force obtained from the CFM measurements was plotted as a function of solution pH and fitted to a sigmoidal curve. The point of inflection from the sigmoidal curve plot was identified as the virus isoelectric point (pI). The pI for SARS-CoV-2 as determined by the CFM was 5.2 – 5.3. These values are within the range of theoretical values reported for SARS-CoV-2 pI. The experimental pI value for the wild type (WT) SARS-CoV-2 was compared to two other variants using pyMol a computational tool. It was observed that the variants had a lower charge and hydrophobicity than the WT. Theoretical calculation are not able to consider modification of virus envelope, and conformational changes of virus surface amino acids, hence, are not able to provide an accurate measure of the virus pI. As a result, an experimental technique like the CFM which can account for changes in the virus envelope and amino acids is required. Biologic purification and delivery techniques which relies on the virus charge would greatly benefit from the use of CFM to characterize virus charge. This was the first experimental determination of SARS-CoV-2 isoelectric point.

## **6.2 Future work**

In this dissertation, CFM has been used extensively to characterize the charge and hydrophobicity of viruses. However, method modifications for the AFM equipment software, as well as other experiments for virus surface measurements, can be investigated. For the CFM, current equipment has been allowed to operate in the 'relative' trigger mode, generating trigger threshold force values based on the softness of the material with which the probe comes into contact during measurement. However, to ensure that the same trigger threshold force is applied regardless of the equipment used, an experiment to determine the trigger threshold force value for a specific virus to be measured should be carried out. This entails testing at least three different trigger

threshold forces to see which burst the virus, have the least adhesion force, and have the optimum adhesion force. The trigger mode should be in absolute for this to be done. In addition, when calibrating the CFM tips, the spring constants of all probes to be used for a virus in a specific solution condition should be within the same range to ensure similar probe deflection for triplicate measurements.

The viruses used in this study was purified using both chromatographic and non-chromatographic techniques. The solution conditions for these purification techniques differ and is capable of effecting changes to the charge distribution and hydrophobic interaction of virus surface proteins. Experiments with CFM to measure the effect of purification techniques on the charge and hydrophobicity of viruses should be investigated. It would be an interesting study to determine the extent to which the method of purification affects the virus surface properties. Currently, no such research has been conducted using mammalian viruses. Common laboratory non-chromatographic techniques to separate virus from impurities like dialysis ultracentrifugation, and PEG precipitation can be used while for chromatographic techniques, AEX and static hydrophobic interaction chromatography can be exploited. To study the effect of purification techniques on charge and hydrophicity, the methods utilized in chapter 3-5 can be exploited.

Currently, in the purification of gene therapy vectors, different purification steps are combined to optimize empty and full virus separation. These combinations of purification techniques also affect the yield of virus. Asides from exploring the effect of purification techniques on virus hydrophobicity and charge, the effect on recovery, final protein concentration and DNA removal should also be explored. To assess the final recovery after purification, the initial and final recovery volumes and concnetrations should be obtained. This results can be expressed as a percentage of initial volume and concentration. The final protein concentration can be evaluated using the Bradford assay. The Bradford assay is a simple colorimetric assay for determining protein concentration based on the binding of the assay reagents (Coomassie Brilliant Blue G-250) to proteins [343]. The DNA concentration can be quantified using the picogreen assy which allows for the selective detection of as low as 25 pg/ml of double -stranded DNA (dsDNA)

present in a virus sample [344]. The charge and hydrophobicity differences, level of DNA removal, recovery, and protein concentration can be compared for all the methods tested. This comparison can act as a guide in the combination of purifications techniques for virus separation. It can also provide information on what purification technique would be best fit for a certain type of virus surface characterization evaluation. Lastly, to convince industry to adopt CFM as a virus surface characterization or for use in optimizing purification systems, a catalog of the expected differences based on the type of purification process the test material is generated from is important.

## 7 References

1. Dunbar, C.E., et al., *Gene therapy comes of age*. Science, 2018. **359**(6372): p. eaan4672.
2. Keeler, A., M. ElMallah, and T. Flotte, *Gene Therapy 2017: Progress and Future Directions*. Clinical and Translational Science, 2017. **10**(4): p. 242-248.
3. Wirth, T., N. Parker, and S. Ylä-Herttuala, *History of gene therapy*. Gene, 2013. **525**(2): p. 162-169.
4. Moirano, J. and M.E. Emborg, *CHAPTER 9 - Nonhuman Primate Models for Testing Gene Therapy for Neurodegenerative Disorders*, in *Gene Therapy of the Central Nervous System*, M.G. Kaplitt and M.J. During, Editors. 2006, Academic Press: Amsterdam. p. 109-119.
5. Dwivedi, S., et al., *Chapter 22 - Genetic Engineering: Towards Gene Therapy and Molecular Medicine*, in *Omics Technologies and Bio-Engineering*, D. Barh and V. Azevedo, Editors. 2018, Academic Press. p. 507-532.
6. McKusick, V.A. *Online Mendelian Inheritance in Man*. OMIM 1987 [cited 2022 September 9]; Available from: <https://www.ncbi.nlm.nih.gov/omim>.
7. Ginn, S., et al., *Gene therapy clinical trials worldwide to 2012 - an update*. *J Gene Med*, 2013. **15**: p. 65-77.
8. Goswami, R., et al., *Gene Therapy Leaves a Vicious Cycle*. *Frontiers in oncology*, 2019. **9**: p. 297.
9. Gonçalves, G. and R. Paiva, *Gene therapy: advances, challenges and perspectives*. Einstein (Sao Paulo, Brazil), 2017. **15**: p. 369-375.
10. Czermak, P., et al., *Purification of the densonucleosis virus by tangential flow ultrafiltration and by ion exchange membranes*. *Desalination*, 2008. **224**(1): p. 23-27.
11. Lundstrom, K., *Viral vectors in gene therapy*. *Diseases*, 2018. **6**(2): p. 42.
12. Samra, B., et al., *Evolving therapy of adult acute lymphoblastic leukemia: state-of-the-art treatment and future directions*. *Journal of Hematology & Oncology*, 2020. **13**(1): p. 70.
13. Arruda, V.R. and B.J. Samelson-Jones, *Obstacles and future of gene therapy for hemophilia*. *Expert Opin Orphan Drugs*, 2015. **3**(9): p. 997-1010.
14. Kay, M.A., *State-of-the-art gene-based therapies: the road ahead*. *Nature Reviews Genetics*, 2011. **12**(5): p. 316-328.
15. Armanious, A., et al., *Viruses at Solid-Water Interfaces: A Systematic Assessment of Interactions Driving Adsorption*. *Environ Sci Technol*, 2016. **50**(2): p. 732-43.
16. Heldt, C.L., et al., *Experimental and computational surface hydrophobicity analysis of a non-enveloped virus and proteins*. *Colloids Surf B Biointerfaces*, 2017. **153**: p. 77-84.
17. Mi, X., et al., *Virus Isoelectric Point Determination Using Single-Particle Chemical Force Microscopy*. *Langmuir*, 2020. **36**(1): p. 370-378.
18. Shi, H. and V.V. Tarabara, *Charge, size distribution and hydrophobicity of viruses: Effect of propagation and purification methods*. *J Virol Methods*, 2018. **256**: p. 123-132.

19. Dika, C., et al., *Impact of the virus purification protocol on aggregation and electrokinetics of MS2 phages and corresponding virus-like particles*. Physical Chemistry Chemical Physics, 2013. **15**(15): p. 5691-5700.
20. Mi, X., et al., *Virus isoelectric point determination using single-particle chemical force microscopy*. Langmuir, 2019.
21. Bulaklak, K. and C.A. Gersbach, *The once and future gene therapy*. Nat Commun, 2020. **11**(1): p. 5820.
22. Mendell, J.R., et al., *Assessment of Systemic Delivery of rAAVrh74.MHCK7.micro-dystrophin in Children With Duchenne Muscular Dystrophy: A Nonrandomized Controlled Trial*. JAMA Neurol, 2020. **77**(9): p. 1122-1131.
23. Pasi, K.J., et al., *Multiyear Follow-up of AAV5-hFVIII-SQ Gene Therapy for Hemophilia A*. New England Journal of Medicine, 2020. **382**(1): p. 29-40.
24. Jenks, S., *Gene therapy death--"everyone has to share in the guilt"*. J Natl Cancer Inst, 2000. **92**(2): p. 98-100.
25. Boutin, S., et al., *Prevalence of serum IgG and neutralizing factors against adeno-associated virus (AAV) types 1, 2, 5, 6, 8, and 9 in the healthy population: implications for gene therapy using AAV vectors*. Hum Gene Ther, 2010. **21**(6): p. 704-12.
26. Tse, L.V., et al., *Structure-guided evolution of antigenically distinct adeno-associated virus variants for immune evasion*. Proc Natl Acad Sci U S A, 2017. **114**(24): p. E4812-e4821.
27. Maheshri, N., et al., *Directed evolution of adeno-associated virus yields enhanced gene delivery vectors*. Nat Biotechnol, 2006. **24**(2): p. 198-204.
28. Leborgne, C., et al., *IgG-cleaving endopeptidase enables in vivo gene therapy in the presence of anti-AAV neutralizing antibodies*. Nat Med, 2020. **26**(7): p. 1096-1101.
29. Corti, M., et al., *B-Cell Depletion is Protective Against Anti-AAV Capsid Immune Response: A Human Subject Case Study*. Mol Ther Methods Clin Dev, 2014. **1**: p. 14033-.
30. Meliani, A., et al., *Antigen-selective modulation of AAV immunogenicity with tolerogenic rapamycin nanoparticles enables successful vector re-administration*. Nat Commun, 2018. **9**(1): p. 4098.
31. Misra, S., *Human gene therapy: a brief overview of the genetic revolution*. J Assoc Physicians India, 2013. **61**(2): p. 127-33.
32. Wirth, T., N. Parker, and S. Yla-Herttuala, *History of gene therapy*. Gene, 2013. **525**(2): p. 162-9.
33. Yin, H., et al., *Non-viral vectors for gene-based therapy*. Nature Reviews Genetics, 2014. **15**(8): p. 541-555.
34. Butt, M.H., et al., *Appraisal for the Potential of Viral and Nonviral Vectors in Gene Therapy: A Review*. Genes (Basel), 2022. **13**(8).
35. Thomas, C.E., A. Ehrhardt, and M.A. Kay, *Progress and problems with the use of viral vectors for gene therapy*. Nature Reviews Genetics, 2003. **4**(5): p. 346-358.
36. Finer, M. and J. Glorioso, *A brief account of viral vectors and their promise for gene therapy*. Gene Therapy, 2017. **24**(1): p. 1-2.

37. van der Loo, J.C. and J.F. Wright, *Progress and challenges in viral vector manufacturing*. Human molecular genetics, 2016. **25**(R1): p. R42-R52.
38. Ginn, S.L., et al., *Gene therapy clinical trials worldwide to 2017: An update*. The Journal of Gene Medicine, 2018. **20**(5): p. e3015.
39. Sung, Y. and S. Kim, *Recent advances in the development of gene delivery systems*. Biomaterials research, 2019. **23**(1): p. 8.
40. Nayerossadat, N., T. Maedeh, and P.A. Ali, *Viral and nonviral delivery systems for gene delivery*. Advanced biomedical research, 2012. **1**.
41. Bono, N., et al., *Non-Viral in Vitro Gene Delivery: It is Now Time to Set the Bar!* Pharmaceutics, 2020. **12**(2): p. 183.
42. Davis, M.E., *Non-viral gene delivery systems*. Current opinion in biotechnology, 2002. **13**(2): p. 128-131.
43. Hull, R., *Chapter 5 - Agents Resembling or Altering Virus Diseases*, in *Plant Virology (Fifth Edition)*, R. Hull, Editor. 2014, Academic Press: Boston. p. 199-243.
44. Ramamoorth, M. and A. Narvekar, *Non viral vectors in gene therapy- an overview*. J Clin Diagn Res, 2015. **9**(1): p. Ge01-6.
45. Jinturkar, K.A. and A. Misra, *2 - Challenges and Opportunities in Gene Delivery*, in *Challenges in Delivery of Therapeutic Genomics and Proteomics*, A. Misra, Editor. 2011, Elsevier: London. p. 45-82.
46. Devarakonda, S., et al., *Cost-Effective and Handmade Paper-Based Immunosensing Device for Electrochemical Detection of Influenza Virus*. Sensors, 2017. **17**(11): p. 13.
47. Acheson, N., *Fundamentals of Molecular Virology*. 2011.
48. Namvar, A., et al., *Physicochemical properties of polymers: An important system to overcome the cell barriers in gene transfection*. Biopolymers, 2015. **103**(7): p. 363-75.
49. Waehler, R., S.J. Russell, and D.T. Curiel, *Engineering targeted viral vectors for gene therapy*. Nature reviews genetics, 2007. **8**(8): p. 573-587.
50. Sano, A., et al., *Atelocollagen for protein and gene delivery*. Adv Drug Deliv Rev, 2003. **55**(12): p. 1651-77.
51. Tros de Ilarduya, C., Y. Sun, and N. Düzgüneş, *Gene delivery by lipoplexes and polyplexes*. Eur J Pharm Sci, 2010. **40**(3): p. 159-70.
52. Warnock, J.N., C. Daigre, and M. Al-Rubeai, *Introduction to Viral Vectors*, in *Viral Vectors for Gene Therapy: Methods and Protocols*, O.-W. Merten and M. Al-Rubeai, Editors. 2011, Humana Press: Totowa, NJ. p. 1-25.
53. Ghosh, S., et al., *Viral Vector Systems for Gene Therapy: A Comprehensive Literature Review of Progress and Biosafety Challenges*. Appl Biosaf, 2020. **25**(1): p. 7-18.
54. Colella, P., G. Ronzitti, and F. Mingozzi, *Emerging Issues in AAV-Mediated In Vivo Gene Therapy*. Molecular Therapy - Methods & Clinical Development, 2018. **8**: p. 87-104.
55. Ylä-Herttua, S., *Endgame: glybera finally recommended for approval as the first gene therapy drug in the European union*. Mol Ther, 2012. **20**(10): p. 1831-2.

56. Wang, D., P.W.L. Tai, and G. Gao, *Adeno-associated virus vector as a platform for gene therapy delivery*. Nat Rev Drug Discov, 2019. **18**(5): p. 358-378.
57. Jacobson, S.G., et al., *Gene therapy for leber congenital amaurosis caused by RPE65 mutations: safety and efficacy in 15 children and adults followed up to 3 years*. Arch Ophthalmol, 2012. **130**(1): p. 9-24.
58. Ferreira, V., H. Petry, and F. Salmon, *Immune Responses to AAV-Vectors, the Glybera Example from Bench to Bedside*. Front Immunol, 2014. **5**: p. 82.
59. Balakrishnan, B. and G. R Jayandharan, *Basic biology of adeno-associated virus (AAV) vectors used in gene therapy*. Current gene therapy, 2014. **14**(2): p. 86-100.
60. Sonntag, F., K. Schmidt, and J.A. Kleinschmidt, *A viral assembly factor promotes AAV2 capsid formation in the nucleolus*. Proceedings of the National Academy of Sciences, 2010. **107**(22): p. 10220-10225.
61. Smith, R., *Adeno-associated virus integration: virus versus vector*. Gene therapy, 2008. **15**(11): p. 817-822.
62. Robert, M.A., et al., *Manufacturing of recombinant adeno-associated viruses using mammalian expression platforms*. Biotechnol J, 2017. **12**(3).
63. Wright, J.F., *Manufacturing and characterizing AAV-based vectors for use in clinical studies*. Gene therapy, 2008. **15**(11): p. 840-848.
64. Grieger, J.C. and R.J. Samulski, *Adeno-associated virus vectorology, manufacturing, and clinical applications*. Methods in enzymology, 2012. **507**: p. 229-254.
65. Nass, S.A., et al., *Universal Method for the Purification of Recombinant AAV Vectors of Differing Serotypes*. Mol Ther Methods Clin Dev, 2018. **9**: p. 33-46.
66. Vandenberghe, L.H., et al., *Efficient serotype-dependent release of functional vector into the culture medium during adeno-associated virus manufacturing*. Hum Gene Ther, 2010. **21**(10): p. 1251-7.
67. P, X. and N. Karim M, *Empty Capsids in Production of Viral Vector: Separation and Reassembly*. Journal of Bioengineering & Biomedical Science, 2018. **08**(01).
68. Konecny, P., R.J. Brown, and W.H. Scouten, *Chromatographic purification of immunoglobulin G from bovine milk whey*. Journal of chromatography A, 1994. **673**(1): p. 45-53.
69. Genzel, Y., et al., *Vaccine Production: Upstream Processing with Adherent or Suspension Cell Lines*, in *Animal Cell Biotechnology: Methods and Protocols*, R. Pörtner, Editor. 2014, Humana Press: Totowa, NJ. p. 371-393.
70. Ayuso, E., F. Mingozi, and F. Bosch, *Production, purification and characterization of adeno-associated vectors*. Current gene therapy, 2010. **10**(6): p. 423-436.
71. Robert, M.A., et al., *Manufacturing of recombinant adeno-associated viruses using mammalian expression platforms*. Biotechnology journal, 2017. **12**(3): p. 1600193.
72. Wright, J.F., *Transient transfection methods for clinical adeno-associated viral vector production*. Hum Gene Ther, 2009. **20**(7): p. 698-706.
73. Grimm, D., et al., *Novel tools for production and purification of recombinant adenoassociated virus vectors*. Hum Gene Ther, 1998. **9**(18): p. 2745-60.

74. Rashnonejad, A., et al., *Large-Scale Production of Adeno-Associated Viral Vector Serotype-9 Carrying the Human Survival Motor Neuron Gene*. *Molecular biotechnology*, 2016. **58**(1): p. 30-36.
75. Clément, N. and J.C. Grieger, *Manufacturing of recombinant adeno-associated viral vectors for clinical trials*. *Molecular Therapy-Methods & Clinical Development*, 2016. **3**: p. 16002.
76. Abdulrahman, A. and A. Ghanem, *Recent advances in chromatographic purification of plasmid DNA for gene therapy and DNA vaccines: A review*. *Analytica Chimica Acta*, 2018. **1025**: p. 41-57.
77. Wright, J.F., *Product-Related Impurities in Clinical-Grade Recombinant AAV Vectors: Characterization and Risk Assessment*. *Biomedicines*, 2014. **2**(1): p. 80-97.
78. Strobel, B., et al., *Comparative Analysis of Cesium Chloride- and Iodixanol-Based Purification of Recombinant Adeno-Associated Viral Vectors for Preclinical Applications*. *Hum Gene Ther Methods*, 2015. **26**(4): p. 147-57.
79. Shulgin, I.L. and E. Ruckenstein, *Preferential hydration and solubility of proteins in aqueous solutions of polyethylene glycol*. *Biophys Chem*, 2006. **120**(3): p. 188-98.
80. Alexander, M.R., et al., *Concentration of infectious SARS-CoV-2 by polyethylene glycol precipitation*. *Journal of Virological Methods*, 2020: p. 113977.
81. Morenweiser, R., *Downstream processing of viral vectors and vaccines*. *Gene Therapy*, 2005. **12**: p. S103.
82. Braas, G., et al., *Strategies for the isolation and purification of retroviral vectors for gene therapy*. *Bioseparation*, 1996. **6**(4): p. 211-228.
83. Parsons, D.F., V. Deniz, and B.W. Ninham, *Nonelectrostatic interactions between ions with anisotropic ab initio dynamic polarisabilities*. *Colloids and Surfaces A: Physicochemical and Engineering Aspects*, 2009. **343**(1): p. 57-63.
84. Burova, E. and E. Ioffe, *Chromatographic purification of recombinant adenoviral and adeno-associated viral vectors: methods and implications*. *Gene Ther*, 2005. **12 Suppl 1**: p. S5-17.
85. Moleirinho, M.G., et al., *Baculovirus affinity removal in viral-based bioprocesses*. *Separation and Purification Technology*, 2020. **241**.
86. Dickerson, R., et al., *Separating Empty and Full Recombinant Adeno-Associated Virus Particles Using Isocratic Anion Exchange Chromatography*. *Biotechnology Journal*, 2021. **16**(1): p. 2000015.
87. Sviben, D., et al., *Recovery of infective virus particles in ion-exchange and hydrophobic interaction monolith chromatography is influenced by particle charge and total-to-infective particle ratio*. *J Chromatogr B Analyt Technol Biomed Life Sci*, 2017. **1054**: p. 10-19.
88. Michen, B. and T. Graule, *Isoelectric points of viruses*. *J Appl Microbiol*, 2010. **109**(2): p. 388-97.
89. Brument, N., et al., *A versatile and scalable two-step ion-exchange chromatography process for the purification of recombinant adeno-associated virus serotypes-2 and-5*. *Molecular Therapy*, 2002. **6**(5): p. 678-686.

90. Urabe, M., et al., *Removal of Empty Capsids from Type 1 Adeno-Associated Virus Vector Stocks by Anion-Exchange Chromatography Potentiates Transgene Expression*. *Molecular Therapy*, 2006. **13**(4): p. 823-828.
91. Kaludov, N., B. Handelman, and J.A. Chiorini, *Scalable purification of adeno-associated virus type 2, 4, or 5 using ion-exchange chromatography*. *Hum Gene Ther*, 2002. **13**(10): p. 1235-43.
92. Joshi, P.R.H., et al., *Development of a scalable and robust AEX method for enriched rAAV preparations in genome-containing VCs of serotypes 5, 6, 8, and 9*. *Molecular Therapy - Methods & Clinical Development*, 2021. **21**: p. 341-356.
93. Gagnon P, et al., *Separation of Empty and Full Adeno-Associated Virus Capsids from a Weak Anion Exchanger by Elution with an Ascending pH Gradient at Low Ionic Strength*. *BioProcess Journal*, 2021. **20**.
94. Fu, X., et al., *Analytical Strategies for Quantification of Adeno-Associated Virus Empty Capsids to Support Process Development*. *Human Gene Therapy Methods*, 2019. **30**(4): p. 144-152.
95. Lock, M., M.R. Alvira, and J.M. Wilson, *Analysis of particle content of recombinant adeno-associated virus serotype 8 vectors by ion-exchange chromatography*. *Hum Gene Ther Methods*, 2012. **23**(1): p. 56-64.
96. Venkatakrishnan, B., et al., *Structure and Dynamics of Adeno-Associated Virus Serotype 1 VP1-Unique N-Terminal Domain and Its Role in Capsid Trafficking*. *Journal of Virology*, 2013. **87**(9): p. 4974-4984.
97. Queiroz, J., C. Tomaz, and J. Cabral, *Hydrophobic interaction chromatography of proteins*. *Journal of biotechnology*, 2001. **87**(2): p. 143-159.
98. Mason, T.G., et al., *Predicting Entropic Effects of Water Mixing with Ionic Liquids Containing Anions of Strong Hydrogen Bonding Ability: Role of the Cation*. *The Journal of Physical Chemistry B*, 2020. **124**(41): p. 9182-9194.
99. Haverick, M., et al., *Separation of mAbs molecular variants by analytical hydrophobic interaction chromatography HPLC: overview and applications*. *mAbs*, 2014. **6**(4): p. 852-858.
100. Mirani, M.r. and F. Rahimpour, *Thermodynamic modelling of hydrophobic interaction chromatography of biomolecules in the presence of salt*. *Journal of chromatography. A*, 2015. **1422**: p. 170-177.
101. Zhang, Y. and P.S. Cremer, *Interactions between macromolecules and ions: the Hofmeister series*. *Current opinion in chemical biology*, 2006. **10**(6): p. 658-663.
102. Burova, E. and E. Ioffe, *Chromatographic purification of recombinant adenoviral and adeno-associated viral vectors: methods and implications*. *Gene therapy*, 2005. **12**.
103. Zolotukhin, S., et al., *Recombinant adeno-associated virus purification using novel methods improves infectious titer and yield*. *Gene therapy*, 1999. **6**(6): p. 973.
104. Segura, M., A. Kamen, and A. Garnier, *Purification of Retrovirus Particles Using Heparin Affinity Chromatography*. 2008. p. 1-11.
105. Wang, Q., et al., *Identification of an adeno-associated virus binding epitope for AVB sepharose affinity resin*. *Mol Ther Methods Clin Dev*, 2015. **2**: p. 15040.

106. Smith, R.H., J.R. Levy, and R.M. Kotin, *A simplified baculovirus-AAV expression vector system coupled with one-step affinity purification yields high-titer rAAV stocks from insect cells*. *Molecular Therapy*, 2009. **17**(11): p. 1888-1896.
107. Auricchio, A., et al., *A single-step affinity column for purification of serotype-5 based adeno-associated viral vectors*. *Molecular Therapy*, 2001. **4**(4): p. 372-374.
108. Zhao, M., et al., *Affinity chromatography for vaccines manufacturing: Finally ready for prime time?* *Vaccine*, 2019. **37**(36): p. 5491-5503.
109. Mietzsch, M., et al., *OneBac: platform for scalable and high-titer production of adeno-associated virus serotype 1-12 vectors for gene therapy*. *Hum Gene Ther*, 2014. **25**(3): p. 212-22.
110. Lee, D.-S., B.-M. Kim, and D.-W. Seol, *Improved purification of recombinant adenoviral vector by metal affinity membrane chromatography*. *Biochemical and Biophysical Research Communications*, 2009. **378**(3): p. 640-644.
111. Koerber, J.T., et al., *Engineering adeno-associated virus for one-step purification via immobilized metal affinity chromatography*. *Human gene therapy*, 2007. **18**(4): p. 367-378.
112. Roth, L., M.P. Gotsbacher, and R. Codd, *Immobilized Metal Affinity Chromatography as a Drug Discovery Platform for Metalloenzyme Inhibitors*. *Journal of Medicinal Chemistry*, 2020.
113. Gagnon, P., et al., *Removal of empty capsids from adeno-associated virus preparations by multimodal metal affinity chromatography*. *J Chromatogr A*, 2021. **1649**: p. 462210.
114. Arakawa, T., S. Ponce, and G. Young, *Isoform separation of proteins by mixed-mode chromatography*. *Protein Expression and Purification*, 2015. **116**: p. 144-151.
115. EMBL, *Protein Purification - Extraction and Clarification - Choice of lysis buffer and additives*. 2020.
116. Scheller, C., et al., *Physicochemical properties of SARS-CoV-2 for drug targeting, virus inactivation and attenuation, vaccine formulation and quality control*. *Electrophoresis*, 2020. **41**(13-14): p. 1137-1151.
117. Elbahesh, H., et al., *Novel roles of focal adhesion kinase in cytoplasmic entry and replication of influenza A viruses*. *Journal of virology*, 2014. **88**(12): p. 6714-6728.
118. Duran-Meza, A.L., et al., *Controlling the surface charge of simple viruses*. *PLoS One*, 2021. **16**(9): p. e0255820.
119. Samandoulgou, I., et al., *Stability of Secondary and Tertiary Structures of Virus-Like Particles Representing Noroviruses: Effects of pH, Ionic Strength, and Temperature and Implications for Adhesion to Surfaces*. *Appl Environ Microbiol*, 2015. **81**(22): p. 7680-6.
120. Dika, C., et al., *Isoelectric point is an inadequate descriptor of MS2, Phi X 174 and PRD1 phages adhesion on abiotic surfaces*. *J Colloid Interface Sci*, 2015. **446**: p. 327-34.
121. Zhu, C., et al., *Characterizing hydrophobicity of amino acid side chains in a protein environment via measuring contact angle of a water nanodroplet on*

- planar peptide network*. Proceedings of the National Academy of Sciences, 2016. **113**(46): p. 12946-12951.
122. Frank, H.S. and M.W. Evans, *Free Volume and Entropy in Condensed Systems III. Entropy in Binary Liquid Mixtures; Partial Molal Entropy in Dilute Solutions; Structure and Thermodynamics in Aqueous Electrolytes*. The Journal of Chemical Physics, 1945. **13**(11): p. 507-532.
  123. Haselmeier, R., et al., *Water Dynamics near a Dissolved Noble Gas. First Direct Experimental Evidence for a Retardation Effect*. The Journal of Physical Chemistry, 1995. **99**(8): p. 2243-2246.
  124. Kronberg, B., *The hydrophobic effect*. Current Opinion in Colloid & Interface Science, 2016. **22**: p. 14-22.
  125. Buchanan, P., et al., *Decreased structure on dissolving methane in water*. Chemical Physics Letters, 2005. **415**(1): p. 89-93.
  126. Rezus, Y.L.A. and H.J. Bakker, *Observation of immobilized water molecules around hydrophobic groups*. Phys. Rev. Lett., 2007. **99**: p. 1-4.
  127. Brandeburgo, W.H., et al., *On the slowdown mechanism of water dynamics around small amphiphiles*. Physical Chemistry Chemical Physics, 2015. **17**(38): p. 24968-24977.
  128. Grdadolnik, J., F. Merzel, and F. Avbelj, *Origin of hydrophobicity and enhanced water hydrogen bond strength near purely hydrophobic solutes*. Proc Natl Acad Sci U S A, 2017. **114**(2): p. 322-327.
  129. Lee, B., *The physical origin of the low solubility of nonpolar solutes in water*. Biopolymers, 1985. **24**(5): p. 813-23.
  130. Johnson, S.A., et al., *The step-wise framework to design a chromatography-based hydrophobicity assay for viral particles*. J Chromatogr B Analyt Technol Biomed Life Sci, 2017. **1061-1062**: p. 430-437.
  131. Duckworth, D.H. and P.A. Gulig, *Bacteriophages*. BioDrugs, 2002. **16**(1): p. 57-62.
  132. Dika, C., et al., *Non-DLVO adhesion of F-specific RNA bacteriophages to abiotic surfaces: Importance of surface roughness, hydrophobic and electrostatic interactions*. Colloids and Surfaces A: Physicochemical and Engineering Aspects, 2013. **435**: p. 178-187.
  133. Li, Z.J., et al., *Strong hydrophobicity enables efficient purification of HBc VLPs displaying various antigen epitopes through hydrophobic interaction chromatography*. Biochemical Engineering Journal, 2018. **140**: p. 157-167.
  134. McNally, D.J., et al., *Development and Optimization of a Hydrophobic Interaction Chromatography-Based Method of AAV Harvest, Capture, and Recovery*. Mol Ther Methods Clin Dev, 2020. **19**: p. 275-284.
  135. Samuel L. Penrod, T.M.O., and Stanley B. Grant, *Deposition Kinetics of Two Viruses in Packed Beds of Quartz Granular Media*. Langmuir, 1996. **12**: p. 5576-5587.
  136. Mayer, B.K., et al., *The Impact of Capsid Proteins on Virus Removal and Inactivation During Water Treatment Processes*. Microbiol Insights, 2015. **8**(Suppl 2): p. 15-28.

137. Gerba, C.P. and W.Q. Betancourt, *Viral Aggregation: Impact on Virus Behavior in the Environment*. Environ Sci Technol, 2017. **51**(13): p. 7318-7325.
138. Walker, G.C., *Net charge of trace proteins*. Nature Nanotechnology, 2016. **11**(9): p. 739-740.
139. Armanious, A., et al., *Competitive Coadsorption Dynamics of Viruses and Dissolved Organic Matter to Positively Charged Sorbent Surfaces*. Environmental Science & Technology, 2016. **50**(7): p. 3597-3606.
140. Chrysikopoulos, C.V. and V.I. Syngouna, *Attachment of bacteriophages MS2 and ΦX174 onto kaolinite and montmorillonite: Extended-DLVO interactions*. Colloids and Surfaces B: Biointerfaces, 2012. **92**: p. 74-83.
141. Gentile, G.J., et al., *Electrostatic interactions in virus removal by ultrafiltration membranes*. Journal of Environmental Chemical Engineering, 2018. **6**(1): p. 1314-1321.
142. Walshe, G.E., et al., *Effects of pH, ionic strength, dissolved organic matter, and flow rate on the co-transport of MS2 bacteriophages with kaolinite in gravel aquifer media*. Water Res, 2010. **44**(4): p. 1255-69.
143. Cao, H., F.T.-C. Tsai, and K.A. Rusch, *Salinity and Soluble Organic Matter on Virus Sorption in Sand and Soil Columns*. Groundwater, 2010. **48**(1): p. 42-52.
144. Kelley, M.C., *Chapter 7 - Electric Field Measurement Techniques*, in *The Earth's Electric Field*, M.C. Kelley, Editor. 2014, Elsevier: Boston. p. 187-214.
145. Adair, J.H., E. Suvaci, and J. Sindel, *Surface and Colloid Chemistry*, in *Encyclopedia of Materials: Science and Technology*, K.H.J. Buschow, et al., Editors. 2001, Elsevier: Oxford. p. 1-10.
146. Davidoff, A.M., et al., *Purification of recombinant adeno-associated virus type 8 vectors by ion exchange chromatography generates clinical grade vector stock*. Journal of Virological Methods, 2004. **121**(2): p. 209-215.
147. Baca, M., et al., *A comprehensive study to protein retention in hydrophobic interaction chromatography*. Journal of Chromatography B, 2016. **1032**: p. 182-188.
148. Nejatishahidein, N., et al., *Effectiveness of host cell protein removal using depth filtration with a filter containing diatomaceous earth*. Biotechnology progress, 2020. **36**(6): p. e3028.
149. Fekete, S., et al., *Hydrophobic interaction chromatography for the characterization of monoclonal antibodies and related products*. J Pharm Biomed Anal, 2016. **130**: p. 3-18.
150. Johnson, S., et al., *Characterization of Non-Infectious Virus-Like Particle Surrogates for Viral Clearance Applications*. Appl Biochem Biotechnol, 2017. **183**(1): p. 318-331.
151. Nestola, P., et al., *Improved virus purification processes for vaccines and gene therapy*. Biotechnol Bioeng, 2015. **112**(5): p. 843-57.
152. Iqbal, M., et al., *Aqueous two-phase system (ATPS): an overview and advances in its applications*. Biol Proced Online, 2016. **18**: p. 18.
153. Asenjo, J.A. and B.A. Andrews, *Aqueous two-phase systems for protein separation: A perspective*. Journal of Chromatography A, 2011. **1218**(49): p. 8826-8835.

154. Asenjo, J.A. and B.A. Andrews, *Aqueous two-phase systems for protein separation: Phase separation and applications*. Journal of Chromatography A, 2012. **1238**: p. 1-10.
155. Turpeinen, D.G., et al., *Continuous purification of an enveloped and non-enveloped viral particle using an aqueous two-phase system*. Separation and Purification Technology, 2021. **269**.
156. Joshi, P.U., et al., *Tie line framework to optimize non-enveloped virus recovery in aqueous two-phase systems*. Journal of Chromatography B, 2019. **1126-1127**: p. 121744.
157. Zafarani-Moattar, M.T., S. Hamzehzadeh, and S. Nasiri, *A new aqueous biphasic system containing polypropylene glycol and a water-miscible ionic liquid*. Biotechnology Progress, 2012. **28**.
158. Mi, X., et al., *Virus isoelectric point determination using single-particle chemical force microscopy*. Langmuir, 2019. **36**(1): p. 370-378.
159. Andrews, B.A., A.S. Schmidt, and J.A. Asenjo, *Correlation for the partition behavior of proteins in aqueous two-phase systems: effect of surface hydrophobicity and charge*. Biotechnol Bioeng, 2005. **90**(3): p. 380-90.
160. Grilo, A.L., M. Raquel Aires-Barros, and A.M. Azevedo, *Partitioning in Aqueous Two-Phase Systems: Fundamentals, Applications and Trends*. Separation & Purification Reviews, 2016. **45**(1): p. 68-80.
161. Rogers, R.D. and M.A. Eiteman, *Aqueous biphasic separations*. 1995: Springer.
162. Hao, X., et al., *Separation and purification of enveloped and non-enveloped viruses from water samples using an aqueous two-phase system*. Process Biochemistry, 2022. **119**: p. 58-67.
163. Choi, H.J., et al., *Effect of Osmotic Pressure on the Stability of Whole Inactivated Influenza Vaccine for Coating on Microneedles*. PLoS One, 2015. **10**(7): p. e0134431.
164. Pergande, M.R. and S.M. Cologna, *Isoelectric Point Separations of Peptides and Proteins*. Proteomes, 2017. **5**(1).
165. Hühner, J., M. Lämmerhofer, and C. Neusüß, *Capillary isoelectric focusing-mass spectrometry: Coupling strategies and applications*. Electrophoresis, 2015. **36**(21-22): p. 2670-2686.
166. Jiang, Y., et al., *Modification in Silver Staining Procedure for Enhanced Protein Staining*. BioMed Research International, 2022. **2022**: p. 6243971.
167. Braun, M., et al., *A simple method to estimate the isoelectric point of modified Tomato bushy stunt virus (TBSV) particles*. ELECTROPHORESIS, 2017. **38**(21): p. 2771-2776.
168. Thomassen, Y.E., et al., *Isoelectric Point Determination of Live Polioviruses by Capillary Isoelectric Focusing with Whole Column Imaging Detection*. Analytical Chemistry, 2013. **85**(12): p. 6089-6094.
169. Leuchs, B., et al., *A novel scalable, robust downstream process for oncolytic rat parvovirus: isoelectric point-based elimination of empty particles*. Appl Microbiol Biotechnol, 2017. **101**(8): p. 3143-3152.
170. Brorson, K., et al., *Characterization and purification of bacteriophages using chromatofocusing*. Journal of Chromatography A, 2008. **1207**(1): p. 110-121.

171. James, A.M., *Electrophoresis of Particles in Suspension*, in *Surface and Colloid Science: Volume 11: Experimental Methods*, R.J. Good and R.R. Stromberg, Editors. 1979, Springer US: Boston, MA. p. 121-185.
172. Sluyterman, L.A.A.E. and O. Elgersma, *Chromatofocusing: Isoelectric focusing on ion-exchange columns: I. General Principles*. *Journal of Chromatography A*, 1978. **150**(1): p. 17-30.
173. Shan, L. and D.J. Anderson, *Gradient Chromatofocusing. Versatile pH Gradient Separation of Proteins in Ion-Exchange HPLC: Characterization Studies*. *Analytical Chemistry*, 2002. **74**(21): p. 5641-5649.
174. Leisi, R., et al., *Impact of the isoelectric point of model parvoviruses on viral retention in anion-exchange chromatography*. *Biotechnology and Bioengineering*, 2021. **118**(1): p. 116-129.
175. Baek, J., et al., *New Insights into the Chromatography Mechanisms of Ion-Exchange Charge Variant Analysis: Dispelling Myths and Providing Guidance for Robust Method Optimization*. *Analytical Chemistry*, 2020. **92**(19): p. 13411-13419.
176. Xiao, Y. and M.R. Wiesner, *Characterization of surface hydrophobicity of engineered nanoparticles*. *J Hazard Mater*, 2012. **215-216**: p. 146-51.
177. Tehrani-Bagha, A.R. and K. Holmberg, *Solubilization of Hydrophobic Dyes in Surfactant Solutions*. *Materials (Basel)*, 2013. **6**(2): p. 580-608.
178. Li, G., K.K.H.Y. Ho, and Y.Y. Zuo, *Relative Dye Adsorption Method for Determining the Hydrophobicity of Nanoparticles*. *The Journal of Physical Chemistry C*, 2022. **126**(1): p. 832-837.
179. Ambalam, P., et al., *Bile stimulates cell surface hydrophobicity, Congo red binding and biofilm formation of Lactobacillus strains*. *FEMS Microbiol Lett*, 2012. **333**(1): p. 10-9.
180. Guliyeva, A.J. and O.K. Gasymov, *ANS fluorescence: Potential to discriminate hydrophobic sites of proteins in solid states*. *Biochemistry and Biophysics Reports*, 2020. **24**: p. 100843.
181. Lee, J.-E., et al., *Mapping Surface Hydrophobicity of  $\alpha$ -Synuclein Oligomers at the Nanoscale*. *Nano Letters*, 2018. **18**(12): p. 7494-7501.
182. Crandon, L.E., et al., *Adaptive methodology to determine hydrophobicity of nanomaterials in situ*. *PLoS One*, 2020. **15**(6): p. e0233844.
183. Tubio, G., B. Nerli, and G. Picó, *Relationship between the protein surface hydrophobicity and its partitioning behaviour in aqueous two-phase systems of polyethyleneglycol–dextran*. *Journal of Chromatography B*, 2004. **799**(2): p. 293-301.
184. Holm, J., A.J. Lawaetz, and S.I. Hansen, *Ligand binding induces a sharp decrease in hydrophobicity of folate binding protein assessed by 1-anilinonaphthalene-8-sulphonate which suppresses self-association of the hydrophobic apo-protein*. *Biochemical and Biophysical Research Communications*, 2012. **425**(1): p. 19-24.
185. Dorh, N., et al., *BODIPY-Based Fluorescent Probes for Sensing Protein Surface-Hydrophobicity*. *Scientific Reports*, 2015. **5**.

186. Cao, Y., J. Zhao, and Y.L. Xiong, *Coomassie Brilliant Blue-binding: a simple and effective method for the determination of water-insoluble protein surface hydrophobicity*. Analytical Methods, 2016. **8**(4): p. 790-795.
187. Georgiou, C.D., et al., *Mechanism of Coomassie brilliant blue G-250 binding to proteins: a hydrophobic assay for nanogram quantities of proteins*. Analytical and Bioanalytical Chemistry, 2008. **391**(1): p. 391-403.
188. Compton, S.J. and C.G. Jones, *Mechanism of dye response and interference in the Bradford protein assay*. Analytical Biochemistry, 1985. **151**(2): p. 369-374.
189. Adhikari, S., et al., *Kinetics and mechanism of dye adsorption on WO<sub>3</sub> nanoparticles*. Applied Surface Science, 2017. **420**: p. 472-482.
190. Talbot, D., et al., *Adsorption of Organic Dyes on Magnetic Iron Oxide Nanoparticles. Part I: Mechanisms and Adsorption-Induced Nanoparticle Agglomeration*. ACS Omega, 2021. **6**(29): p. 19086-19098.
191. Sahu, O. and N. Singh, *13 - Significance of bioadsorption process on textile industry wastewater*, in *The Impact and Prospects of Green Chemistry for Textile Technology*, I. Shahid ul and B.S. Butola, Editors. 2019, Woodhead Publishing. p. 367-416.
192. Singh, A.K., *Chapter 7 - Mechanisms of Nanoparticle Toxicity*, in *Engineered Nanoparticles*, A.K. Singh, Editor. 2016, Academic Press: Boston. p. 295-341.
193. Mu, T.-H. and H.-N. Sun, *Chapter 22 - Sweet Potato Leaf Polyphenols: Preparation, Individual Phenolic Compound Composition and Antioxidant Activity*, in *Polyphenols in Plants (Second Edition)*, R.R. Watson, Editor. 2019, Academic Press. p. 365-380.
194. Mi, X. and C.L. Heldt, *Adsorption of a non-enveloped mammalian virus to functionalized nanofibers*. Colloids Surf B Biointerfaces, 2014. **121**: p. 319-24.
195. Ayawei, N., et al., *Synthesis, characterization and application of Mg/Al layered double hydroxide for the degradation of congo red in aqueous solution*. Open Journal of Physical Chemistry, 2015. **5**(03): p. 56.
196. Singh, A.K., *Chapter 8 - Nanoparticle Ecotoxicology*, in *Engineered Nanoparticles*, A.K. Singh, Editor. 2016, Academic Press: Boston. p. 343-450.
197. Noy, A., *Chemical force microscopy of chemical and biological interactions*. Bio Surface and Interface Analysis, 2006. **38**(11): p. 1429-1441.
198. Binnig, G., C.F. Quate, and C. Gerber, *Atomic force microscope*. Phys Rev Lett, 1986. **56**(9): p. 930-933.
199. Gan, C., et al., *Imaging and force measurement of LDL and HDL by AFM in air and liquid*. FEBS Open Bio, 2015. **5**: p. 276-282.
200. Mi, X. and C.L. Heldt, *Single-particle chemical force microscopy to characterize virus surface chemistry*. BioTechniques, 2020. **69**(5): p. 363-370.
201. Lübbecke, J., et al., *Measurement and modelling of non-contact atomic force microscope cantilever properties from ultra-high vacuum to normal pressure conditions*. Measurement Science and Technology, 2011. **22**(5): p. 055501.
202. Meusel, M., et al., *Time- and Temperature-Dependent Growth Behavior of Ionic Liquids on Au(111) Studied by Atomic Force Microscopy in Ultrahigh Vacuum*. The Journal of Physical Chemistry C, 2021. **125**(37): p. 20439-20449.

203. Guo, S., et al., *Measuring protein isoelectric points by AFM-based force spectroscopy using trace amounts of sample*. Nat Nanotechnol, 2016. **11**(9): p. 817-23.
204. Areo, O., et al., *Single-Particle Characterization of SARS-CoV-2 Isoelectric Point and Comparison to Variants of Interest*. Microorganisms, 2021. **9**(8).
205. Geisse, N.A., *AFM and combined optical techniques*. Materials Today, 2009. **12**(7): p. 40-45.
206. Dufrene, Y.F., *Atomic force microscopy and chemical force microscopy of microbial cells*. Nat Protoc, 2008. **3**(7): p. 1132-8.
207. Shah, B., V.K. Kakumanu, and A.K. Bansal, *Analytical techniques for quantification of amorphous/crystalline phases in pharmaceutical solids*. Journal of Pharmaceutical Sciences, 2006. **95**(8): p. 1641-1665.
208. Uchihashi, T., et al., *Quantitative force measurements in liquid using frequency modulation atomic force microscopy*. Applied Physics Letters, 2004. **85**(16): p. 3575-3577.
209. Marti, O., *Measurement of Adhesion and Pull-Off Forces with the AFM*. 2000.
210. Rouso, I. and A. Deshpande, *Applications of Atomic Force Microscopy in HIV-1 Research*. Viruses, 2022. **14**(3): p. 648.
211. Bhushan, B. and S. Sundararajan, *Micro/nanoscale friction and wear mechanisms of thin films using atomic force and friction force microscopy*. Acta Materialia, 1998. **46**(11): p. 3793-3804.
212. Le Grimellec, C., et al., *Imaging of the Surface of Living Cells by Low-Force Contact-Mode Atomic Force Microscopy*. Biophysical Journal, 1998. **75**(2): p. 695-703.
213. De, T., et al., *Immobilization method of yeast cells for intermittent contact mode imaging using the atomic force microscope*. Ultramicroscopy, 2010. **110**(3): p. 254-258.
214. Yamashita, H., et al., *Role of trimer-trimer interaction of bacteriorhodopsin studied by optical spectroscopy and high-speed atomic force microscopy*. Journal of Structural Biology, 2013. **184**(1): p. 2-11.
215. Ando, T., T. Uchihashi, and T. Fukuma, *High-speed atomic force microscopy for nano-visualization of dynamic biomolecular processes*. Progress in Surface Science, 2008. **83**(7): p. 337-437.
216. Maver, U., et al., *Recent progressive use of atomic force microscopy in biomedical applications*. TrAC Trends in Analytical Chemistry, 2016. **80**: p. 96-111.
217. Seifert, J., et al., *Comparison of Atomic Force Microscopy and Scanning Ion Conductance Microscopy for Live Cell Imaging*. Langmuir, 2015. **31**(24): p. 6807-6813.
218. Braet, F. and E. Wisse, *AFM imaging of fenestrated liver sinusoidal endothelial cells*. Micron, 2012. **43**(12): p. 1252-1258.
219. Parrat, D., et al., *Imaging modes in atomic-force microscopy*. Journal of Trace and Microprobe Techniques, 1995. **13**(3): p. 343-352.

220. Xu, K., et al., *Recent development of PeakForce Tapping mode atomic force microscopy and its applications on nanoscience*. Nanotechnology Reviews, 2018. **7**(6): p. 605-621.
221. Albrecht, T.R., et al., *Frequency modulation detection using high-Q cantilevers for enhanced force microscope sensitivity*. Journal of applied physics, 1991. **69**(2): p. 668-673.
222. Medalsy, I., U. Hensen, and D.J. Muller, *Imaging and quantifying chemical and physical properties of native proteins at molecular resolution by force-volume AFM*. Angewandte Chemie International Edition, 2011. **50**(50): p. 12103-12108.
223. Ha, C.-S. and J.A. Gardella, *Surface Chemistry of Biodegradable Polymers for Drug Delivery Systems*. Chemical Reviews, 2005. **105**(11): p. 4205-4232.
224. Weymouth, A.J., T. Hofmann, and F.J. Giessibl, *Quantifying Molecular Stiffness and Interaction with Lateral Force Microscopy*. Science, 2014. **343**(6175): p. 1120-1122.
225. Guz, N., et al., *If cell mechanics can be described by elastic modulus: study of different models and probes used in indentation experiments*. Biophysical journal, 2014. **107**(3): p. 564-575.
226. Fakhru'llina, G., et al., *Nanoscale imaging and characterization of Caenorhabditis elegans epicuticle using atomic force microscopy*. Nanomedicine: Nanotechnology, Biology and Medicine, 2017. **13**(2): p. 483-491.
227. Kaimaki, D.-M., B.E. Smith, and C. Durkan, *On the use of nanomechanical atomic force microscopy to characterise oil-exposed surfaces*. RSC advances, 2018. **8**(12): p. 6680-6689.
228. Marti, O., M. Holzwarth, and M. Beil, *Measuring the nanomechanical properties of cancer cells by digital pulsed force mode imaging*. Nanotechnology, 2008. **19**(38): p. 384015.
229. Beckwitt, E.C., et al., *Peakforce tapping AFM reveals that human XPA binds to DNA damage as a monomer producing a 60 bend*. Biophysical Journal, 2018. **114**(3): p. 93a.
230. Al Faouri, R., et al., *Adhesive force between graphene nanoscale flakes and living biological cells*. Journal of Applied Toxicology, 2017. **37**(11): p. 1346-1353.
231. Dufrene, Y.F., et al., *Multiparametric imaging of biological systems by force-distance curve-based AFM*. Nat Methods, 2013. **10**(9): p. 847-54.
232. Cappella, B. and G. Dietler, *Force-distance curves by atomic force microscopy*. Surface Science Reports, 1999. **34**(1): p. 1-104.
233. Liashkovich, I., G. Rosso, and V. Shahin, *Atomic Force Microscopy for Structural and Biophysical Investigations on Nuclear Pore Complexes*, in *The Nuclear Pore Complex: Methods and Protocols*, M.W. Goldberg, Editor. 2022, Springer US: New York, NY. p. 299-310.
234. Leite, F., L. Mattoso, and O. Oliveira, *The Atomic Force Spectroscopy as a Tool to Investigate Surface Forces: Basic Principles and Applications*, ed. by A. 2007.
235. Hutter, J.L. and J. Bechhoefer, *Calibration of atomic-force microscope tips*. Review of scientific instruments, 1993. **64**(7): p. 1868-1873.

236. Moretti, M., et al., *AFM characterization of biomolecules in physiological environment by an advanced nanofabricated probe*. *Microscopy Research and Technique*, 2012. **75**(12): p. 1723-1731.
237. Shi, X., et al., *Living cell study at the single-molecule and single-cell levels by atomic force microscopy*. *Nanomedicine*, 2012. **7**(10): p. 1625-1637.
238. Prasad, B.V.V. and M.F. Schmid, *Principles of Virus Structural Organization*, in *Viral Molecular Machines*, M.G. Rossmann and V.B. Rao, Editors. 2012, Springer US: Boston, MA. p. 17-47.
239. Phillips, R. and S.R. Quake, *The Biological Frontier of Physics*. *Physics Today*, 2006. **59**(9): p. 38-43.
240. Dragnea, B., *Viruses: A Physical Chemistry Perspective*. *J Phys Chem B*, 2022. **126**(24): p. 4411-4414.
241. Rahmati, M., et al., *Biological responses to physicochemical properties of biomaterial surface*. *Chem Soc Rev*, 2020. **49**(15): p. 5178-5224.
242. Ryu, W.S., *Virus Life Cycle*. *Molecular Virology of Human Pathogenic Viruses*. 2017:31-45. doi: 10.1016/B978-0-12-800838-6.00003-5. Epub 2016 May 6.
243. Byk, L.A. and A.V. Gamarnik, *Properties and Functions of the Dengue Virus Capsid Protein*. *Annual Review of Virology*, 2016. **3**(1): p. 263-281.
244. Patel, A.J. and S. Garde, *Efficient method to characterize the context-dependent hydrophobicity of proteins*. *J Phys Chem B*, 2014. **118**(6): p. 1564-73.
245. Lum, K., D. Chandler, and J.D. Weeks, *Hydrophobicity at Small and Large Length Scales*. *The Journal of Physical Chemistry B*, 1999. **103**(22): p. 4570-4577.
246. Godawat, R., S.N. Jamadagni, and S. Garde, *Characterizing hydrophobicity of interfaces by using cavity formation, solute binding, and water correlations*. *Proc Natl Acad Sci U S A*, 2009. **106**(36): p. 15119-24.
247. Hoffmann, W., et al., *An Intrinsic Hydrophobicity Scale for Amino Acids and Its Application to Fluorinated Compounds*. *Angewandte Chemie International Edition*, 2019. **58**(24): p. 8216-8220.
248. Chong, S.H. and S. Ham, *Site-directed analysis on protein hydrophobicity*. *J Comput Chem*, 2014. **35**(18): p. 1364-70.
249. Bastos-González, D., et al., *Ions at interfaces: the central role of hydration and hydrophobicity*. *Current Opinion in Colloid & Interface Science*, 2016. **23**: p. 19-28.
250. Carstensen, H., B.W. Müller, and R.H. Müller, *Adsorption of ethoxylated surfactants on nanoparticles. I. Characterization by hydrophobic interaction chromatography*. *International Journal of Pharmaceutics*, 1991. **67**(1): p. 29-37.
251. Jones, M.C., et al., *Quantitative assessment of nanoparticle surface hydrophobicity and its influence on pulmonary biocompatibility*. *J Control Release*, 2014. **183**: p. 94-104.
252. Bolognesi, B., et al., *ANS binding reveals common features of cytotoxic amyloid species*. *ACS Chem Biol*, 2010. **5**(8): p. 735-40.
253. Wang, H. and P.K. Chu, *Chapter 4 - Surface Characterization of Biomaterials*, in *Characterization of Biomaterials*, A. Bandyopadhyay and S. Bose, Editors. 2013, Academic Press: Oxford. p. 105-174.

254. Dufrene, Y.F., et al., *Imaging modes of atomic force microscopy for application in molecular and cell biology*. Nat Nanotechnol, 2017. **12**(4): p. 295-307.
255. Alsteens, D., et al., *Multiparametric atomic force microscopy imaging of single bacteriophages extruding from living bacteria*. Nat Commun, 2013. **4**: p. 2926.
256. Krieg, M., et al., *Atomic force microscopy-based mechanobiology*. Nature Reviews Physics, 2019. **1**(1): p. 41-57.
257. Adeniba, O.O., et al., *Simultaneous time-varying viscosity, elasticity, and mass measurements of single adherent cancer cells across cell cycle*. Scientific Reports, 2020. **10**(1): p. 12803.
258. Aleksandr Noy, a. Dmitri V. Vezenov, and C.M. Lieber, *Chemical Force Microscopy*. Annual Review of Materials Science, 1997. **27**(1): p. 381-421.
259. Frisbie, C.D., et al., *Functional group imaging by chemical force microscopy*. Science, 1994. **265**(5181): p. 2071-2074.
260. Lal, R. and M.F. Arnsdorf, *Multidimensional atomic force microscopy for drug discovery: A versatile tool for defining targets, designing therapeutics and monitoring their efficacy*. Life sciences, 2010. **86**(15-16): p. 545-562.
261. Heldt, C.L., et al., *A colorimetric assay for viral agents that produce cytopathic effects*. Journal of Virological Methods, 2006. **135**(1): p. 56-65.
262. Almeida, A., et al., *Chromatographic capture of cells to achieve single stage clarification in recombinant protein purification*. Biotechnology Progress, 2022. **38**(2): p. e3227.
263. Metzger, K.F.J., et al., *Adsorptive filtration: A case study for early impurity reduction in an Escherichia coli production process*. Biotechnology Progress, 2020. **36**(3): p. e2948.
264. Simpson, A.A., et al., *The structure of porcine parvovirus: comparison with related viruses*. J Mol Biol, 2002. **315**(5): p. 1189-98.
265. Ren, X., et al., *Phylogeny and evolution of porcine parvovirus*. Virus Res, 2013. **178**(2): p. 392-7.
266. Streck, A.F., C.W. Canal, and U. Truyen, *Molecular epidemiology and evolution of porcine parvoviruses*. Infection, Genetics and Evolution, 2015. **36**: p. 300-306.
267. Banerjee, N. and S. Mukhopadhyay, *Viral glycoproteins: biological role and application in diagnosis*. VirusDisease, 2016. **27**(1): p. 1-11.
268. Rey, F.A., et al., *The envelope glycoprotein from tick-borne encephalitis virus at 2 Å resolution*. Nature, 1995. **375**(6529): p. 291-8.
269. Callens, N., et al., *Morphology and Molecular Composition of Purified Bovine Viral Diarrhea Virus Envelope*. PLoS Pathog, 2016. **12**(3): p. e1005476.
270. Newcomer, B.W., M.F. Chamorro, and P.H. Walz, *Vaccination of cattle against bovine viral diarrhea virus*. Veterinary Microbiology, 2017. **206**: p. 78-83.
271. Ingraham, R.H., *Hydrophobic interaction chromatography of proteins*, in *High-Performance Liquid Chromatography of Peptides and Proteins: Separation, Analysis, and Conformation*. 2017, CRC Press. p. 425-435.
272. Tomaz, C.T., *Chapter 7 - Hydrophobic interaction chromatography\**, in *Liquid Chromatography (Second Edition)*, S. Fanali, et al., Editors. 2017, Elsevier. p. 171-190.

273. Shimizu, S. and D.J. Smith, *Preferential hydration and the exclusion of cosolvents from protein surfaces*. The Journal of Chemical Physics, 2004. **121**(2): p. 1148-1154.
274. Moelbert, S., B. Normand, and P. De Los Rios, *Kosmotropes and chaotropes: modelling preferential exclusion, binding and aggregate stability*. Biophys Chem, 2004. **112**(1): p. 45-57.
275. Bhat, R. and S.N. Timasheff, *Steric exclusion is the principal source of the preferential hydration of proteins in the presence of polyethylene glycols*. Protein Science, 1992. **1**(9): p. 1133-1143.
276. Zaccai, G., et al., *Neutrons describe ectoine effects on water H-bonding and hydration around a soluble protein and a cell membrane*. Scientific reports, 2016. **6**(1): p. 1-12.
277. Rego, N.B., E. Xi, and A.J. Patel, *Identifying hydrophobic protein patches to inform protein interaction interfaces*. Proc Natl Acad Sci U S A, 2021. **118**(6).
278. Chong, Y., et al., *Dominant Alcohol-Protein Interaction via Hydration-Enabled Enthalpy-Driven Binding Mechanism*. J Phys Chem B, 2015. **119**(17): p. 5367-75.
279. Yoshikawa, H., et al., *Mechanistic insights into protein precipitation by alcohol*. International journal of biological macromolecules, 2012. **50**(3): p. 865-871.
280. Johansson, K., et al., *Combined effects of potassium chloride and ethanol as mobile phase modulators on hydrophobic interaction and reversed-phase chromatography of three insulin variants*. Journal of Chromatography A, 2015. **1381**: p. 64-73.
281. Patra, M., et al., *Under the influence of alcohol: the effect of ethanol and methanol on lipid bilayers*. Biophys J, 2006. **90**(4): p. 1121-35.
282. Ballal, D. and W.G. Chapman, *Hydrophobic and hydrophilic interactions in aqueous mixtures of alcohols at a hydrophobic surface*. J Chem Phys, 2013. **139**(11): p. 114706.
283. Jennissen, H.P., *Hydrophobic interaction chromatography: harnessing multivalent protein-surface interactions for purification procedures*. Methods in molecular biology (Clifton, NJ), 2005. **305**: p. 81-99.
284. Peralta, C., et al., *The combination of ischemic preconditioning and liver Bcl-2 overexpression is a suitable strategy to prevent liver and lung damage after hepatic ischemia-reperfusion*. Am J Pathol, 2002. **160**(6): p. 2111-22.
285. Eriksson, K.O., *Hydrophobic interaction chromatography*, in *Biopharmaceutical Processing*. 2018, Elsevier. p. 401-408.
286. Al-Ghouti, M.A. and D.A. Da'ana, *Guidelines for the use and interpretation of adsorption isotherm models: A review*. Journal of Hazardous Materials, 2020. **393**: p. 122383.
287. Dill, K.A., et al., *Modeling water, the hydrophobic effect, and ion solvation*. Annu Rev Biophys Biomol Struct, 2005. **34**: p. 173-99.
288. Bolen, D.W. and I.V. Baskakov, *The osmophobic effect: natural selection of a thermodynamic force in protein folding* | Edited by D. Draper. Journal of Molecular Biology, 2001. **310**(5): p. 955-963.

289. Nagaraja, V.H. and R. Iyyaswami, *Aqueous two phase partitioning of fish proteins: partitioning studies and ATPS evaluation*. J Food Sci Technol, 2015. **52**(6): p. 3539-48.
290. van der Vegt, N.F.A. and D. Nayar, *The Hydrophobic Effect and the Role of Cosolvents*. J Phys Chem B, 2017. **121**(43): p. 9986-9998.
291. He, S., et al., *DNA precipitation revisited: A quantitative analysis*. Nano Select, 2021. **3**(3): p. 617-626.
292. Dos Santos, R., A.L. Carvalho, and A.C.A. Roque, *Renaissance of protein crystallization and precipitation in biopharmaceuticals purification*. Biotechnology Advances, 2017. **35**(1): p. 41-50.
293. Zeng, X., et al., *Effects of deproteinization methods on primary structure and antioxidant activity of Ganoderma lucidum polysaccharides*. International journal of biological macromolecules, 2019. **126**: p. 867-876.
294. Samaranch, L., et al., *Adeno-associated viral vector serotype 9-based gene therapy for Niemann-Pick disease type A*. Sci Transl Med, 2019. **11**(506).
295. Hampson, D., A. Hooper, and Y. Niibori, *The Application of Adeno-Associated Viral Vector Gene Therapy to the Treatment of Fragile X Syndrome*. Brain Sciences, 2019. **9**(2).
296. Hejmowski, A.L., et al., *Novel anion exchange membrane chromatography method for the separation of empty and full adeno-associated virus*. Biotechnol J, 2022. **17**(2): p. e2100219.
297. Medicine, U.S.N.L.o. *Clinical Trials*. [cited 2022 October 26]; Available from: <https://clinicaltrials.gov/>.
298. Au, H.K.E., M. Isalan, and M. Mielcarek, *Gene Therapy Advances: A Meta-Analysis of AAV Usage in Clinical Settings*. Front Med (Lausanne), 2021. **8**: p. 809118.
299. Patel, D.H. and A. Misra, *5 - Gene Delivery Using Viral Vectors*, in *Challenges in Delivery of Therapeutic Genomics and Proteomics*, A. Misra, Editor. 2011, Elsevier: London. p. 207-270.
300. Ling, C., et al., *The adeno-associated virus genome packaging puzzle*. Journal of molecular and genetic medicine: an international journal of biomedical research, 2015. **9**(3).
301. Mietzsch, M., et al., *Improved Genome Packaging Efficiency of Adeno-associated Virus Vectors Using Rep Hybrids*. Journal of Virology, 2021. **95**(19): p. e00773-21.
302. King, J.A., et al., *DNA helicase-mediated packaging of adeno-associated virus type 2 genomes into preformed capsids*. The EMBO journal, 2001. **20**(12): p. 3282-3291.
303. Flotte, T.R., *Empty Adeno-Associated Virus Capsids: Contaminant or Natural Decoy?* Human Gene Therapy, 2017. **28**(2): p. 147-148.
304. Mingozzi, F., et al., *CD8+ T-cell responses to adeno-associated virus capsid in humans*. Nature Medicine, 2007. **13**(4): p. 419-422.
305. Manno, C.S., et al., *Successful transduction of liver in hemophilia by AAV-Factor IX and limitations imposed by the host immune response*. Nature Medicine, 2006. **12**(3): p. 342-347.

306. Gao, K., et al., *Empty virions in AAV8 vector preparations reduce transduction efficiency and may cause total viral particle dose-limiting side effects*. *Molecular Therapy-Methods & Clinical Development*, 2014. **1**: p. 9.
307. Qu, G., et al., *Separation of adeno-associated virus type 2 empty particles from genome containing vectors by anion-exchange column chromatography*. *Journal of virological methods*, 2007. **140**(1-2): p. 183-192.
308. Wright, J.F., *AAV empty capsids: for better or for worse?* *Molecular Therapy*, 2014. **22**(1): p. 1-2.
309. Crosson, S.M., et al., *Helper-free Production of Laboratory Grade AAV and Purification by Iodixanol Density Gradient Centrifugation*. *Mol Ther Methods Clin Dev*, 2018. **10**: p. 1-7.
310. Chen, Y.H., M.S. Keiser, and B.L. Davidson, *Adeno-Associated Virus Production, Purification, and Titering*. *Current Protocols in Mouse Biology*, 2018. **8**(4): p. e56.
311. Allay, J.A., et al., *Good manufacturing practice production of self-complementary serotype 8 adeno-associated viral vector for a hemophilia B clinical trial*. *Human gene therapy*, 2011. **22**(5): p. 595-604.
312. Joshi, P.R., et al., *Development and Validation of an Anion Exchange High-Performance Liquid Chromatography Method for Analysis of Empty Capsids and Capsids Encapsidating Genetic Material in a Purified Preparation of Recombinant Adeno-Associated Virus Serotype 5*. *Human Gene Therapy*, 2021. **32**(21-22): p. 1390-1402.
313. Moskalenko, M., et al., *Epitope mapping of human anti-adeno-associated virus type 2 neutralizing antibodies: implications for gene therapy and virus structure*. *Journal of virology*, 2000. **74**(4): p. 1761-1766.
314. Pacouret, S., et al., *AAV-ID: A Rapid and Robust Assay for Batch-to-Batch Consistency Evaluation of AAV Preparations*. *Molecular Therapy*, 2017. **25**(6): p. 1375-1386.
315. Khatwani, S.L., A. Pavlova, and Z. Pirot, *Anion-exchange HPLC assay for separation and quantification of empty and full capsids in multiple adeno-associated virus serotypes*. *Mol Ther Methods Clin Dev*, 2021. **21**: p. 548-558.
316. Mi, X., et al., *Virus Isoelectric Point Determination Using Single-Particle Chemical Force Microscopy*. *Langmuir*, 2020. **36**: p. 370-378.
317. Werle, A.K., et al., *Comparison of analytical techniques to quantitate the capsid content of adeno-associated viral vectors*. *Molecular Therapy - Methods & Clinical Development*, 2021. **23**: p. 254-262.
318. Gagnon, P., et al., *Multiple-Monitor HPLC Assays for Rapid Process Development, In-Process Monitoring, and Validation of AAV Production and Purification*. *Pharmaceutics*, 2021. **13**(1).
319. Lins-Austin, B., et al., *Adeno-Associated Virus (AAV) Capsid Stability and Liposome Remodeling During Endo/Lysosomal pH Trafficking*. *Viruses*, 2020. **12**(6).
320. Penzes, J.J., et al., *Adeno-associated Virus 9 Structural Rearrangements Induced by Endosomal Trafficking pH and Glycan Attachment*. *Journal of Virology*, 2021. **95**(19): p. e00843-21.

321. Rieman III, W., *Salting-out chromatography: A review*. Journal of Chemical Education, 1961. **38**(7): p. 338.
322. Sanemasa, I., M. Nakahara, and J.-Z. Zheng, *Uptake of alkanes and alcohols by ion-exchange resins in aqueous solution*. Analytical sciences, 2003. **19**(6): p. 949-951.
323. Nesterenko, P.N. and E.P. Nesterenko, *Hydrophobicity of polymer based anion-exchange columns for ion chromatography*. Heliyon, 2021. **7**(6): p. e07290.
324. Dickerson, R., et al., *Separating Empty and Full Recombinant Adeno-Associated Virus Particles Using Isocratic Anion Exchange Chromatography*. Biotechnol J, 2021. **16**(1): p. e2000015.
325. Anastassopoulou, J. and T. Theophanides, *Magnesium-DNA interactions and the possible relation of magnesium to carcinogenesis. Irradiation and free radicals*. Critical Reviews in Oncology Hematology, 2002. **42**: p. 79-91.
326. Aboubakr, H.A., T.A. Sharafeldin, and S.M. Goyal, *Stability of SARS-CoV-2 and other coronaviruses in the environment and on common touch surfaces and the influence of climatic conditions: A review*. Transbound Emerg Dis, 2020.
327. Joonaki, E., et al., *Surface Chemistry Can Unlock Drivers of Surface Stability of SARS-CoV-2 in a Variety of Environmental Conditions*. Chem, 2020. **6**(9): p. 2135-2146.
328. Vega, E., J. Garland, and S.D. Pillai, *Electrostatic forces control nonspecific virus attachment to lettuce*. Journal of food protection, 2008. **71**(3): p. 522-529.
329. van Oss, C.J., *Acid—base interfacial interactions in aqueous media*. Colloids and Surfaces A: Physicochemical and Engineering Aspects, 1993. **78**: p. 1-49.
330. Dang, H.T.T. and V.V. Tarabara, *Virus deposition onto polyelectrolyte-coated surfaces: A study with bacteriophage MS2*. Journal of Colloid and Interface Science, 2019. **540**: p. 155-166.
331. Boone, S.A. and C.P. Gerba, *Significance of fomites in the spread of respiratory and enteric viral disease*. Applied and environmental microbiology, 2007. **73**(6): p. 1687-1696.
332. Bhattacharjee, S., *DLS and zeta potential - What they are and what they are not?* J Control Release, 2016. **235**: p. 337-351.
333. Samandougou, I., I. Fliss, and J. Jean, *Zeta Potential and Aggregation of Virus-Like Particle of Human Norovirus and Feline Calicivirus Under Different Physicochemical Conditions*. Food and Environmental Virology, 2015. **7**(3): p. 249-260.
334. Heffron, J. and B.K. Mayer, *Improved Virus Isoelectric Point Estimation by Exclusion of Known and Predicted Genome-Binding Regions*. Appl Environ Microbiol, 2020. **86**(23).
335. Krebs, F., et al., *Isoelectric point determination by imaged CIEF of commercially available SARS-CoV-2 proteins and the hACE2 receptor*. Electrophoresis, 2021. **42**(6): p. 687-692.
336. Hristova, S.H. and A.M. Zhivkov, *Isoelectric point of free and adsorbed cytochrome c determined by various methods*. Colloids and Surfaces B: Biointerfaces, 2019. **174**: p. 87-94.

337. Weichert, W.S., et al., *Assaying for structural variation in the parvovirus capsid and its role in infection*. *Virology*, 1998. **250**(1): p. 106-17.
338. Bioinformatics, S.S.I.o. *ExpASy: ProtParam Tool*. [cited 2021 May 25]; Available from: <https://web.expasy.org/protparam/>.
339. Pandey, L.M., *Surface engineering of personal protective equipments (PPEs) to prevent the contagious infections of SARS-CoV-2*. *Surface Engineering*, 2020. **36**(9): p. 901-907.
340. Gobeil, S.M.C., et al., *Effect of natural mutations of SARS-CoV-2 on spike structure, conformation, and antigenicity*. *Science (New York, N.Y.)*, 2021. **373**(6555): p. eabi6226.
341. Walls, A.C., et al., *Structure, Function, and Antigenicity of the SARS-CoV-2 Spike Glycoprotein*. *Cell*, 2020. **181**(2): p. 281-292.e6.
342. Wrapp, D., et al., *Cryo-EM structure of the 2019-nCoV spike in the prefusion conformation*. *Science*, 2020. **367**(6483): p. 1260-1263.
343. Johansen, T., et al., *Chapter Nine - Methods for Studying Interactions Between Atg8/LC3/GABARAP and LIR-Containing Proteins*, in *Methods in Enzymology*, L. Galluzzi, J.M. Bravo-San Pedro, and G. Kroemer, Editors. 2017, Academic Press. p. 143-169.
344. Anantanawat, K., et al., *High-throughput Quant-iT PicoGreen assay using an automated liquid handling system*. *BioTechniques*, 2019. **66**(6): p. 290-294.

## A Appendix

### A.1 Virus surface hydrophobicity characterization using chemical force microscopy

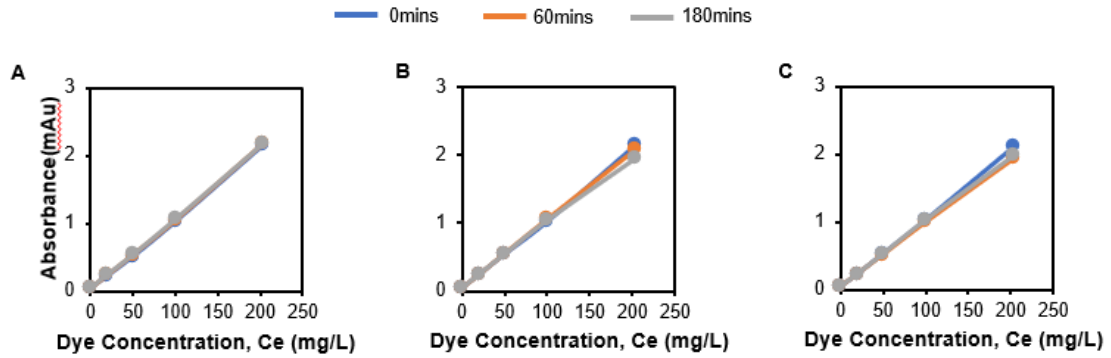


**Figure A.1.1: Time course experiments to determine changes in dye absorbance readings at the different dye concentrations used with PBS. (A) Rose Bengal in PBS (B) Rose Bengal in PBS + 195mM NaCl (C) Rose Bengal in PBS + 845mM NaCl.**

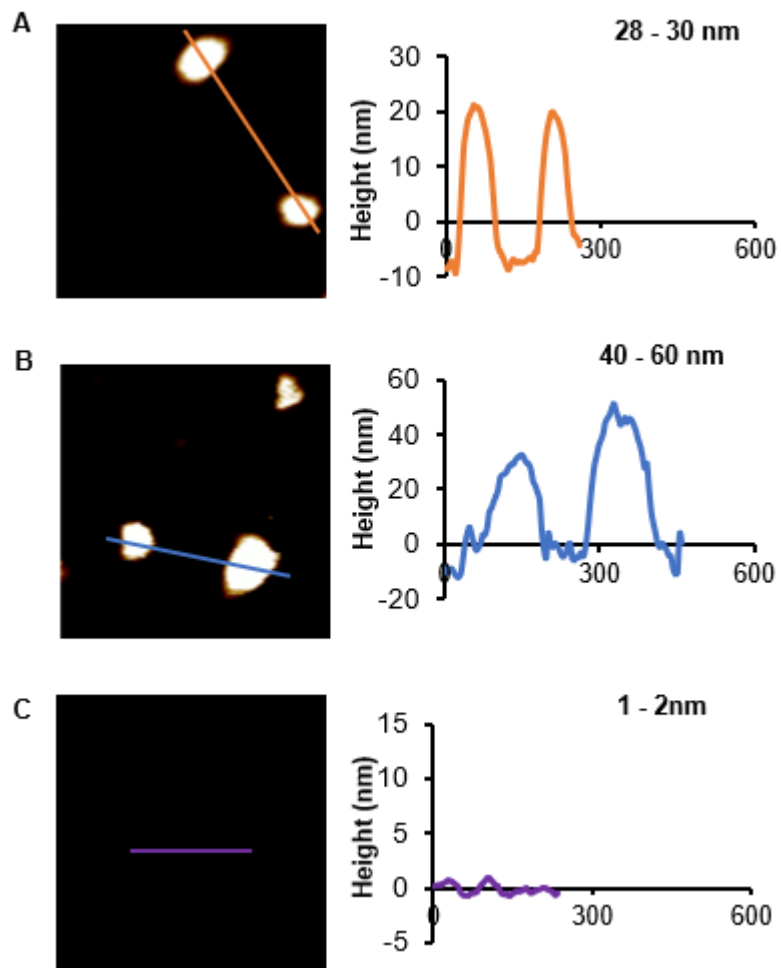


**Figure A.1.2: Topographic image and corresponding height analysis of virus and control surface.** (A) PPV (B) BVDV (C) Control surface. Scan size for viruses and control – 500nm X 500nm. CSG30 probes was used for imaging in PBS.

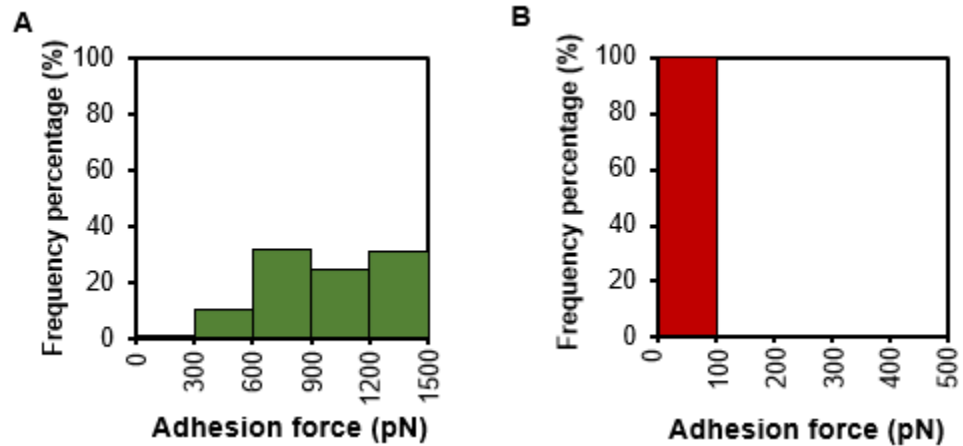


**Figure A.1.3: Confirmation of AFM probe functionalization** (A) Positive control (CH<sub>3</sub> probe/CH<sub>3</sub> gold coated glass slide) (B) Negative control (CH<sub>3</sub> probe/OH gold coated glass slide). Control – 500nm X 500nm. PBS was used as the buffer in this measurement.

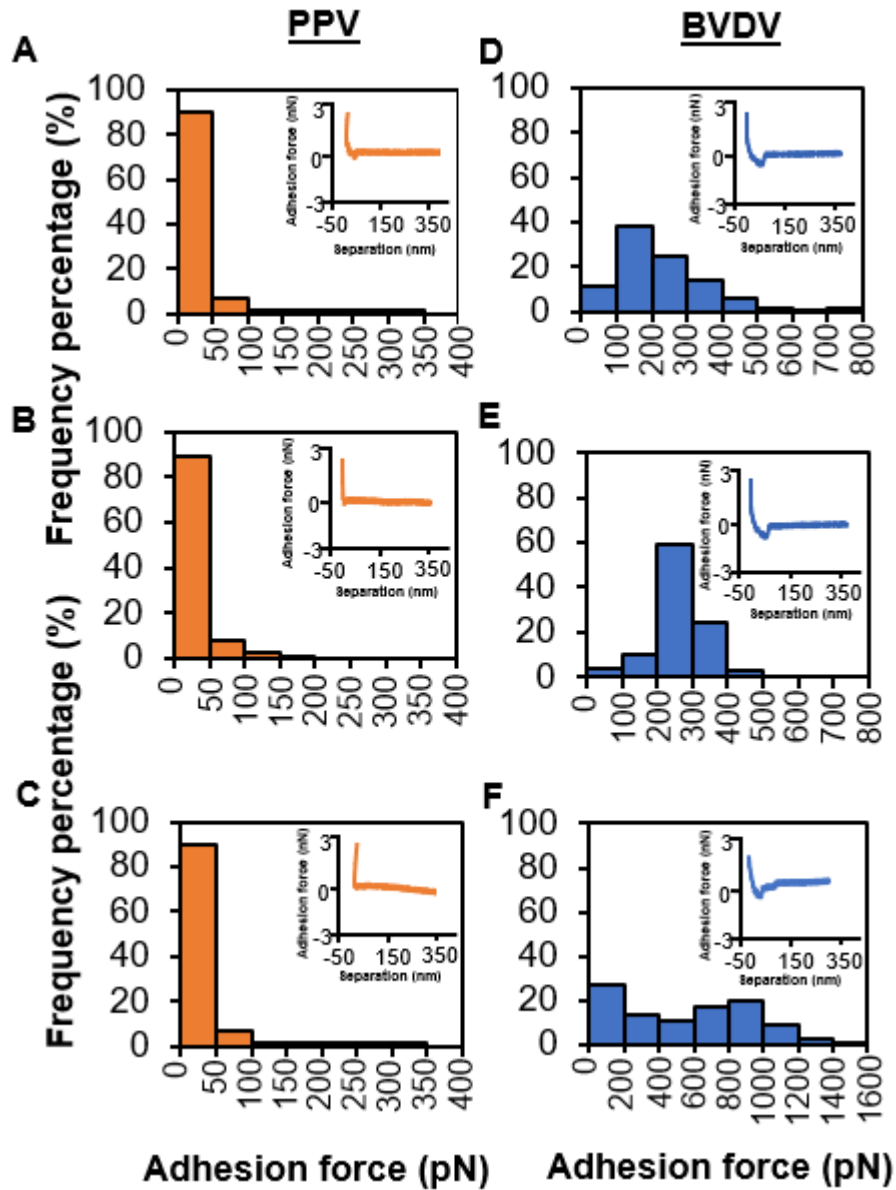


**Figure A.1.4: Adhesion histograms and representative force-distance curves (retracted portion only).** (A) PPV in 1X PBS (B) PPV in 1X PBS + 195mM NaCl (C) PPV in 1X PBS + 845mM NaCl (D) BVDV in 1X PBS (E) BVDV in 1X PBS + 195mM NaCl (F) BVDV in 1X PBS + 845mM NaCl.  $\geq 400$   $F-D$  curves were recorded over 500nm X 500nm areas.

**Table A.1.1.** Summary of mean adhesion force for PPV and BVDV.

<b>BUFFER SOLUTION</b>	<b>PPV MEAN FORCE (pN)</b>	<b>BVDV MEAN FORCE (pN)</b>
1X PBS	16	230
1X PBS + 195mM NaCl	17	262
1X PBS + 845mM NaCl	10	548

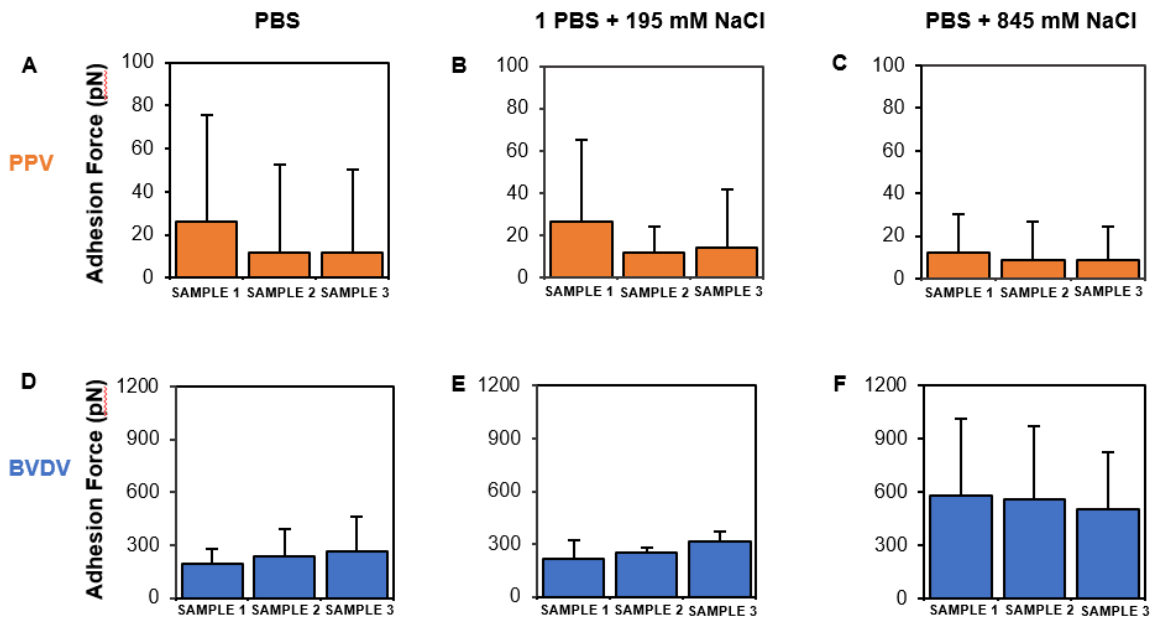


**Figure A.1.5: Adhesion force of each sample for PPV and BVDV in PBS (A) PPV in PBS (B) PPV in PBS + 195 mM NaCl (C) PPV in PBS + 845 mM NaCl (D) BVDV in PBS (E) BVDV in PBS + 195 mM NaCl (F) BVDV in PBS + 845 mM NaCl.  $\geq 400$  *F-D* curves were recorded over 500nm X 500nm areas.**

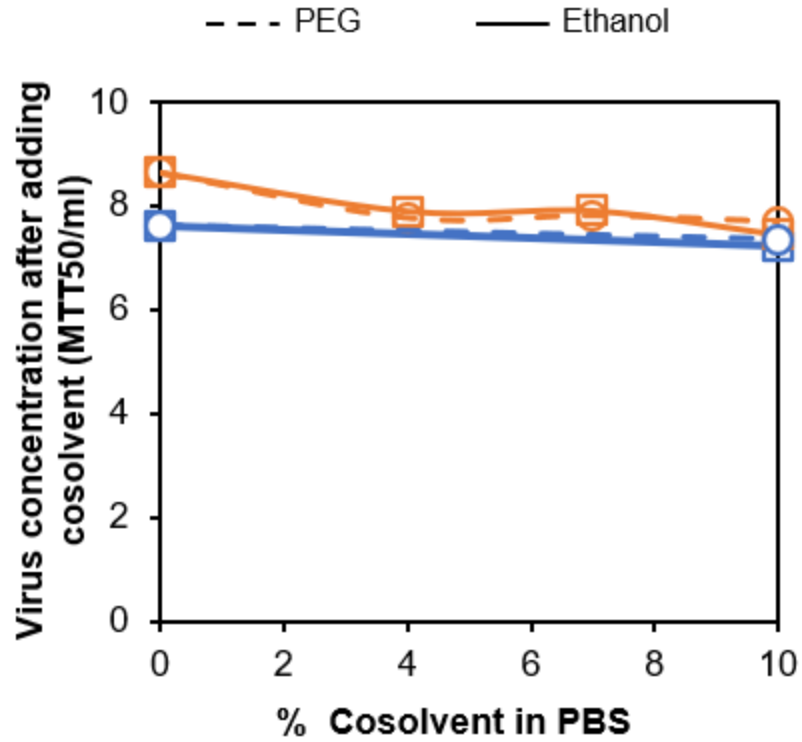
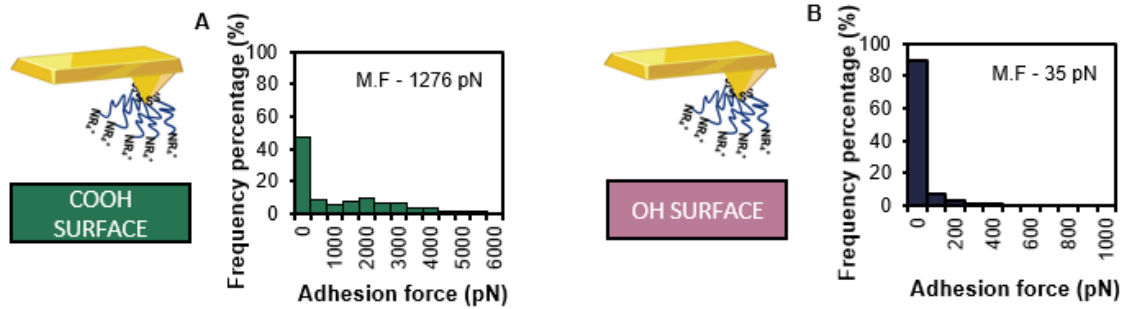


**Figure A.1.6: PPV and BVDV concentration as a function of cosolvent addition.** Using MTT assay the concentration of PPV and BVDV was quantified before and after PEG and ethanol were added.

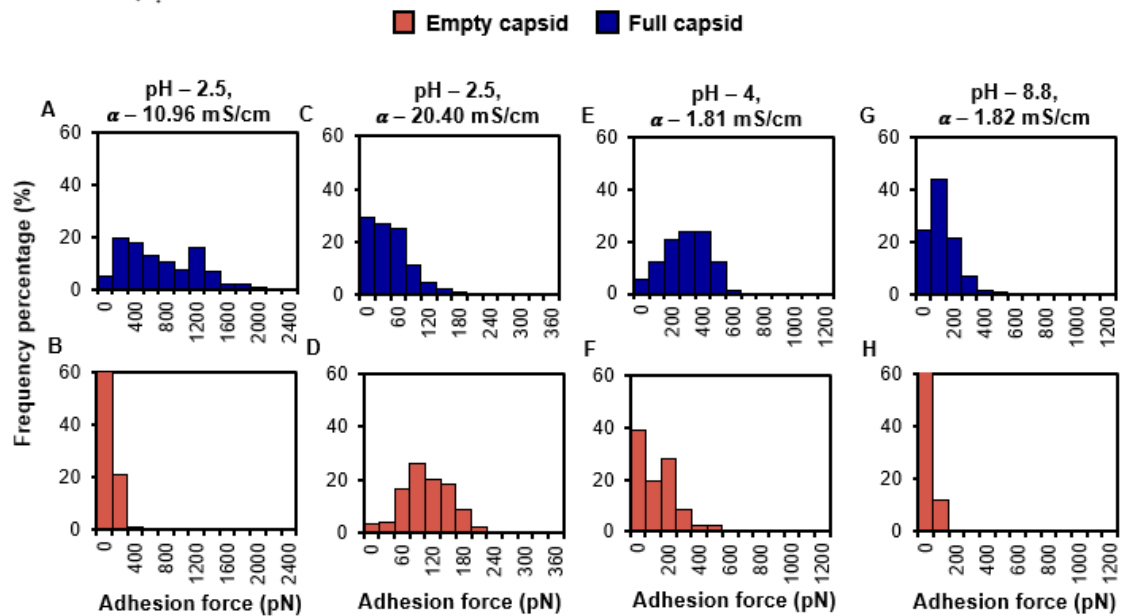
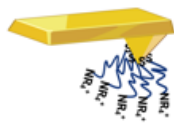
**Table A.1.2.** The maximum wavelength absorbance for Rose Bengal was determined through testing wavelengths ranging from 543 – 600nm. Dye concentrations between 0 mM - 0.4 mM was mixed with either water or PBS, and absorbance was read using a UV-vis spectrophotometer

Dye conc.	Water			1X PBS			PBS + 195mM NaCl			Wavelength
<b>0mM (Water or buffer)</b>	0.038	0.037	0.037	0.036	0.036	0.036	0.037	0.037	0.037	<b>543</b>
<b>0.01mM DYE</b>	0.46	0.429	0.468	0.428	0.445	0.449	0.399	0.454	0.453	<b>543</b>
<b>0.027mM</b>	1.074	1.051	1.059	0.985	1.011	1.053	1.036	1.065	1.01	<b>543</b>
<b>0.1mM</b>	1.994	1.964	1.932	1.958	2.099	2.208	1.936	2.019	2.114	<b>543</b>
<b>0.2mM</b>	4.013	3.958	4.048	3.759	3.859	3.801	3.678	3.71	3.757	<b>543</b>
<b>0.4mM</b>	OVRFLW	OVRFLW	OVRFLW	<b>543</b>						
<b>0mM (Water or buffer)</b>	0.038	0.037	0.037	0.036	0.036	0.036	0.037	0.037	0.037	<b>560</b>
<b>0.01mM</b>	0.306	0.288	0.313	0.289	0.3	0.304	0.276	0.31	0.311	<b>560</b>
<b>0.027mM</b>	0.686	0.685	0.688	0.648	0.663	0.687	0.688	0.713	0.674	<b>560</b>
<b>0.1mM</b>	1.249	1.223	1.234	1.272	1.353	1.424	1.279	1.34	1.397	<b>560</b>
<b>0.2mM</b>	2.684	2.622	2.664	2.526	2.579	2.559	2.508	2.521	2.525	<b>560</b>
<b>0.4mM</b>	OVRFLW	OVRFLW	OVRFLW	<b>560</b>						
<b>0mM (Water or buffer)</b>	0.037	0.037	0.037	0.036	0.036	0.036	0.037	0.037	0.037	<b>570</b>
<b>0.01mM</b>	0.112	0.105	0.115	0.107	0.109	0.112	0.105	0.114	0.116	<b>570</b>
<b>0.027mM</b>	0.211	0.209	0.211	0.21	0.211	0.217	0.223	0.228	0.22	<b>570</b>
<b>0.1mM</b>	0.365	0.358	0.363	0.39	0.415	0.433	0.411	0.429	0.449	<b>570</b>
<b>0.2mM</b>	0.771	0.755	0.763	0.815	0.828	0.821	0.896	0.896	0.898	<b>570</b>
<b>0.4mM</b>	1.469	1.447	1.51	1.73	1.805	1.764	2.049	2.088	2.027	<b>570</b>
<b>0mM (Water or buffer)</b>	0.037	0.037	0.037	0.036	0.036	0.036	0.037	0.037	0.037	<b>580</b>
<b>0.01mM</b>	0.054	0.051	0.056	0.051	0.05	0.052	0.05	0.052	0.054	<b>580</b>
<b>0.027mM</b>	0.068	0.068	0.068	0.074	0.07	0.071	0.074	0.075	0.076	<b>580</b>
<b>0.1mM</b>	0.097	0.097	0.098	0.11	0.117	0.117	0.118	0.123	0.127	<b>580</b>
<b>0.2mM</b>	0.178	0.174	0.176	0.215	0.216	0.216	0.262	0.261	0.261	<b>580</b>
<b>0.4mM</b>	0.329	0.323	0.336	0.495	0.52	0.505	0.654	0.671	0.652	<b>580</b>
<b>0mM (Water or buffer)</b>	0.037	0.037	0.037	0.036	0.036	0.036	0.037	0.037	0.036	<b>590</b>
<b>0.01mM</b>	0.043	0.042	0.045	0.04	0.039	0.039	0.039	0.039	0.041	<b>590</b>
<b>0.027mM</b>	0.042	0.042	0.042	0.047	0.043	0.042	0.043	0.043	0.046	<b>590</b>
<b>0.1mM</b>	0.047	0.047	0.049	0.053	0.055	0.052	0.052	0.053	0.055	<b>590</b>
<b>0.2mM</b>	0.062	0.061	0.061	0.073	0.072	0.073	0.083	0.085	0.084	<b>590</b>
<b>0.4mM</b>	0.092	0.09	0.092	0.131	0.137	0.132	0.167	0.171	0.168	<b>590</b>
<b>0mM (Water or buffer)</b>	0.037	0.037	0.037	0.036	0.036	0.036	0.037	0.037	0.037	<b>600</b>
<b>0.01mM</b>	0.042	0.04	0.043	0.038	0.037	0.037	0.037	0.037	0.039	<b>600</b>
<b>0.027mM</b>	0.037	0.037	0.037	0.042	0.038	0.037	0.038	0.038	0.04	<b>600</b>
<b>0.1mM</b>	0.038	0.039	0.04	0.042	0.045	0.04	0.039	0.04	0.041	<b>600</b>
<b>0.2mM</b>	0.042	0.042	0.041	0.045	0.044	0.045	0.046	0.049	0.047	<b>600</b>
<b>0.4mM</b>	0.048	0.047	0.047	0.055	0.058	0.055	0.062	0.062	0.062	<b>600</b>

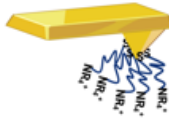
## A.2 Effect of Charge and Hydrophobicity on the Separation of Empty and Full AAV Capsids on Ion Exchange Chromatography



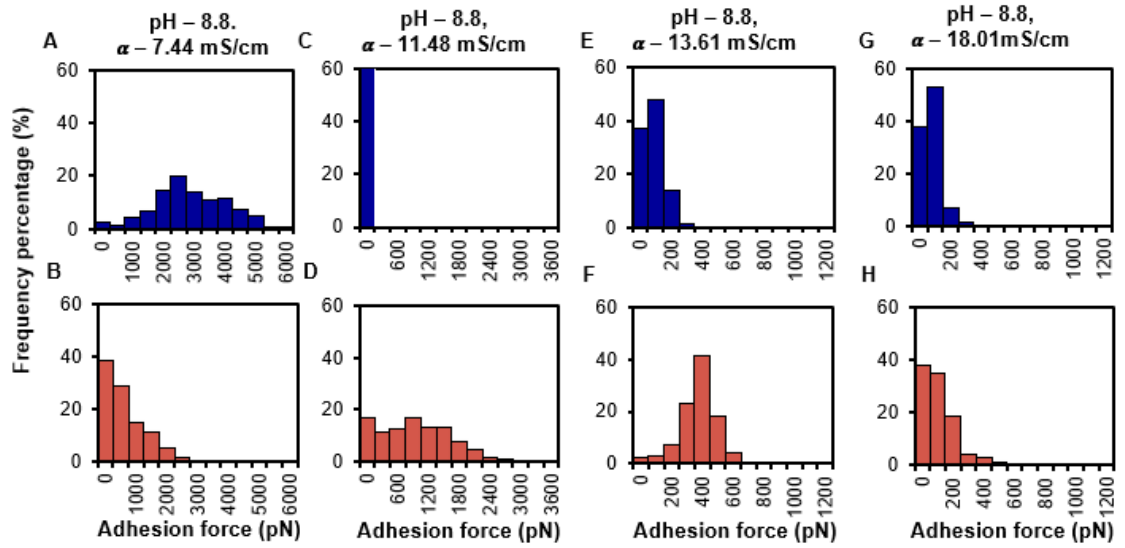
**Figure A.2.1: Control Data for  $\text{NR}_4^+$  Probe in PB, pH 7.** (A) Positive control (B) Negative control.  $F - D$  curves  $\geq 450$  were recorded over  $500\text{nm} \times 500\text{nm}$  areas. M.F is the average mean force measured from the triplicate run.



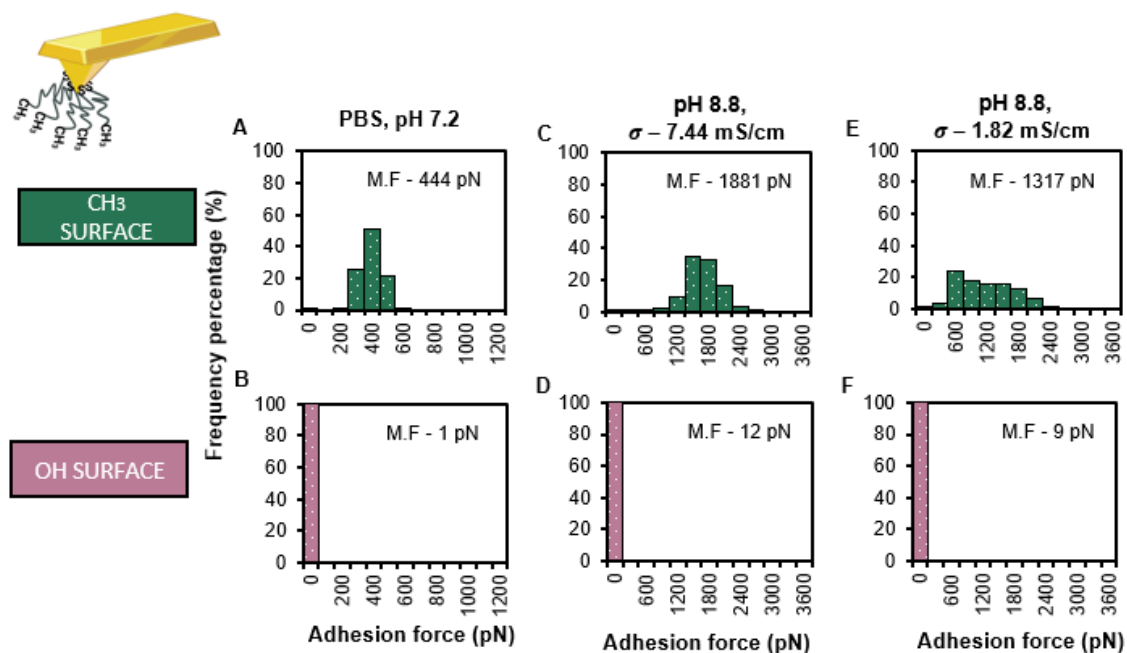
**Figure A.2.2: Adhesion histograms in different buffer conditions for AAV full and empty capsids using  $\text{NR}_3^+$  probe.  $F-D$  curves  $\geq 450$  were recorded over  $500\text{nm} \times 500\text{nm}$  areas.**



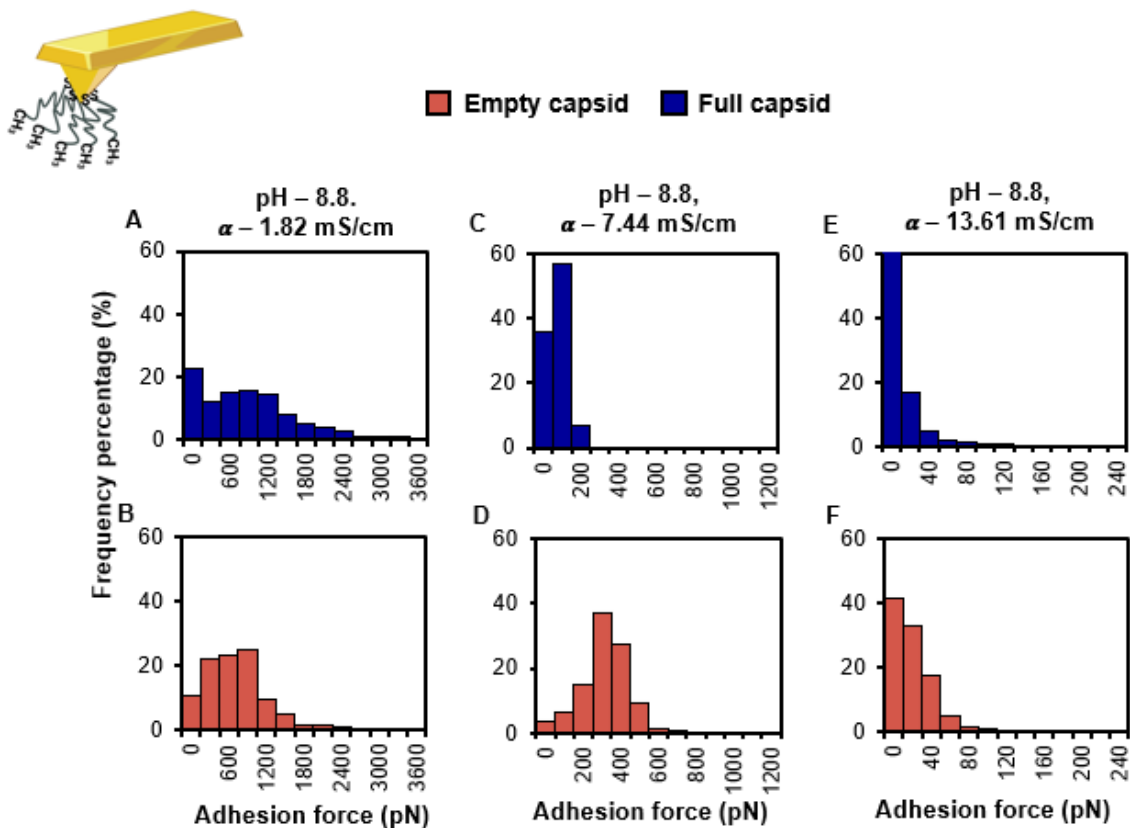
Empty capsid Full capsid



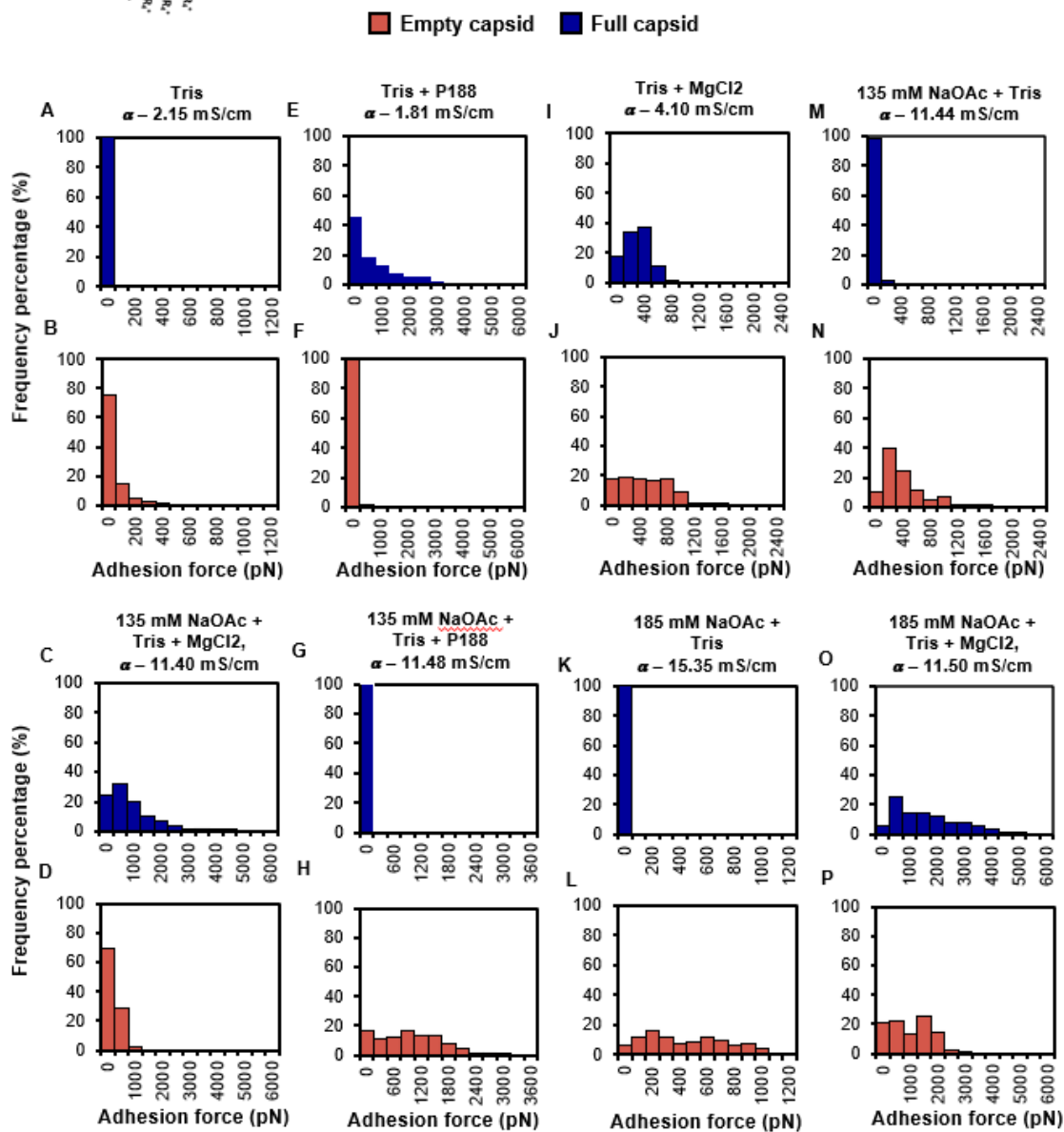
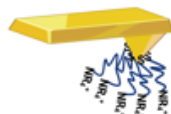
**Figure A.2.3: Adhesion histograms in different buffer conditions for AAV full and empty capsids with NR<sub>3</sub><sup>+</sup> probe. *F*–*D* curves  $\geq 450$  were recorded over 500nm X 500nm areas.**



**Figure A.2.4: Control data using CH<sub>3</sub> probe.** (A -B) Positive and negative control in PBS, pH 7.2. (C - D) Positive and negative control in high conductivity buffer, 7.44 mS/cm, pH 8.8. (E - F) Positive and negative control in low conductivity buffer, 1.82 mS/cm, pH 8.8. *F-D* curves  $\geq 450$  were recorded over 500nm X 500nm areas. M.F is the average mean force measured from the triplicate run.



**Figure A.2.5:** Adhesion histograms in different buffer conditions for AAV full and empty capsids using CH<sub>3</sub> probe. *F-D* curves  $\geq 450$  were recorded over 500nm X 500nm areas.



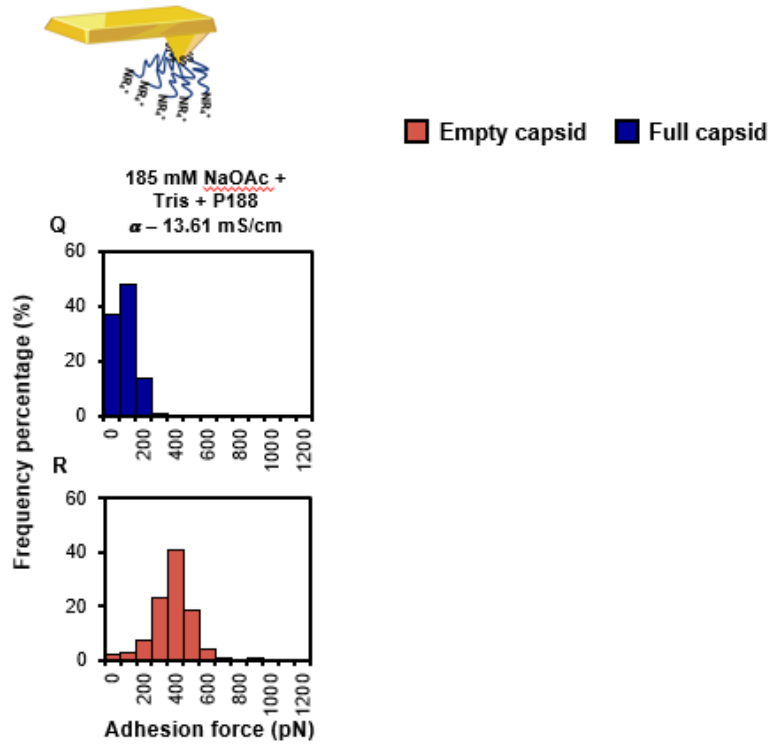


**Figure A.2.7: Adhesion histograms for AAV full and empty capsids in buffers at pH 8.8 with NR<sub>3</sub><sup>+</sup> probe.** *F-D* curves  $\geq 450$  were recorded over 500nm X 500nm area. Concentrations of the buffer components: 100 mM Tris, 5 mM MgCl<sub>2</sub>, 0.01% P188.

### A.3 Single-Particle Characterization of SARS-CoV-2 Isoelectric Point and Comparison to Variants of Interest

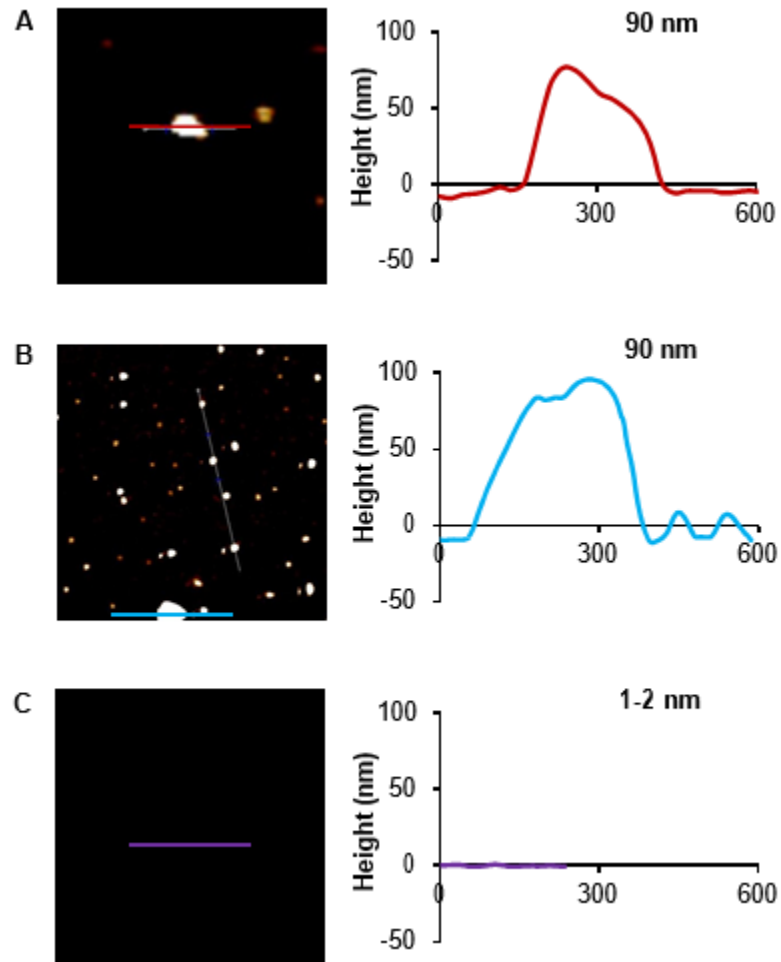


**Figure A.3.1: Topographic image and corresponding height analysis of virus and control surface.** (a) SARS-CoV-2 gamma irradiated. (b) SARS-CoV-2 heat inactivated and (c) Control surface. Scan size for viruses -  $3\mu\text{m} \times 3\mu\text{m}$ , control -  $500\text{nm} \times 500\text{nm}$ .

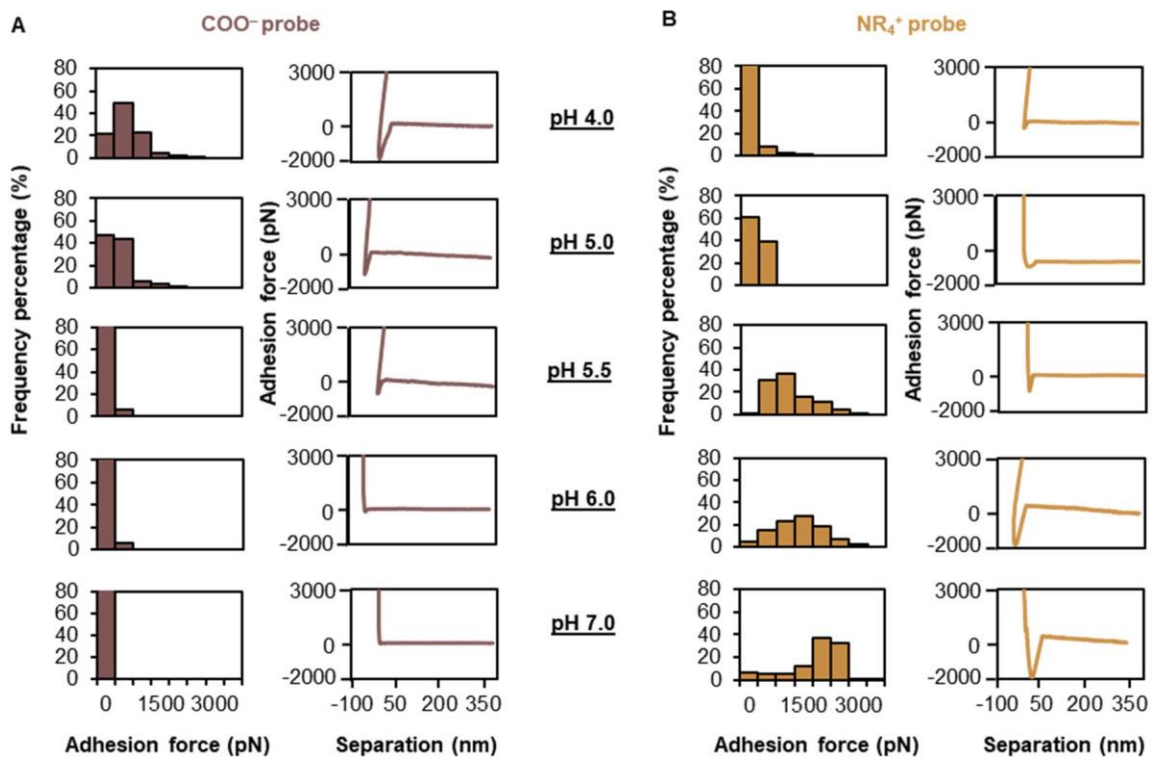


**Figure A.3.2: Adhesion and representative force–distance curves (retracted portion only) of irradiated SARS-CoV-2.** (a) COO<sup>-</sup>-terminated probe and (b) NR<sub>4</sub><sup>+</sup>-terminated probe, recorded in 20 mM citrate (pH 4-6) or phosphate buffers (pH 7). Each figure represents 450 *F–D* curves.

**Table A.3.1.** Surface hydrophobicity comparison among WT and VOI.

<b>Pango Lineage</b>	<b>PDB</b>	<b>Total Surface Residues</b>	<b>Hydrophobicity</b>
WT	6VSB	2454	29
B.1.1.7	7LWV	2089	-146
B.1.351	7LYQ	1992	-191

The surface residues of the WT and VOI were found by in PyMol using 'findSurfaceResidue' script. Surface hydrophobicity was calculated by summing the individual hydrophobicity values of residues assigned as per the Eisenberg hydrophobicity scale.

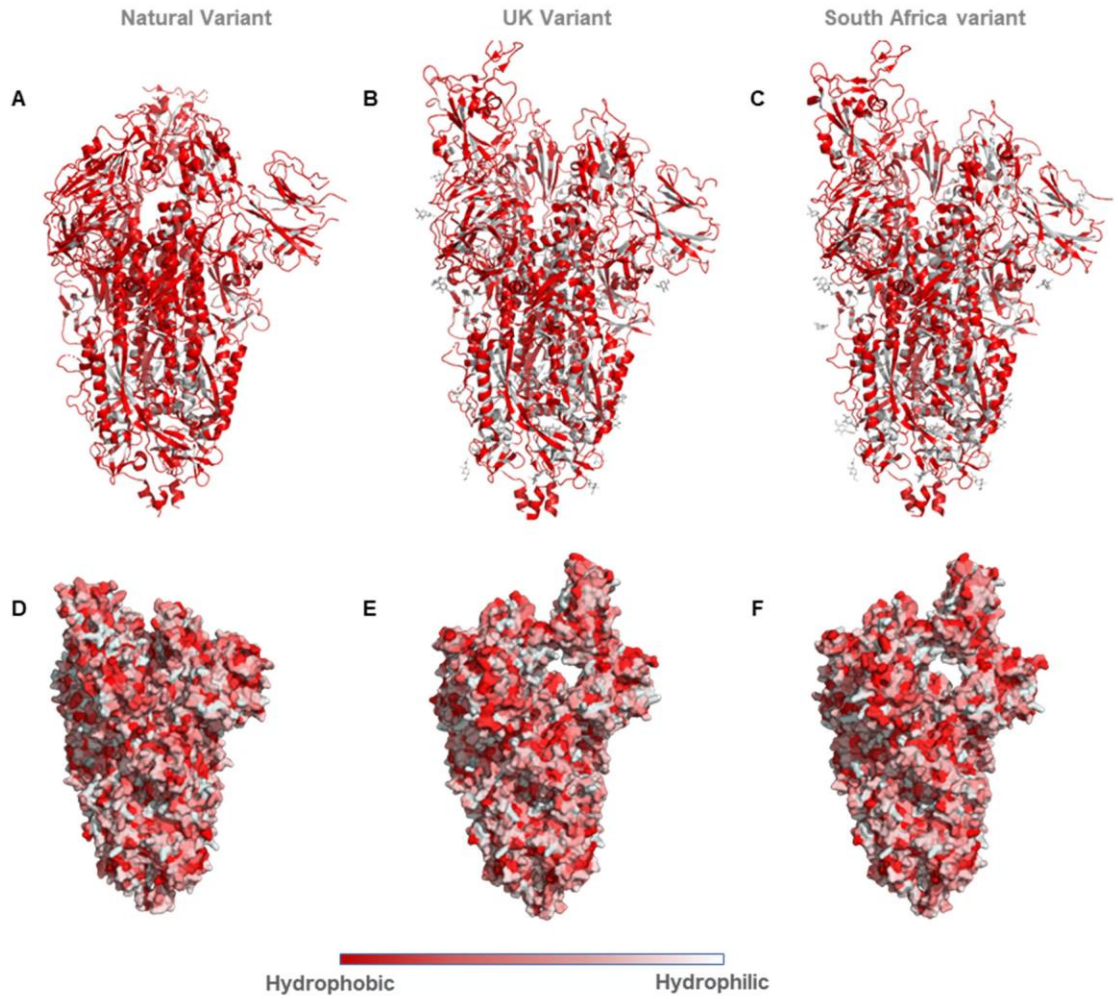


**Figure A.3.3: Surface characteristics of S-proteins of WT and VOI.** (A) Surface residues (marked in red) (B) Surface hydrophobicity map of S-proteins.

## **B Copyright documentation**

### **B.1 Reuse license for Figure 2.2**

JOHN WILEY AND SONS LICENSE  
TERMS AND CONDITIONS

Nov 29, 2022

---

This Agreement between Michigan Technological University -- Oluwatoyin Areo ("You") and John Wiley and Sons ("John Wiley and Sons") consists of your license details and the terms and conditions provided by John Wiley and Sons and Copyright Clearance Center.

License Number 5414410499152

License date Oct 22, 2022

Licensed Content  
Publisher John Wiley and Sons

Licensed Content  
Publication Biotechnology Journal

Licensed Content Title Manufacturing of recombinant adeno-associated viruses  
using mammalian expression platforms

Licensed Content Author Bruno Gaillet, Rénaud Gilbert, Amine Kamen, et al

Licensed Content Date Feb 8, 2017

Licensed Content Volume 12

Licensed Content Issue 3

Licensed Content Pages 16

Type of Use Dissertation/Thesis

Requestor type University/Academic

Format electronic

Portion Figures/table

Number of figures/tables 1

Will you be translating? No

Title MEASURING THE PHYSICOCHEMICAL PROPERTIES OF  
VIRAL VECTORS TO ENHANCE GENE THERAPY  
PRODUCTION

Institution name Michigan Technological University

Expected presentation  
date Nov 2022

Order reference number 2

Portions Figure 1

Michigan Technological University  
107 Quincy st, Apt B

Requestor Location

HANCOCK, MI 49930  
United States  
Attn: Michigan Technological University

Publisher Tax ID

EU826007151

Total

0.00 USD

## **B.2 Reuse license for Figure 2.4 and Figure 2.5**

This is a License Agreement between OLUWATOYIN AREO ("User") and Copyright Clearance Center, Inc. ("CCC") on behalf of the Rightsholder identified in the order details below. The license consists of the order details, the Marketplace Order General Terms and Conditions below, and any Rightsholder Terms and Conditions which are included below.

All payments must be made in full to CCC in accordance with the Marketplace Order General Terms and Conditions below.

Order Date

08-Nov-2022

Order License ID

1287952-1

ISSN

1566-5232

Type of Use

Republish in a thesis/dissertation

Publisher

BENTHAM SCIENCE PUBLISHERS LTD.

Portion

Chart/graph/table/figure

LICENSED CONTENT

Publication Title

CURRENT GENE THERAPY

Date

01/01/2001

Language

English

Country

Netherlands

Rightsholder

EUREKA SCIENCE (FZC)

Publication Type

Journal

## REQUEST DETAILS

Portion Type

Chart/graph/table/figure

Number of Charts / Graphs / Tables / Figures Requested

2

Format (select all that apply)

Electronic

Who Will Republish the Content?

Academic institution

Duration of Use

Life of current and all future editions

Lifetime Unit Quantity

Up to 1,500,000

Rights Requested

Main product

Distribution

Worldwide

Translation

Original language of publication

Copies for the Disabled?

No

Minor Editing Privileges?

Yes

Incidental Promotional Use?

No

Currency

USD

#### NEW WORK DETAILS

Title

MEASURING THE PHYSICOCHEMICAL PROPERTIES OF VIRAL VECTORS TO  
ENHANCE GENE THERAPY PRODUCTION

Instructor Name

Dr. Caryn Heldt

Institution Name

Michigan Technological University

Expected Presentation Date

2022-11-21

#### ADDITIONAL DETAILS

Order Reference Number

N/A

The Requesting Person/Organization to Appear on the License

OLUWATOYIN AREO

#### REUSE CONTENT DETAILS

Title, Description or Numeric Reference of the Portion(s)

Fig.2 and Fig. 3

Editor of Portion(s)

Liang Cheng

Volume of Serial or Monograph

10

Page or Page Range of Portion

423-436

Title of the Article/Chapter the Portion Is From

Production, Purification and Characterization of Adeno-Associated Vectors

Author of Portion(s)

Eduard Ayuso, Federico Mingozzi and Fatima Bosch

Issue, if Republishing an Article From a Serial

6

Publication Date of Portion

2000-12-31

### B.3 Reuse license for Figure 2.6

ELSEVIER LICENSE

TERMS AND CONDITIONS

Oct 21, 2022

---

This Agreement between Michigan Technological University -- Oluwatoyin Areo ("You") and Elsevier ("Elsevier") consists of your license details and the terms and conditions provided by Elsevier and Copyright Clearance Center.

License Number 5413800039842

License date Oct 21, 2022

Licensed Content  
Publisher Elsevier

Licensed Content  
Publication Journal of Chromatography A

Licensed Content Title Thermodynamic modelling of hydrophobic interaction  
chromatography of biomolecules in the presence of salt

Licensed Content Author Mohammad Reza Mirani, Farshad Rahimpour

Licensed Content Date Nov 27, 2015  
Licensed Content Volume 1422

Licensed Content Issue n/a

Licensed Content Pages 8

Start Page 170

End Page 177

Type of Use reuse in a thesis/dissertation

Portion figures/tables/illustrations

Number of  
1  
figures/tables/illustrations

Format electronic

Are you the author of this  
No

Elsevier article?

Will you be translating? No

Title MEASURING THE PHYSICOCHEMICAL PROPERTIES OF  
VIRAL VECTORS TO ENHANCE GENE THERAPY  
PRODUCTION

Institution name Michigan Technological University

Expected presentation  
date Nov 2022

Order reference number 1

Portions Fig. 1.

Michigan Technological University  
107 Quincy st, Apt B

Requestor Location

HANCOCK, MI 49930  
United States  
Attn: Michigan Technological University

Publisher Tax ID 98-0397604

Total 0.00 USD

## B.4 Reuse license for Figure 2.10

SPRINGER NATURE LICENSE

TERMS AND CONDITIONS

Nov 29, 2022

---

This Agreement between Michigan Technological University -- Oluwatoyin Areo ("You") and Springer Nature ("Springer Nature") consists of your license details and the terms and conditions provided by Springer Nature and Copyright Clearance Center.

License Number	5422110980043
License date	Nov 04, 2022
Licensed Content Publisher	Springer Nature
Licensed Content Publication	Springer eBook
Licensed Content Title	Atomic Force Microscopy for Structural and Biophysical Investigations on Nuclear Pore Complexes
Licensed Content Author	Ivan Liashkovich, Gonzalo Rosso, Victor Shahin
Licensed Content Date	Jan 1, 2022
Type of Use	Thesis/Dissertation

Requestor type            academic/university or research institute

Format                    electronic

Portion                    figures/tables/illustrations

Number of  
figures/tables/illustrations 1

Will you be translating? No

Circulation/distribution 200 - 499

Author of this Springer  
Nature content            no

Will you be translating? No

Title                        MEASURING THE PHYSICOCHEMICAL PROPERTIES OF  
VIRAL VECTORS TO ENHANCE GENE THERAPY  
PRODUCTION

Institution name           Michigan Technological University

Expected presentation  
date                        Nov 2022

Order reference number 5

Portions                    Figure 1

Michigan Technological University  
107 Quincy st, Apt B

Requestor Location

HANCOCK, MI 49930  
United States  
Attn: Michigan Technological University

Total

0.00 USD